



## "Detecting crop damage using Sentinel-2 imagery in a smallholder agriculture landscape"

Champagne, Céline

### ABSTRACT

Smallholder farmers in Sub-Saharan African countries are facing more and more challenges in terms of agriculture. Not only the lack of mechanization remains a problem to feed the population that continues to grow but in addition, external threats such as the invasive pest Fall armyworm and climate hazards increase the risk of food insecurity and famine in some countries. Determining the extent of such damage requires extensive field work and a lot of time when it is necessary to act quickly to deliver food aid. Remote sensing can represent a real solution to this problem. Indeed, monitoring crops remotely is a technique that has been used successfully for several years now. The recent availability of free of access Sentinel-2 imagery opens the door to these kind of technologies for any developing countries. Therefore, this master thesis aims, in collaboration with CIMMYT who is actively working on these matters in Zimbabwe, to assess the feasibility of detecting damage on maize in two districts of the country using satellite imagery. An intermediate objective is to produce a crop types map over the area of study. Firstly, we looked at defoliation damage due Fall Armyworm. It turns out that those damage are rather patchy within a field. This in combination with a complex landscape, one must conclude that Sentinel-2 does not have the spatial characteristic to overcome the configuration of these smallholder fields that, on top of the already existing confounding factors, suffered from intense drought. Secondly, this work took a turn after Cyclone Idai hit our study area. Chip...

### CITE THIS VERSION

Champagne, Céline. *Detecting crop damage using Sentinel-2 imagery in a smallholder agriculture landscape*. Faculté des bioingénieurs, Université catholique de Louvain, 2019. Prom. : Defourny, Pierre. <http://hdl.handle.net/2078.1/thesis:22451>

Le répertoire DIAL.mem est destiné à l'archivage et à la diffusion des mémoires rédigés par les étudiants de l'UCLouvain. Toute utilisation de ce document à des fins lucratives ou commerciales est strictement interdite. L'utilisateur s'engage à respecter les droits d'auteur liés à ce document, notamment le droit à l'intégrité de l'oeuvre et le droit à la paternité. La politique complète de droit d'auteur est disponible sur la page [Copyright policy](#)

DIAL.mem is the institutional repository for the Master theses of the UCLouvain. Usage of this document for profit or commercial purposes is strictly prohibited. User agrees to respect copyright, in particular text integrity and credit to the author. Full content of copyright policy is available at [Copyright policy](#)

## Faculté des bioingénieurs

# Detecting crop damage using Sentinel-2 imagery in a smallholder agriculture landscape

Chipinge and Makoni Districts, Zimbabwe

Auteur : Céline Champagne

Promoteur(s) : Prof. Pierre Defourny (UCL/ELI/ELIE)

Dr. Frédéric Baudron (CIMMYT)

Lecteur(s) : Prof. Anne Legrève (UCL/ELI/ELIM)

Dr. Martin Claverie (UCL/ELI/ELIE)

Année académique 2018-2019

Bioingénieur : sciences et technologies de l'environnement



## Acknowledgements

I would like to start by expressing my special thanks to my supervisors, Pr. Pierre Defourny and Dr. Frédéric Baudron for giving me the opportunity to work on this really interesting and challenging subject and develop my knowledge in remote sensing.

I thank Professor Defourny for introducing me to the world of remote sensing and his advice and guidance throughout this work.

I thank Dr. Frédéric Baudron for welcoming me in Zimbabwe and sharing his knowledge and experience on the field. I also thank Isaac Chaipa and his team from GOAL for organizing the field data collection and accompanying me in Makoni District. I would also like to thank Rose, from CIMMYT who welcomed me into her community and gave me the opportunity to discover a bit of the Zimbabwean culture.

I am also grateful for the assistance and support given throughout the year by the researchers from the Geomatics Laboratory.

I thank Dr. Nicolas Velings for reading the thesis through and making recommendations.

This year would not have been the same without my fellow mates from the thesis room. First, I would like to thank Caroline for our conversations, her precious help and advice during this year and her motivation which helped me a lot. Also, thanks to Dorian my “aménagiste” friend for these two years of master spent together. Julien, thank you for your everyday joyful “Good Mornings” and being always in a good mood. Thanks to Alexis for his help and support when I could not make a program work. Also, thanks to Baptiste for his constant stress-free mood.

More personally, I would like to thank my best friends, Margot, Louise, Clémence, Pauline and Odile for their constant support during the past five years but also all the moments and experiences I got to share with them during my time in Louvain-La-Neuve.

A huge thank you to Maxime for helping me during this work and always reassuring me and believing in me.

Last but not least, I would like to express my profound gratitude to my family for always believing in me and doing everything in their power to help me throughout my years of study and this work. It would never have been possible without you.



# Table of contents

I.	<b>Introduction .....</b>	<b>1</b>
II.	<b>Literature review.....</b>	<b>3</b>
A.	The Fall Armyworm ( <i>Spodoptera frugiperda</i> ).....	3
1.	History and migration behaviour .....	3
2.	Description of Spodoptera frugiperda .....	3
3.	Life Cycle and Damage on Maize.....	4
4.	Climate conditions and effect of temperature .....	7
5.	Invasion and Impacts in Africa .....	7
B.	Current method of monitoring FAW .....	9
C.	Remote Sensing Monitoring: Crop Disease and Pests Detection .....	10
1.	Resolution of remotely sensed data .....	10
2.	The potential of Sentinel-2 satellites .....	12
3.	Spectral Features: Wavebands and Indices .....	13
4.	Classification methods and related features .....	16
D.	Conclusion .....	18
III.	<b>Objectives .....</b>	<b>20</b>
IV.	<b>Material .....</b>	<b>21</b>
A.	Area of Study .....	21
1.	Geographic Location .....	21
2.	Soil types .....	22
3.	Climate and topography.....	22
4.	Characteristics of agriculture and maize harvesting calendar .....	25
B.	Data sources .....	25
1.	Ground dataset .....	26
2.	Sentinel-2 images.....	27
3.	Pléiades Images.....	29
4.	Software .....	30
V.	<b>Methods for Damage Detection and Crop Mapping .....</b>	<b>31</b>
A.	Overall Approach .....	31
B.	<i>In Situ</i> Data Preparation .....	32
1.	FAW 2018 Field Campaign .....	32

2. FAW 2019 Field Campaign .....	32
3. Idai Field Campaign .....	32
C. Image Pre-processing .....	32
D. Fall Armyworm Damage Detection .....	33
1. Photointerpretation .....	33
2. Sensitivity Analysis .....	33
3. Confounding Factors Analysis .....	34
E. Cyclone Idai Damage Detection.....	36
1. Sensitivity Analysis .....	36
2. Photointerpretation .....	37
F. Crop Mapping.....	37
1. Binary Cropland Classification.....	37
2. Crop Type Classification .....	38
3. Validation method .....	38
<b>VI. Results and Discussion .....</b>	<b>40</b>
A. Fall Armyworm Damage Detection .....	40
1. Photointerpretation .....	40
2. Sensitivity Analysis .....	45
3. Confounding factors analysis .....	48
B. Cyclone Idai Damage Detection.....	50
1. Sensitivity Analysis .....	50
2. Photointerpretation .....	55
C. Crop Mapping.....	60
1. Binary cropland mask.....	60
2. Crop-type mapping .....	61
<b>VII. General discussion.....</b>	<b>69</b>
<b>VIII. Conclusion and prospects.....</b>	<b>72</b>
<b>IX. Bibliography .....</b>	<b>I</b>
<b>X. Appendixes.....</b>	<b>VII</b>

# Table of Figures

Figure 1: Egg mass of the Fall Armyworm, <i>Spodoptera frugiperda</i> (J.E. Smith) (John L. Capinera, 2000).....	4
Figure 2: Newly hatched larva of the fall armyworm, <i>Spodoptera frugiperda</i> (J.E. Smith) (John L. Capinera, 2000). .....	4
Figure 3: Mature larva of the fall armyworm, <i>Spodoptera frugiperda</i> (J.E. Smith) showing light-coloured inverted "Y" on the front head (John L. Capinera, 2000). .....	4
Figure 4: Maize growth stages, modified from Clarrie Beckingham, 2007, (Prasanna et al., 2018). ....	5
Figure 5: Early-instar FAW damage on maize leaves in the form of small window panes (Prasanna et al., 2018)	6
Figure 6: Emerging tassel that will push FAW larvae out of the whorl (Prasanna et al., 2018).....	6
Figure 7: Ear/cob damage caused by FAW larva (Prasanna et al., 2018) .....	6
Figure 8: Geographic location of the two study districts, namely Makoni (main town Rusape) and Chipinge....	21
Figure 9: Elevation model of the study area of Chipinge with a Sentinel-2 images of the 28 <sup>th</sup> of February 2019 on top. The three Wards of study are Ward 16 and 20 that are at an average elevation of 430 m and Ward 18 that is at an average elevation of 925 m. DEM source: Aster, Nasa. <a href="https://doi.org/10.5067/ASTER/ASTGTM.002">https://doi.org/10.5067/ASTER/ASTGTM.002</a> ..	23
Figure 10: Mean average monthly temperature in Chipinge from 1985 to 2015, 2016, 2017, 2018 and 2019... 24	24
Figure 11: Cyclone Idai impacts in Zimbabwe, picture posted by Goba C. on the chronicle 'My Zimbabwe News" on the 16 <sup>th</sup> of March 2019. ....	24
Figure 12: Maize cultivation cycle in agro-ecological regions (natural farming regions) II and III (FAO).....	25
Figure 13: Sentinel-2 true-colour image of the 28th of February 2019 over the three study Wards of Chipinge (from left to right, Ward 20, 16 and 18). ....	28
Figure 14: Pléiades true-colours images acquired on the 25th of March 2019 over Ward 18 of Chipinge (left) and on the 29th of March 2019 over Ward 16 of Chipinge (right). ....	29
Figure 15: Workflow of the overall approach used to assess the possibility of detecting crop damage in a smallholder agriculture landscape and map the crops.....	31
Figure 16: Illustration of a dried maize field in Ward 16 (Chipinge) (32.6575°; -20.4312°) on Pléiades (2 m) and Sentinel 2 (10 m) in true and false colours. ....	40
Figure 17: Picture taken on the 22nd of February 2019 of the field illustrated in Figure 16. ....	41
Figure 18: Illustration of a dried maize field in Ward 16 (Chipinge) (32.3658°; -20.4396°) on Pléiades (2 m) and Sentinel 2 (10 m) in true and false colours and a picture of that same field taken on the 22 <sup>nd</sup> of February 2019. ....	41
Figure 19: Illustration of a sparse and heterogenous maize field in Ward 18 (Chipinge) (32.6079°; -20.3973°) on Pléiades (2 m) and Sentinel 2 (10 m) in true and false colours and a picture of that same field taken on the 19 <sup>th</sup> of February 2019. ....	42
Figure 20: Illustration of a weedy maize field already in the tasselling stage, in Ward 18 (Chipinge) (32.6479°; -20.4341°) on Pléiades (2 m) and Sentinel 2 (10 m) in true and false colours and a picture of that same field taken on the 21 <sup>st</sup> of February 2019. ....	43
Figure 21: Illustration of a maize field that is not dense, with patchy FAW damage in Ward 18 (Chipinge) (32.6026°; -20.3946°) on Pléiades (2 m) and Sentinel 2 (10 m) in true and false colours and pictures of that same field taken on the 19 <sup>th</sup> of February 2019. The top picture is an undamaged part of the field and the bottom picture is t of a damaged part. ....	44
Figure 22: VIs response (left) and surface reflectance of the ten original Sentinel-2 bands (right) on the 20 <sup>th</sup> of March 2018. Two fields with distinct level of FAW damage (Davis score 3 and 7) and similar context are compared.....	45

Figure 23: VIs response (left) and surface reflectance of the ten original Sentinel-2 bands (right) on the 24 <sup>th</sup> of January 2018. Two fields with distinct level of FAW damage (Davis score 1 and 9) and similar context are compared.....	46
Figure 24: VIs response (left) and surface reflectance values of the ten original Sentinel-2 bands (right) to three levels of FAW damage (Davis score 1, 5 and 9) on the 24th of January 2018. The mean value of all the pixels in each category is considered. ....	47
Figure 25: NDRE response between healthy maize fields and damaged fields that are in a context where confounding factors are disturbing the signal. The trajectories are analysed between the 24th of January 2019 and the 28th of February 2019 for fields in Chipinge and between the 1st of February 2019 and the 3rd of March 2019 for the fields in Makoni.....	48
Figure 26: Mean VIs response (left) and mean water indices response (right) for each category of maize/sorghum flood damage on the 25 <sup>th</sup> of March 2019.....	50
Figure 27: Mean surface reflectance values of the ten original Sentinel-2 bands for the five categories of flood damage on the 25 <sup>th</sup> of March 2019 .....	50
Figure 28: Mean VIs response (left) and mean surface reflectance values of the ten original Sentinel-2 bands (right) for the five categories of flattened damage on the 25 <sup>th</sup> of March 2019 .....	51
Figure 29: Pictures taken after Idai illustrating flattened crop fields in Chimanimani, Zimbabwe on the 17 <sup>th</sup> of March 2019 (left, credits to Xinhua from “New China”) and Beira, Mozambique (right, credits to Thomson Reuters, nd.) .....	52
Figure 30: Distribution of the bands/VIs response for each category of flood damage around the median. The graph is composed of a boxplot and a mirrored distribution of the data (blue). ....	52
Figure 31: Distribution of the bands/VIs response for each category of flattened damage around the median. The graph is composed of a boxplot and a mirrored distribution of the data (blue). ....	53
Figure 32: Visualization of the best combination of features that separates the different levels of flood damage. ....	55
Figure 33: Visualization of the extreme classes (first level of damage in green and last in red) of flood damage on four features (GCI, NDWI2, NIR, CIRE) and two combinations of features (Band 8 - Band 2 and Band 8 and Band 12), on the 25th of March 2019.....	56
Figure 34: Comparison of the SWIR channel ( $1610 \pm 45$ nm) of the 28th of February 2019 and the 25th of March 201 over the study area of Chipinge. The five categories of flood damaged fields are represented in five colours (in order: green, blue, yellow, orange and red) and the two extreme classes are compared on the two dates. 57	57
Figure 35: Delta of surface reflectance in the SWIR channel ( $1610 \pm 45$ nm) between the 28th of February and the 25th of March over the study area of Chipinge. The five categories of flood damaged fields are represented in five colours (in order: green, blue, yellow, orange and red) and the two extreme classes are compared. ....	58
Figure 36: Delta of SWIR surface reflectance between the 28th of February and the 25th of March 2019 in Ward 20 (left), Ward 16 (middle) and Ward 18 (right) of Chipinge. The five categories of flood damaged fields are represented in five colours (in order: green, blue, yellow, orange and red).....	59
Figure 37: Crop land mask obtained over the tile covering Chipinge with one date Sentinel-2 image as input (30th of October 2018) and 2 classes of landcovers namely crop (maize, sorghum and other crops) and non-crop as well as two zoomed in sections (bottom).....	60
Figure 38: Crop type mask obtained over the tile covering Chipinge with one date Sentinel-2 image as input (28th of October 2018), a crop mask obtained on the 30th of October 2018 and 3 classes of landcovers namely maize, sorghum and other crops. Two zoomed in sections are also displayed and one is shown with a Pléiades image underneath (bottom right). .....	62
Figure 39:Visualization on the 28 <sup>th</sup> of February Sentinel-2 image of the National park (middle top) and fields in Ward 16 (middle bottom) as well as on Google Earth imagery (right).....	64
Figure 40: Crop type map generated with two dates Sentinel-2 images as input (30th of October 2018 and 28th of February 2019) and in situ training data containing 10 classes of land covers. Each class was stratified and split	

into subclasses according to wards and problematic areas. There are three zoomed in sections of the Natural Park (left), Ward 16 (middle) and Ward 18 (right). ..... 65

Figure 41: Crop type map generated over ward 18 of Chipinge and obtained with one Pléiades image as input (25th of March 2019) and a shapefile that contained 9 classes of landcovers. ..... 67

## List of Tables

Table 1: Sentinel-2 bands used in this study and their respective wavelengths .....	34
Table 2: Indices used in this study for the detection of the damage on maize and sorghum .....	35
Table 3: Water indices tested in this study for the detection of flooded damage on maize and sorghum. ....	36
Table 4: Mean values and standard deviation values for healthy fields and damaged fields that are in a context where confounding factors are disturbing the signal between the 24th of January 2019 and the 28th of February 2019 for fields in Chipinge and between the 1st of February 2019 and the 3rd of March 2019 for the fields in Makoni.....	49
Table 5: Correlation values between the spectral features tested in this study. The VIs being highly correlated, it is not summarized here. The combination of features with a correlation that is less than 0.5 are highlighted in green.....	54
Table 6: Delta of SWIR surface reflectance values of flooded fields with a damage score of 1 (green) and 5 (red) and the average value of the four represented plots of each category.....	58
Table 7: Confusion matrix between the cropland mask of Figure 37 and the in situ validation dataset. Precision, recall, F-score and overall accuracy were computed based on the matrix. ....	61
Table 8: Confusion matrix between the crop type mask of Figure 38 and the in situ validation dataset. Precision, recall, F-score and overall accuracy were computed based on the matrix. ....	63
Table 9: Confusion matrix between the crop type mask of Figure 40 and the in situ validation dataset. Precision, recall, F-score and overall accuracy were computed based on the matrix .....	65
Table 10: Confusion matrix between the crop type mask of Figure 41 and the in situ validation dataset. Precision, recall, F-score and overall accuracy were computed based on the matrix .....	67
Table 11: Reduced confusion matrix to cereals (Maize + sorghum) and other landcovers of the classification illustrated in Figure 40.....	68

## Acronyms and Abbreviations

ANN	Artificial Neural Network
ANOVA	Analysis of Variance
AOT	Aerosol Optical Thickness
CABI	Centre for Agriculture and Biosciences International
CIMMYT	The International Maize and Wheat Improvement Centre
CIRE	Red-Edge Chlorophyll Index
CNES	French Space Agency
DEM	Digital Elevation Model
ESA	European Space Agency
EVI	Enhanced Vegetation Index
FAO	Food & Agriculture Organization
FAW	Fall Armyworm
GCI	Green Chlorophyll Index
GDP	Gross Domestic Product
HiRI	High-Resolution Imager
LAI	Leaf Area Index
MACCS	Multi-Sensor Atmospheric Correction and Cloud Screening
MLH	Maximum Likelihood
MODIS	Moderate Resolution Imaging Spectroradiometer
MSAVI	Modified SAVI
MSI	Multi-Spectral Instrument
NDVI	Normalized Difference Vegetation Index
NDWI	Normalized Difference Water Index
NIR	Near Infrared
NR	Natural Regions
OA	Overall Accuracy
OBIA	Object-Based Image Analysis
ONI	Oceanic Niño Index
OTB	Orfeo Toolbox
OWT	Oriented Watershed Transform
RDVI	Renormalized Difference Vegetation Index
RF	Random Forest
S2	Sentinel-2
SAR	Synthetic Aperture Radar
SAVI	Soil-Adjusted Vegetation Index

SCI	Scene Classification Image
SSA	Sub-Saharan Africa
SVM	Support Vector Machine
SWIR	Short-Wave Infra-Red
UAV	Unmanned Aerial Vehicle
USAID	United States Agency for International Development
VHR	Very High-Resolution
VI <sub>s</sub>	Vegetation Indices

## I. Introduction

Smallholder farmers in Sub-Saharan African countries are facing more and more challenges in terms of agriculture. Not only the lack of mechanization remains a problem to feed the population that continues to grow but in addition, external threats increase the risk of food insecurity and famine in some countries.

Indeed, let's start by mentioning the arrival in Africa in 2016 of Fall Armyworm (FAW), native of the Americas. In just three years, these insects have colonized almost the entire continent of Africa and have now arrived in Asia. Maize, which turns out to be the main host plant of FAW, is also the most cultivated crop in Africa and remains the most important staple food. The defoliation damage of FAW causes yield losses and therefore this insect represents a great threat to overcome.

Unfortunately, FAW is not the only threat to smallholder farmers. Climate hazards are an increasingly common problem they face. More particularly this year, Zimbabwe suffers from the damage of a big dry spell that occurred during the maize growing season and was followed by a cyclone. These two extreme climatic events have caused significant damage and food insecurity in some areas, including the Chipinge District, which we will focus on.

Determining the extent of such damage, even at the district level, requires extensive field work and a lot of time where it is necessary to act quickly to deliver food aid. Being able to determine the extent of this damage quickly would be a real asset for the future because it seems that these extreme events will not diminish. It is here that remote sensing can represent a real solution to this problem. Indeed, monitoring crops remotely is a technique that has been used successfully for several years now. The availability of free access satellite imagery opens the door to these kinds of technologies for any developing country. Besides, in the past years, sensors have much improved in terms of spectral and spatial resolutions. Similarly, the use of Unmanned Aerial Vehicle (UAV) platform has seen its price decrease in the past years.

Therefore, this master thesis aims, in collaboration with CIMMYT who is actively working on these matters in Zimbabwe, to assess the feasibility of detecting damage on maize in two districts of the country using satellite imagery. It was also initially planned to use UAV imagery, but the administrative request did not go through. CIMMYT is working on the factors influencing FAW damage on maize and quantifying its impact on yield. The ground truth databases used in this master thesis belong to CIMMYT and were collected in partnership with GOAL.

This master thesis is composed of the following sections. As a start, a brief literature review on the matter will be detailed in the next section. It will begin with some definitions and explanations of what FAW is and then will be gathered information about relevant remote sensing applications. As a result of that, the objectives of this

work will be set in order to guide our investigations. The following section will detail our material we used and the methods we tested to evaluate the possibility of detecting and mapping damaged maize. The results will then be displayed and discussed in the last two sections.

## II. Literature review

This literature review is composed of 3 sections. First, general information about FAW will be gathered as well as its life cycle and its invasion and impacts in Africa. Thereafter, we will discuss FAW's current monitoring methods as well as the technical aspects of pest damage surveillance by remote sensing.

### A. The Fall Armyworm (*Spodoptera frugiperda*)

#### 1. History and migration behaviour

*Spodoptera frugiperda*, commonly known under the name of FAW, is an insect pest that is indigenous to the tropical and subtropical regions of the Americas. Johnson (1987) summarized the life history and migration behaviour of FAW in the western hemisphere: FAW was first a permanent resident of Central America and the northern parts of South America (Brazil and Peru included). The pest was first recorded in 1797 in the United States where it widely spread over the entire country and even southern Canada. In those regions, its distribution is seasonal due to its lack of diapause mechanism. The pest cannot survive to winter and therefore overwinter in mild climate to find sources of food, southern location of Florida and Texas included. Each spring, when the next growing season starts, the moth migrates from those regions to north. The destination actually depends on the prevailing winds and the availability of host plants (Ashley, 1986). Migration and year-round survival is possible where its host plants occur (Luginbill, 1928). This migratory behaviour among other characteristics classify *S. frugiperda* as a successful colonizing species. Indeed, the female moth is a strong flyer with the ability of travelling up to 100 km at night. Rose et al. (1975) recorded a flight of 1600 km from the south of Mississippi's state to southern Canada performed in 30 hours due to the right wind patterns. With a lifetime of two to three weeks, from the first instar to the end of its moth stage, it lays a maximum of 1500 to 2000 masses of 200 eggs directly onto the leaves. The pest occurs in outbreaks causing important yield losses which could exacerbate food insecurity in some countries, as a stress that come in addition to other ones (including drought and social instability) (FAO, 2018).

#### 2. Description of *Spodoptera frugiperda*

The FAW is a species in the order *Lepidoptera* and in the family *Noctuidae*. A description of the pest from egg-to-adult seems necessary to recognize and differentiate this insect from others in the field. John L. Capinera (2000) published a detailed fact sheet of *Spodoptera frugiperda* (J.E. Smith).



Figure 1: Egg mass of the Fall Armyworm, *Spodoptera frugiperda* (J.E. Smith) (John L. Capinera, 2000).

The egg mass is spread over the foliage and covered in a layer of greyish hairs. The egg is dome shaped and measures about 0.4 mm in diameter and 0.3 mm in height. The egg stage lasts for 2 to 3 days during summer (Figure 1).

The larvae go through six instars and grow from about 1 mm length to 35 mm. Newly hatched larvae have a black head and a light-green body (Figure 2). In the second instar, the head capsule turns orangish. Its dorsal surface takes on its brown colour from the 3rd stage and lateral white lines begin to form.



Figure 2: Newly hatched larva of the fall armyworm, *Spodoptera frugiperda* (J.E. Smith) (John L. Capinera, 2000).



Figure 3: Mature larva of the fall armyworm, *Spodoptera frugiperda* (J.E. Smith) showing light-coloured inverted "Y" on the front head (John L. Capinera, 2000).

During the following instars, the head turns to a reddish-brown marked with a white inverted "Y" (Figure 3). The dorsal surface of the body is marked with 4 dark spots on the eighth abdominal segment and the ventral side is paler.

### 3. Life Cycle and Damage on Maize

The caterpillar feeds on leaves, stem and may also attack the growing point of a plant which leads to wilting and death. In the Americas, it is known that the pest feeds on

more than 80 crop varieties including important staple food as for example maize, rice, sorghum and sugarcane (Day et al., 2017). Maize is the most widely harvested crop in Africa but also the one that is the most damaged by FAW. Knowing the life cycle of the pest contributes to a better understanding of the damage's occurrence and severity on maize.

First, it is necessary to have a general understanding of maize growth stages since the type of damage will vary. After emerging, the maize plant goes through 3 main stages: Vegetative (V), Tasselling (VT) and Reproductive (R) (Zadoks et al., 1974). The V stage is the number of maize leaves with a leaf collar and can be characterized by the early and late whorl stage (Figure 4).

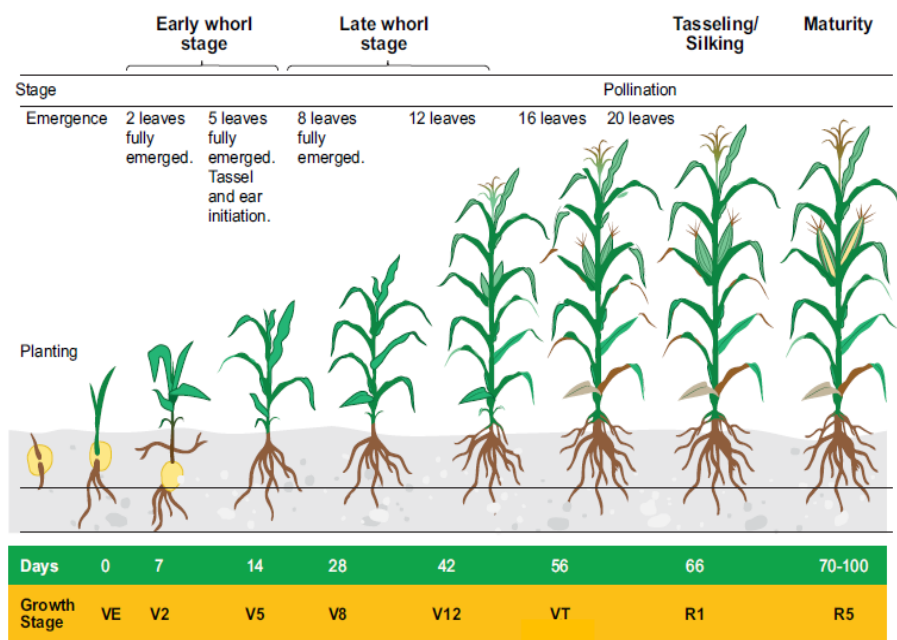


Figure 4: Maize growth stages, modified from Clarrie Beckingham, 2007, (Prasanna et al., 2018).

On the first three days of the larva's life cycle, masses of eggs are laid on the under surface of a leaf near the base of the plant or in the whorl.

During its first instars, the young larvae feed on the undersides of leaves. Bottom leaves are always the first being damaged. Young and tender maize plants are FAW's favourite food. While the maize is not yet in the tasselling stage, FAW's favourite spot to stay and to feed is curled up in the whorl. Early-instar FAW damage is in the form of small window pane. The young larva sucks chlorophyll from the leaves leaving a transparent window (Figure 5).



Figure 5: Early-instar FAW damage on maize leaves in the form of small window panes (Prasanna et al., 2018)

By day six to fourteen, the caterpillar will have reached growth stage three to six (FAO, 2018). At this point, the larvae will have developed its jaw and can cause the most extensive defoliation resulting in ragged holes in the leaves.



Figure 6: Emerging tassel that will push FAW larvae out of the whorl (Prasanna et al., 2018)

Figure 7: Ear/cob damage caused by FAW larva (Prasanna et al., 2018)

The growing point of maize is below ground until the end of the early whorl stage (about V6) (Prasanna et al., 2018). From the late whorl stage, the larvae will make their way to this point destroying the plant's potential of growing and form reproductive structure (Capinera, 2017). Early detection of FAW is therefore essential to prevent significant yield loss. The emerging tassel will push the larvae out of the whorl (Figure 6) and the pest will then migrate to the base of the developing ear/cob and the tip of the ear (Prasanna et al., 2018). Ear damage results in chewed kernels and visible frass (Figure 7). Eventually, pupation will occur under the ground for about eight to

nine days and the cycle ends with the release of the adult moth (FAO, 2018). When the first generation of FAW infests a maize plant at V2 stage, the pest can complete its entire development and the second generation can re-infest the same maize plant at reproductive stage. The probability of this happening is particularly high in places where FAW is endemic (Prasanna et al., 2018).

#### *4. Climate conditions and effect of temperature*

The invasion of FAW depends on weather. Wet and cool spring, with abundant rainfall and thus lush vegetation are favourable conditions for an expansive FAW population. When the weather gets warm and humid, propagation of FAW is probable and can cause severe damage to summer crops (Lunginbill P., 1928).

The development time from egg-to-adult of FAW is influenced by temperature. Barfield et al. (1978) found a mean development rate ranging from 66.6 days at 15.6°C to 18.4 days at 35°C. Temperature also influences the number of mating. A peak is observed between 25 and 30°C with few mating occurring around 15°C (Simmons and Marti, 1992).

#### *5. Invasion and Impacts in Africa*

In an evidence note compiled and published by the Centre for Agriculture and Biosciences International (CABI) in 2017, Day et al. (2017) describe the appearance of the pest in Africa and assess the potential impacts if left uncontrolled. In early 2016 were reported the first signs of FAW in Nigeria and the Democratic Republic of São Tomé and Príncipe (Goergen et al., 2016). The cause of the invasion is not yet confirmed, but the hypothesis is by commercial aircraft before widespread dispersal by the wind. Day et al. (2017) state that, as of August 2017, 28 countries have confirmed the presence of FAW, including Zimbabwe, and a further 9 countries suspect its presence. In early 2018, all African countries (except 10 northern states territories) have reported an infestation (FAO, 2018). In 2019, Egypt and Asian countries have reported its presence (FAO, 2019). Maize is the most widely grown crop in Africa and accounts for almost half of the calories and protein consumed in eastern and southern Africa, and one fifth in West Africa (Macauley, H., 2015).

FAW is believed to become endemic in Sub-Saharan Africa (SSA) due to the particularly suitable agroecological conditions. While in most areas of North America FAW can't survive in cold winter, generations of the pest can be continuous throughout the year in SSA wherever host plants are available, especially where there are two rainy seasons and thus cropping seasons (Prasanna et al., 2018).

Two strains of FAW have been identified in the Americas based on the larval host plants. One strain preferably feeds on corn ("C strain"), cotton and sorghum while the second one tends to favour rice ("R strain") and grasses (Pashley, 1986; Pashley, 1988). Morphologically, the two are the same. The differences appear in their pheromone composition, mating behaviour and their development relative to the host

plants (Dumas et al., 2015). Whether the two strains are present all over Africa is still under investigation, though, recent studies are reinforcing the hypothesis. The two strains were present in the first 2016 outbreaks in Nigeria and São Tomé (Goergen et al., 2016). Nagoshi et al. (2017) conducted genetic analysis on FAW present in the maize fields in Togo. The genetic marker data indicate that both strains are present in the country, but the corn strain is the predominant FAW subpopulation present in the Togolese collections. The similarities of the mitochondrial haplotype configuration with the one from the Caribbean region and eastern coast of the United States suggest that those areas are the origin of the Togolese infestation. A study in Uganda (Otim et al., 2018) also supports the presence of the haplotypes representative of both strains. Studies have not yet confirmed if both strains were introduced together or separately. Moreover, as those populations are not representative of the entire African population, further research is needed to better understand the genetic characterization for crop resistance development.

Although the presence of the 2 strains is confirmed, preference for maize is dominant. Threats of food insecurity for more than 300 million African smallholders exist and studies start to quantify possible yield losses. Day et al. (2017) conducted a survey across Ghana and Zambia after the full growing season of 2017 to estimate yield losses due to FAW from farmers' perception. They estimated an average yield loss of maize in Ghana of 45% (range 22–67%) and in Zambia of 40% (range 25–50%). Without any means of control, 21–53% of the annual production of maize averaged over a three-year period is estimated to be lost in just 12 of Africa's maize-producing countries. The pest will affect natural capital, through yield losses; and financial capital, through the effect on income and the increased production's costs.

Impacts of yield were assessed following a rigorous scouting protocol at the scale of smallholders' farmers in Eastern Zimbabwe (Baudron et al., 2019). Their estimation of FAW damage on yield (11.57%) is much lower than what the studies based on farmer's perception reported. The levels of FAW damage in this study (32–48%, depending on the estimate used) were, however, in the same range as previous reports (Kumela et al., 2019).

Other sectors are threatened as well. Some SSA's seed companies have reported losses in their maize seed production fields during the 2017 crop season. International trade is also jeopardized due to the risks of invasion. Informal reports indicate that FAW has been intercepted at quarantine points in Africa and Europe (Prasanna et al., 2018).

Another dangerous emerging impact in Africa concerns environmental and human health due to hazardous and unguided applications of chemicals. Continued exposures to pesticides are dangerous especially for women and children who primarily manage agricultural work in African fields. In terms of environment, unwanted

damage to natural enemies and predators of FAW hinder sustainable management of FAW and other pests (Prasanna et al., 2018; Harrison et al., 2019).

### B. Current method of monitoring FAW

FAW monitoring has different purposes. One objective is to track the presence and movement of the pest within a specific area (it can be at local scale, regional or more). One month before planting, a pheromone trap is placed near fields to catch male moths. The number of individuals is counted and recorded for the tracking (Prasanna et al., 2018).

At farm scale level, scouting aims to identify the presence of FAW in the field in order to take actions against the pest. As mentioned in the previous section, FAW has a fast-growing development and a wide ability of spreading. Early detection of the pest is the key to avoid the growing point of the plant to be destroyed. As for now, the main method of monitoring the pest is field work and scouting. FAO and CABI established monitoring methods to help farmers detect signs of FAW presence and allow them to act as early as possible.

For a start, it is suggested that farmers should enter their fields at last 2 weeks after planting and then continuously at least once a week and at best 3 times a week if they observe a fast-changing dynamic. The growth stage of the maize must be first identified. Although the scouting protocol will be the same, the damage one will be looking at differs with the maize whorl stage. Not all fields have to be scouted but if fields were planted under different conditions (time of sowing, varieties, intercropping) then each type of field should be sampled. We can find different scouting protocols in the literature. FAO (2018) suggests in their guide to randomly sample a total of 20 plants per field, avoiding 2 meters from the edges for border effects. Of these 20 plants, information about the growth stage of the maize, leaves damage, egg mass, presence of natural enemies, soil conditions, etc. must be recorded. Another protocol of scouting is recommended in the guide of the United States Agency for International Development (USAID) and CIMMYT. The sampling should be random and follow a 'W' pattern avoiding 5 meters from the borders. The assessment of the level of FAW infestation (expressed as a percentage of plants displaying signs of damage) is set on 5 different locations of 10-20 analysed plants. The scout should look for distinct damage symptoms at the different growth stages of the maize plant.

Identifying the presence of the FAW early presents multiple benefits: at early whorl stage, the growing point of the maize is still below ground; it is easier to target the whorl with pesticides and control early instars of the larva; pesticide exposure is lower since the spraying is not yet overhead (Prasanna et al., 2018).

Field monitoring shows advantages in terms of farmer's increasing knowledge of their field as they will learn about its variability (FAO, 2018). This method is, however, labour intensive, time consuming and not always appropriate for farmers whose fields are

remote. Furthermore, the fight against FAW being recent in Africa, information and training still need to be transmitted to farmers in order to accurately recognize the caterpillar among others in the field and assure an integrated pest management.

### C. Remote Sensing Monitoring: Crop Disease and Pests Detection

The use of spectral features to detect abiotic changes in plants has been studied and used for a few decades. This practice is regularly used for small case studies. Today, the recent development in satellite technologies has spawned more and more access to various data sources potentially enabling researchers to early detect and monitor crop disease and pest damage over a large-scale area. Detecting FAW on maize using this method could offer a rapid, non-destructive and effortless tool to farmers to tackle this invasive pest.

#### 1. *Resolution of remotely sensed data*

There exist a wide range of platforms and sensors available for data acquisition. Their specifications will determine the spatial, spectral, temporal and radiometric resolutions of the remotely sensed data. As part of disease and pest damage detection, spectral and spatial resolutions are the ones we are the most interested in. The temporal resolution is of great interest as well.

The spectral resolution refers to the number and width of spectral bands the sensor will sample from the electromagnetic spectrum. There are 2 types that have been used in this subject. First, hyperspectral systems can have hundreds of narrow bands making them very useful in the sector of agriculture to detect precise and unique spectral signature of small objects, impacts or variations. Hyperspectral sensors have been used and tested numerous times to detect pest and disease damage. As for instance, early detection and differentiation of sugar beet diseases (*Cercospora* leaf spot, sugar beet rust and powdery mildew) was accurately performed on stations based on hyperspectral reflectance (Rumpf et al., 2010). Spectral characteristics of sugar beet leaves were assessed by greenhouse experiments and the chlorophyll content was measured using a handheld non-imaging spectroradiometer (*Ibid.*). Another example is Behmann et al. (2014) who developed a method to early detect and visualize multiple levels of senescence on barley due to drought stress from series of hyperspectral images. However successful, there are two downsides to consider with this type of data. First, the high number of narrow bands adds complexity and spectral redundancy must be taken into account while processing the data. Next, hyperspectral data availability is very limited, and both of the previous experiments were conducted in controlled site/greenhouse conditions. The development of high resolution multi-spectral satellite sensors around the world led to the emergence of studies assessing the capability of multispectral sensors to detect stress in plants. These sensors will typically measure around 4 to 10 spectral bands for each pixel of the image. The bands are usually in the visible and near infrared (NIR). Some sensors include Red-edge channels in their band settings which have shown to be particularly

sensitive to biophysical changes (Oumar and Mutanga, 2013). In a complex environment such as smallholders' African landscape where one specific type of damage has to be distinguished from other damage often occurring at the same time, the spaceborne sensor's channels should allow the differentiation among the different spectral responses. For example, Yuan et al. (2017) assessed the potential of seven very high-resolution satellite (Geo-Eye, Ikonos, Quickbird, Spot 6, GF-1, Rapideye and Worldview-2) in detecting and differentiating powdery mildew, yellow rust and aphid in winter wheat. They simulated the spectral response of the sensors' channels based on plants' canopy hyperspectral measurements. The results showed overall great potential for all multispectral sensors, but a certain extent of confusion stayed in identifying healthy, powdery mildew and aphid classes. This study remains a simulation but the highlighted difficulties in detecting damage in a complex environment should be taken into account.

To further discuss the potential of multispectral sensors, the spectral resolution must be considered together with the spatial resolution. This one is a measure of the smallest object that can be resolved by the sensor or the linear dimension on the ground represented by each pixel (Shunlin et al., 2012). Sensors can therefore be sorted according to their spatial resolution as follows: coarse resolution ( $> 1000$  m), medium resolution (100-1000m), high resolution (5-100m) and very high resolution ( $< 5$  m). Given the fact that stresses often appear at the plant scale and that pest and disease damage typically occur patchy in a field, only high and very high resolution sensors can be considered for this application.

The temporal resolution is a measure of the frequency with which a sensor revisits the same part of the Earth's surface. The frequency characteristics are determined by the design of the satellite sensor and its orbit pattern (Shunlin et al., 2012). The revisit time can be daily, weekly or even monthly. Considering the crop cycle over seasons and the fast-changing dynamics in terms of stresses, the shorter the temporal resolution, the better. A quick revisit of an area will allow monitoring changes in the spectral responses over time assuming the availability of cloud free images.

The combination of these three requirements already exists among available sensors and some have shown promising results. For instance, Franke and Menz (2007) performed a spatio-temporal analysis of the infection dynamics of powdery mildew and leaf rust in wheat on a test site of 6 ha with very high resolution images from Quickbird satellite. Its multispectral sensor has three bands in the visible (blue, green and red) and one in the NIR with a spatial resolution of 2 m and a revisit time of 1-3.5 days depending on latitude. The detection at early growth stage was difficult and showed a low accuracy (56.8%). However, the result of later growth stages and high rate of infection were encouraging (88.6%). Detection and mapping of powdery mildew on wheat were successfully performed (overall accuracy (OA) of 79%) using high-resolution multispectral satellite images from SPOT-6 with a single date image when the disease was fully expressed (Yuan et al., 2014). The satellite also has three visible

bands (blue, green and red), one NIR band and a spatial resolution of 6 meters. RapidEye satellite has a fifth band in the red-edge and a spatial resolution of 5 m. Adelabu et al. (2014) used RapidEye to try to discriminate multiple levels of insects defoliation in mopane woodland in Botswana. Using two different classifiers, results showed that the integration of information from red edge band increases accuracy in all analysis performed in the study.

All these results suggest the potential success of using good quality data of high to very high resolution multispectral sensors for the detection of FAW's defoliation damage on maize. However, one must note that the studies found in the literature to detect crop damage were conducted on controlled stations. It should also be noted that, even though acquiring data from the satellites cited above is cheaper, it can remain costly for farmers.

## *2. The potential of Sentinel-2 satellites*

Sentinel-2 (S2) mission is part of the Copernicus initiative led by the European commission and implemented partly by the European Space Agency (ESA). The aim is to provision operational monitoring information for environment and security applications. The mission objectives of S2 is to provide systematic global acquisitions of high temporal and multi-spectral resolution imagery for the observation of vegetation and production of land-cover/land change maps (Drusch et al., 2012). The Sentinel data products are available for free via a simple self-registration thanks to the data policy adopted for the European Copernicus Earth Observation program (ESA, n.d.).

The sensor offers three visible bands (blue green and red) and one NIR at a spatial resolution of 10 m and six bands (in the red-edge and short-wave infra-red (SWIR)) at 20 m. Three bands at 60 m are dedicated mainly to atmospheric corrections and cirrus-cloud screening (ESA, nd). Those characteristics in combination with a high revisit frequency of 5 days make S2 satellites particularly suitable for vegetation monitoring.

Its potential has been evaluated for the discrimination of Coffee leaf Rust infection levels at leaf scale under controlled station conditions (Chemura et al., 2017). Field spectra were resampled to simulate the channel settings of S2. The results highlighted the important discriminating power of bands in the red and red-edge with an accuracy of 79.4%. Another research showed S2's capacity to detect low severity mite infestation in grapes (Mohite et al., 2018). Reflectance data from healthy and low infested grape leaves were used to simulate 8 bands of S2 at 10 m and 20 m. Classifications results using the simulated bands came out with an accuracy of 89.12%. A validation of the simulated S2 based algorithm with ground observations and available S2 images delivered an accuracy of 83.33%. This manifests S2's potential for the detection of low infestation. In general, S2 multi-spectral instrument (MSI) seems particularly suited for stressors' detection especially thanks to its red-

edge bands that seem to provide useful information to detect vegetation response to environmental stress (Liu et al., 2018).

### 3. *Spectral Features: Wavebands and Indices*

The very basis of disease and insect monitoring is the spectral response to physiological stresses and plant cell structure changes. Sensing diseases and pests damage on crops remotely requires to initially link the spectral responses to damage severity. Variation in the visible spectrum is influenced by the photosynthetic pigments while the reflectance in the near-infrared is influenced by the structural properties of the leaf (Barton, 2012).

That being said, one can understand that what we are really interested in is the spectral response to degrees of defoliation damage. A first step would be to look at the spectral variation between healthy and infested samples. According to Yuan et al. (2017) who evaluated broadband sensors' discerning power for wheat diseases and insects, the blue channel failed to show significant statistical difference between healthy and infected samples for most sensors. The green band showed varying response levels from weak to medium ( $p$ -value < 0.01). Contrariwise, the red and NIR channels exhibited stronger discrimination power.

Now, one can also find in the literature targeted studies on the detection of defoliation damage. Erickson et al. (2004) assessed hail and wind defoliation damage to maize with remote sensing data in Indiana and Nebraska with the purpose of helping insurance companies. With adequate ground reference of different levels of crop damage, a classification was performed by extrapolating the spectral information to adjacent unknown areas of damage. Incremental differences in plant damage resulted in incremental differences in spectral responses. In order to identify the best subset of spectral bands to separate the different classes of damage, a criterion based on a distance measure such as the Bhattacharyya distance was used. It is a measure of the statistical separability of classes in a given feature space (Bruzzone and Serpico, 2000). A high Bhattacharyya distance between damage-level classes for a given band means a high chance that this band will be useful for separation. At wavelengths between 700 nm and 1400 nm where the reflectance is usually high due to green plant cells, there was less reflectance from defoliated plots compared to check. The average distance between values of each damage level was lower for the green and blue bands compared to the NIR. The distance was even greater for the red spectral band. These two bands provided the most discrimination among levels of damage. The greater the damage, the greater was the reflectance. Besides, it was found that the combination of the two bands seemed to provide much more information than either band alone since the different degrees of damage could clearly be distinguished. Classification performances were 10% higher for leaf loss during late vegetation stages than early reproductive stages.

As mentioned above, the red-edge spectral band also seems to provide useful information in terms of damage detection. Regarding our matter of study, Adelabu et al. (2014) assessed the ability of Rapideye's red-edge band to discriminate different levels of insect defoliation in an African Savanna. The results show that this added information increases the OA of about 20% opposed to when the red-edge channel was excluded.

More specific to FAW's defoliation damage, Zhang et al. (2016) assessed the response of biophysical parameters and spectral features to armyworm attack in maize. They compared the differences in reflectance between the levels of damage at a post-outbreak date of FAW and for the reflectance delta between two dates (before and after the outbreak). Four bands were evaluated: the blue, green, red and NIR from the HJ-1 satellite optical sensor characterized by a spatial resolution of 30 m. The results are consistent with what has already been said. The green band failed to show any response to insect damage for the single date approach as well as, with the blue band, for the two-date approach. The red and NIR bands showed stronger reflectance differences between healthy, slightly damaged and damaged samples.

All these observations lead us to retain the discerning power of the red and near-infrared bands. Sentinel-2 contains these two as well as 3 bands in the red-edge. As mentioned above, the red-edge has already shown satisfactory results in the detection of vegetation damage which encourages the use of Sentinel-2 for the detection of FAW's damage.

Other common features used for the detection of insect damage are the computation of vegetation indices (VIs) derived from sensors' original bands. Over the years of research in remote sensing, scientists have developed a wide range of VIs that quantify and qualify changes in vegetation properties. Bannari et al. (1995) state that the spectral response of vegetated areas presents a complex mixture of vegetation, soil brightness, environmental effects, shadow, soil colour and moisture. Numerous VIs have been developed during the last two decades in order to enhance vegetation response and minimize the effects of these factors.

The most common method to monitor vegetation status is the use of the Normalized Difference Vegetation Index (NDVI). The index is used to evaluate the amount of green biomass in vegetation. It is measured as the ratio of the difference between the NIR ( $\rho_{NIR}$ ) and red reflectance ( $\rho_{Red}$ ) over the sum of both reflectance (Rouse and Haas, 1974).

$$NDVI = \frac{\rho_{NIR} - \rho_{Red}}{\rho_{NIR} + \rho_{Red}}$$

Defoliation damage will result in a decrease of the NDVI value which is between 0 and 1 due to the normalization. This index is not only related to canopy structure and leaf area index (LAI) but also to canopy photosynthesis (Xue and Su, 2017). NDVI is, however, known to be sensitive to soil brightness effects, soil colour, atmosphere, cloud and shadows. Therefore, other VIs were developed to overcome these effects. The soil background brightness can particularly be an issue when the vegetation is sparse or, in our case, when the vegetation is defoliated. Red radiation increases when the soil is visible (Ibid.). The Soil-Adjusted Vegetation Index (SAVI) was therefore developed to overcome the soil effect (Huete, 1988).

$$SAVI = \frac{(\rho_{NIR} - \rho_{Red}) * (1 + L)}{(\rho_{NIR} + \rho_{Red} + L)}$$

L is the soil brightness correction factor which improves the sensitivity of the NDVI. The range of L is from 0 to 1 and the value is determined by the environmental conditions. It is close to 1 when the vegetation coverage is high and close to 0 otherwise. This means that when the soil is bare, SAVI is equal to NDVI. Therefore, a modified SAVI (MSAVI) was developed (Qi et al., 1994) where L is a function of the soil line that reduces the effect of bare soil. Since establishing a function of the soil line was the difficult parameter to find, Qi et al. (1994) solved the problem and developed the Modified Secondary Soil-Adjusted Vegetation Index (MSAVI2) which has a simpler algorithm and is expressed as follows:

$$MSAVI2 = 0.5 * [(2\rho_{NIR} + 1) - \sqrt{(2\rho_{NIR} + 1)^2 - 8(\rho_{NIR} - \rho_{Red})}]$$

This index is useful in the analysis of plant growth, desertification research, grassland yield estimation, LAI assessment, drought monitoring and the analysis of soil erosion (Ibid.).

Atmospheric sensitivity of the NDVI is considered into the Enhanced Vegetation Index (EVI) which was created for Moderate Resolution Imaging Spectroradiometer (MODIS) data by optimizing the signal in high biomass regions (high LAI) and reducing atmospheric influences. The EVI is more responsive to canopy variations and thus LAI, canopy type and architecture (Huete et al., 2002).

$$EVI = G * \frac{\rho_{NIR} - \rho_{Red}}{\rho_{NIR} + C1 * \rho_{Red} - C2 * \rho_{Blue} + L}$$

The equation takes the above form where  $\rho$  are atmospherically corrected reflectance, L is the canopy background adjustment and C1 and C2 are the coefficients of the aerosol resistance term, which uses the blue band to correct for aerosol influences in the red band. G is the gain factor which equals to 2.5 (Ibid.).

The list of VIs that have been developed as part of remote sensing is long, which requires a selection of the best subset of features for the detection of the different levels of FAW damage. In order to do so, Zhang et al. (2016) performed an analysis of variance (ANOVA) to test the sensitivity of the different spectral features. To avoid redundancy, a cross-correlation was implemented to features that passed the sensitivity test to assess the dependency of variables. Their results showed that the sensitivity of the VIs to FAW's damage was stronger than the original bands. Among the different VIs tested, it appears that the MSAVI shows, with a univariate model, the best response to pest damage with an accuracy of 0.79 followed by the Renormalized difference vegetation index (RDVI) and SAVI with a 0.71 accuracy. The RDVI modifies the NDVI to make the index more suitable for low to high LAI values (Ibid.).

#### *4. Classification methods and related features*

Once the appropriate subset of features is selected, it will serve as input for the classification of the maize according to its level of defoliation damage. The classification of an image is the process of assigning an attribute to pixels or objects based on a model build on training data. There are two main classification techniques in remote sensing: pixel-based or object-based.

The Object-based Image Analysis (OBIA) is performed in two steps: segmentation and classification. The segmentation is used to digitize the image and group small pixels into vector objects. The objects represent land features such as rivers, building, fields, etc. The next step, which is the classification, uses statistics such as the spectral, geometrical and spatial properties of the object to classify it into a feature class. To the best of our knowledge, the OBIA technique has not, or very little, been used for mapping insect or disease damage in fields on a regional scale and in addition, in a context of smallholder agriculture. Several reasons combined may justify this: the satellite spatial resolution and the landscape heterogeneity can be obstacles to the segmentation.

The classification step of OBIA and the pixel-based image classification can be either an unsupervised or a supervised technique. The unsupervised classification doesn't require to have input training data since an algorithm such as K-means creates clusters based on the pixel's properties. The next step is to interactively assign classes to (groups of) clusters. The supervised classification requires to initially train the algorithm with the spectral signature of representative samples of each class. The main types of classifiers used for damage mapping in the literature are machine-learning algorithms such as the Maximum Likelihood, the Artificial Neural Network, the Support Vector Machine and the Random Forest. The four were compared to one

another in several researches. First, an explanation of how they work seems appropriate.

a) Maximum Likelihood (MLH)

The MLH classifier stands on two principles. First, that the training dataset statistics of each class in each band is assumed to be normally distributed. Second, the MLH estimator coincides with the most probable Bayesian estimator. MLH calculates the probability that a pixel belongs to a specific class. The pixel is assigned to the class that has the highest probability thus the maximum likelihood (Yuan et al., 2014).

b) Artificial Neural Network (ANN)

The ANN is a nature-inspired technique. Just like the network of neurons in the human brain, each node of the ANN represents a neuron and each link represents the way two neurons interact. One popular ANN architecture is the multilayer perceptron. It is built with an input layer, one or more hidden layers (computation nodes) and one set of output nodes which is the output layer (Mas and Flores, 2008). Each neuron receives input signal from neurons of the previous layer and send the output to neurons of the successive layer (Rumpf et al., 2010). The output network is compared to the desired output and the network weights, which are synaptic weights for each link between the input and processing unit, are adjusted with an error-correlation rule. Mas and Flores (2008) reported other studies' comparison of ANN to conventional methods like MLH and its advantages. First, ANN has the ability to learn complex patterns, taking into account any non linear complex relationship between the explicative and the dependent variables. Secondly, ANN appears to be a robust solution in the presence of incomplete data since it has the ability to generalize noisy environment. Another point is that ANN includes previous knowledge in its network and realistic physical constraints into the analysis. Finally, there is no hypothesis on the distribution of the data used (e.g. normally distributed) which allows the incorporation of ancillary data such as the slope, texture, etc. In brief, when the feature space is complex and the source data have different statistical distributions, ANNs have been reported to perform more accurately (Ibid.).

c) Support Vector Machine (SVM)

SVM is a non-parametric algorithm. In its simplest linear form, it uses two classes that are linearly separable. The basic idea behind SVMs is to separate the two different classes of training samples through a hyperplane (Rumpf et al., 2010). The algorithm tries to maximize the margin, which is the distance between the closest training samples, or support vectors, and the hyperplane itself (Adelabu et al., 2014). SVM uses a kernel trick to project the training vectors into a multi-dimensional feature space and an optimization function to fit the optimal hyperplane that best separates the classes (Ibid.). Two parameters are used in SVM. The parameter "C" which is the

regularization parameter and is used to optimize the trade-off between margin maximization and error minimization and the kernel parameter  $\lambda$  (Ibid.). One main advantage of SVM is its ability to generalize well even with limited training samples. The major limitation seems to be related to the fitting of the kernel parameter (Mountrakis et al., 2011).

#### d) Random Forest (RF)

Random forest is a machine learning algorithm that is largely used in remote sensing. Multiple decision trees are built during the training phase and the majority of the trees is chosen by the random forest as the final decision. The trees (*ntree*) are constructed independently based on a random subset of samples from the training data and each node is split using the best user-defined number of features (*mtry*). The decision for the classification is then made by averaging the probabilities of a class assignment calculated by each tree. The multiple classification trees then vote by plurality on the correct classification (Breiman Leo, 2001).

All these four classifiers have been tested and compared in multiple studies with the aim of classifying levels of damage. The ANN classifier and MLH were compared on their ability to classify powdery mildew damage in winter wheat (Yuan et al., 2014). The overall accuracy was 10% higher for the ANN. In another case, ANN and SVM were tested for the early detection and differentiation of sugar beet diseases (Rumpf et al., 2010). Classification error was lower and lower for SVM. SVM seems to have a stronger optimization method (Ibid.). Indeed, SVM solves a quadratic optimization problem and the convexity of this problem ensures a unique and global solution. On the other hand, ANNs' solution is not convex and there are in general several local optima thus a good performance of the optimizer is not guaranteed (Ibid.). Finally, RF classifier and SVM were both used for the classification of defoliation damage in the African Savanna (Adelabu et al., 2014). Although the aim of their study was not to compare both algorithms, it was noticeable that SVM tends to slightly outperform RF and that seemingly thanks to its ability to work with a small number of samples. Random forest is generally known to need a larger number of samples to work its randomization concept well (Ibid.). On the other hand, RF seems to work better than SVM when the number of classes is important and shows low sensitivity to the number of inputs.

### D. Conclusion

FAW is an invasive pest that has colonized almost all the African countries and was reported in Asia in early 2019. Its defoliation impacts on maize result in yield losses and can exacerbate food insecurity in combination with other factors. The current ground monitoring method requires a lot of time and efforts as well as knowledge about the pest which is still not well known by African farmers. Remote sensing therefore seems a rapid and effortless tool to farmers to tackle this invasive pest. It can be noted

from the literature review that the detection of crop damage requires satellite to have at least a high to very-high spatial resolution and a short revisit time due to the fast stress dynamic changes. Also, the spectral characteristics of the satellite sensor should include bands in the visible, particularly the red which has shown promising results as well as a band in the NIR. Bands in the red-edge should also be considered since several studies have shown the red-edge potential in detecting vegetation damage. Sentinel-2 satellites meet all these characteristics and this imagery is, moreover, free of access which is an asset to consider in the case of smallholder agriculture. In terms of damage classification, a pixel based approach will be considered since it was widely tested in the literature and the segmentation required by an OBIA seems challenging in a smallholder agriculture landscape. Finally, several machine learning algorithms seem suited for the classification of damage, however, SVM and RF stand out and both have distinct advantages. SVM appears to work better with small training samples while RF seems to work better with a high number of classes and shows low sensitivity to the number of inputs. RF will therefore be considered for this work.

### III. Objectives

The main objective of this thesis is to assess the feasibility of detecting and mapping damaged maize using satellite imagery in a context of Sub-Saharan smallholders' agriculture. Two types of situation of damage are considered throughout this work.

First, FAW has already caused great damage on maize fields in Africa since 2016. Farmers are putting efforts in weekly monitoring the pest in order to detect FAW early enough. As reviewed above, several studies have shown encouraging results in mapping damage of disease or insects with satellite imagery, depending on the satellite's characteristics. Some features of Sentinel-2 seem promising in that way. The first objective of this thesis aims to assess the feasibility of detecting the damage of Fall Armyworm on maize using satellite imagery. The focus will be on maize fields in Zimbabwe where ongoing research activities are conducted by CIMMYT.

Second, as Cyclone Idai hit one district of the area of study Mid-March right after our field survey, the thesis also aims to investigate the feasibility of mapping the resulting cyclone damage and possibly estimate the crop loss of maize and sorghum in an emergency context.

To reach this goal, several tasks must be accomplished. First a sensitivity analysis of Sentinel-2 spectral bands and derived features to the types of damage must be accomplished in order to investigate the sensor's potential. The next step is to run a crop type classification and extract the maize/sorghum mask over the area of study. The possibility of mapping both types of damage will then be evaluated based on the results and our field observations.

## IV. Material

### A. Area of Study

#### 1. Geographic Location

This study was carried out in the eastern region of Zimbabwe, specifically in the Makoni and Chipinge districts (Figure 8). Both districts are part of the Manicaland Province. Makoni district, with its main town Rusape, is situated southeast of Harare, the capital of Zimbabwe, at about 170 kilometres by road and is close to the Nyanga National Park. This farming district covers an area of 7,834 km<sup>2</sup>. Chipinge is close to the Mozambique border and is located approximately 170 kilometres, by road, south of Mutare, the nearest large city and 450 kilometres southeast of Harare. Chipinge district covers an area of 5,220 km<sup>2</sup>. In each district, three wards (administrative subdivision of District) were chosen to conduct this study.

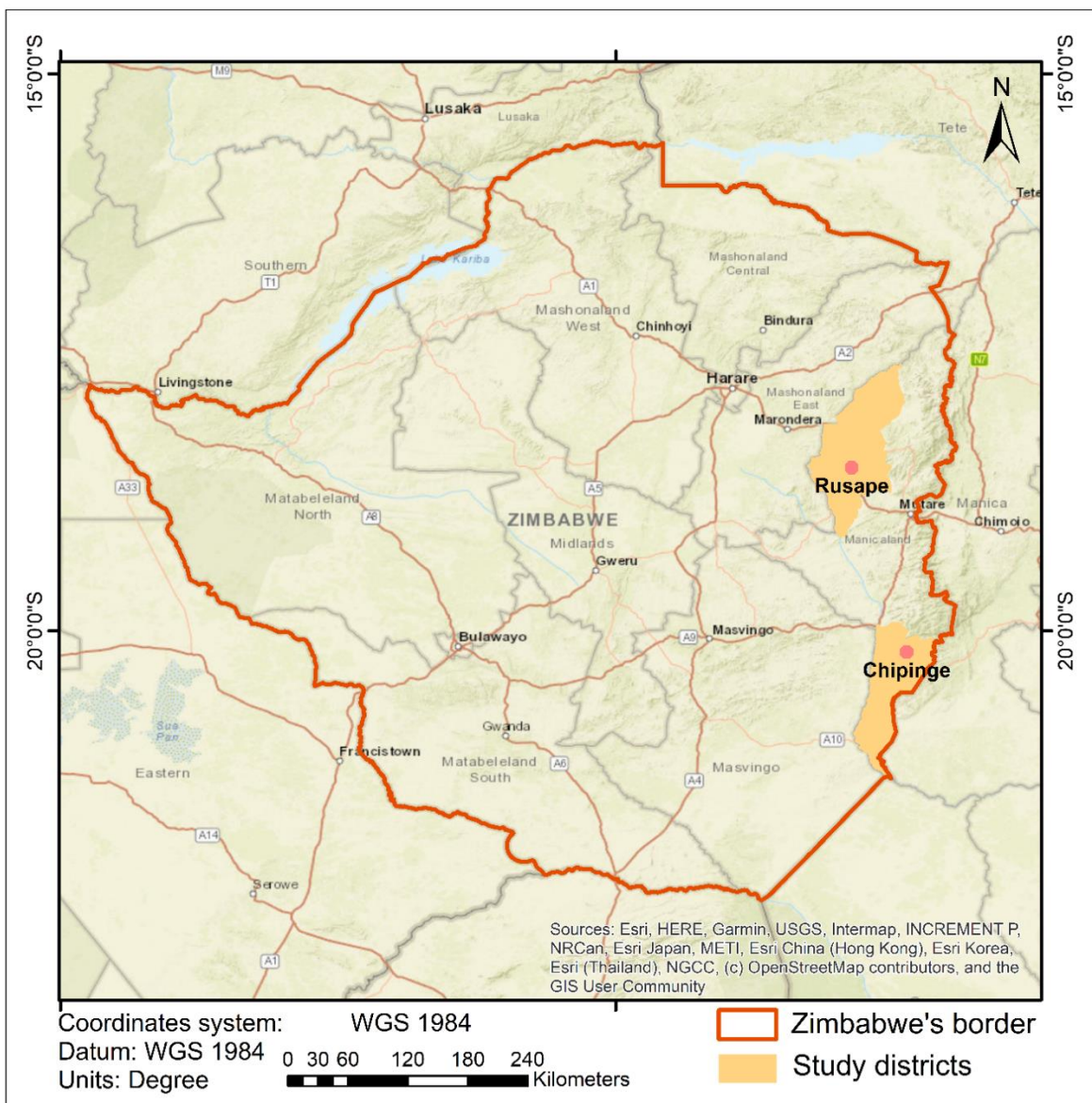


Figure 8: Geographic location of the two study districts, namely Makoni (main town Rusape) and Chipinge.

These study sites were selected because they consist of a great diversity of landscapes and are characterized by different agro-environmental conditions representing the diversity encountered in the country. The physical and climatic characteristics of these two districts will be developed below. Besides, the local partner of CIMMYT, GOAL is actively working in these districts and this study was able to benefit from their knowledge and support.

## 2. *Soil types*

The different soil types found are influenced by first, the parent material and second, the climate, in particular, the rainfalls and topography. Precambrian rock is one notable landscape feature in the greater part of the country. Its basement is made of four fifths of granite. The sandy soils found in most parts of Zimbabwe are derived from this granite parent material. These soils are easily eroded and do not retain water due to their coarse texture (Sanger et al., 2019). Richer clays and loam soils can be found on the basement of mafic gneiss and schists and represent the country's best soils. However, these high value agricultural soils are rare and the heavy rainfalls during a few months of the year result in runoffs and erosion.

## 3. *Climate and topography*

Zimbabwe's climate is intrinsically linked to its topography. Although the country is lying north of the Tropic of Capricorn, its varying elevation from the lowlands, plateau to highlands gives it according to Köppen classification, subtropical conditions (Cwa – Cwb) in most of the country and a semi-arid climate (BSh) in the south and southwest region. The highest peak of the country is in the eastern part of Zimbabwe, in Nyanga National Park. The mountain Inyangani is at an altitude of 2.991 m above sea level. From November until April, the eastern highlands receive the country's heaviest rains (more than 1000 mm annually) as they form a barrier to the monsoon winds coming from the Indian Ocean (Sanger et al., 2019). Temperatures vary from 11°C in winter to 24°C in summer. On the other hand, the lowlands receive little rains and the mean temperature reaches 38°C in summer. Winter is from mid-May to mid-August with a cool, dry and sunny season, followed by a brief period of intense heat from mid-August to the end of October.

Chipinge is at an average altitude of 1134 m and its landscape and elevation profile are highly contrasted within the district (Figure 9). Three Wards were selected by Baudron et al. (2019) as a relatively drier, intermediate and wetter Wards respectively (16, 20 and 18). Ward 18 is at an average elevation of 925 m and receives much more rain up in the mountains, while Ward 16 and 20 are in a more arid area, approximately 430 m above sea level.

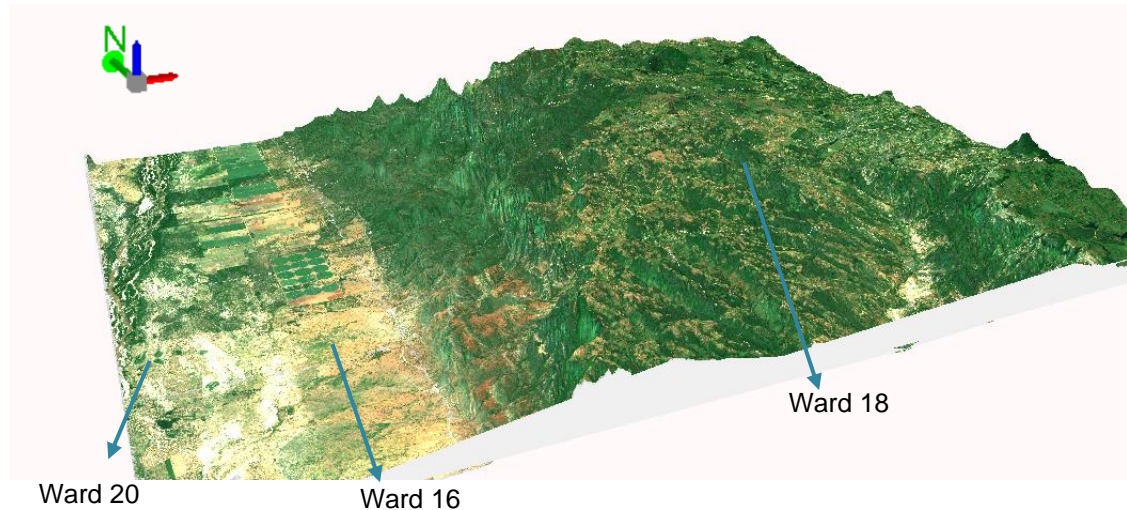


*Figure 9: Elevation model of the study area of Chipinge with a Sentinel-2 images of the 28<sup>th</sup> of February 2019 on top. The three Wards of study are Ward 16 and 20 that are at an average elevation of 430 m and Ward 18 that is at an average elevation of 925 m. DEM source: Aster, Nasa. <https://doi.org/10.5067/ASTER/ASTGTM.002>*

Zimbabwe is divided into five agro-ecological regions (Appendix 1) and Chipinge is on two of them. These natural farming regions (NR) were established based on their physical characteristics such as the rainfall regime, the topography, the soil quality and vegetation type among others. From NR I to NR V, the natural resources of the land are declining due to poorer physical conditions. Consequently, NR IV and V are promoted for livestock and dry resistant crops (Moyo, 2000). Wards 16 and 20 are in the NR III and IV which are characterized by a rainfall ranging from 500 to 700 mm/year and 450 to 650 mm/year respectively. These regions are subject to seasonal droughts and region IV is particularly exposed to severe dry spells during the rainy season. Ward 20 being along the Save River, it is composed of a large irrigation scheme. Ward 18 is in the NR I and receives more than 1050 mm rainfall per year which makes NR I the most adequate one for agriculture (Agritex, 2017).

Makoni is at an average altitude of 1372 m above sea level. Three Wards were selected based on their physical context as well (Baudron et al. 2019) that are a drier, intermediate and wetter Wards (26, 28 and 34). Ward 26 is at an average elevation of 905 m, Wards 28 is around 1175 m and Wards 34 is approximately around 1580 m. In terms of agroecological regions, Ward 34 is in between NR I – NR II and Ward 26 and 28 are part of NR II – NR III. Natural farming region II is well adapted to intensive cropping systems with reliable rainfalls from November to March/April that ranges from 750 to 1000 mm/year (Agritex, 2017).

Although the physical characteristics of these two districts seem favourable to agriculture, the 2018-2019 crop season has faced several challenges. Indeed, Southern African countries are facing El-Nin  conditions for the second time since the 2015-2016 season with some regions still suffering from its impact (FAO, 2019). Positive subsurface temperature anomalies across most of the Pacific have been

present for more than a year with a peak in October 2018, a minimum in early January 2019 and rose again afterwards. By definition, El-Niño is characterized by a positive Oceanic Niño Index (ONI) greater than or equal to +0.5°C. The most recent ONI value (February - April 2019) is +0.8°C (NOAA, 2019). El-Niño induced drought has led to delayed planting, erratic rainfalls and has potentially exacerbated outbreaks of crop pests such as FAW (FAO, 2019). The below-average rainfall across Zimbabwe and higher temperature in December, January and February (Figure 10) has badly impacted the crop growth leading to underdeveloped maize and even wilted crops (USAID, 2019).

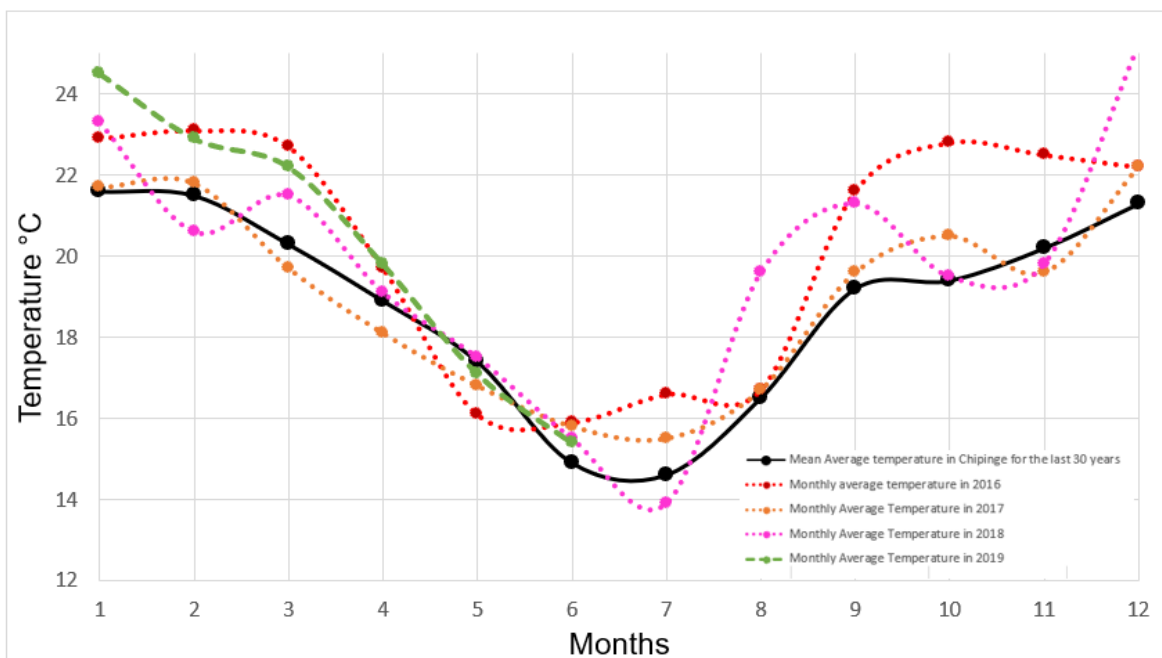


Figure 10: Mean average monthly temperature in Chipinge from 1985 to 2015, 2016, 2017, 2018 and 2019.

In early March, while the country was facing food security emergency due to the dry spell, forecasts announced a category 4 Tropical cyclone Idai in formation along the Mozambican coasts. This natural disaster hit on the 15<sup>th</sup> of March. It is in the form of a Tropical storm that Idai entered Zimbabwe causing heavy rains and floods which swept away homes and destroyed fields (Figure 11). Chimanimani, Chipinge and Mutare districts have been the most affected (International Federation of Red Cross, 2019).



Figure 11: Cyclone Idai impacts in Zimbabwe, picture posted by Goba C. on the chronicle 'My Zimbabwe News' on the 16<sup>th</sup> of March 2019.

#### 4. Characteristics of agriculture and maize harvesting calendar

Agriculture in Zimbabwe accounts for about 15% of the gross domestic product (GDP). Although the sector declined in the 21<sup>st</sup> century, more than one half of the total labour force is engaged in agriculture. The total agricultural area is divided between large-scale commercial farming and smallholders whose lands are considerably less fertile (Sanger et al., 2019). The most harvested crop is maize. It used to be produced in amounts that enabled exports of sizable quantities but since the decline of production in the 21<sup>st</sup> century, the country now fails to meet its domestic needs. Other food crops such as sorghum, wheat, millet, groundnuts, bananas and oranges are commonly produced. Commercial production is mainly tobacco, coffee, tea, cotton, etc. Chipinge main crops are maize, cotton and sorghum while Makoni's production is maize, groundnuts and tobacco.

Maize cultivation cycle is quite similar within the concerned agro-ecological zones (natural farming regions) as visible here (Figure 12). Sorghum is sowed mid-November and harvested during a short period at the end of April.

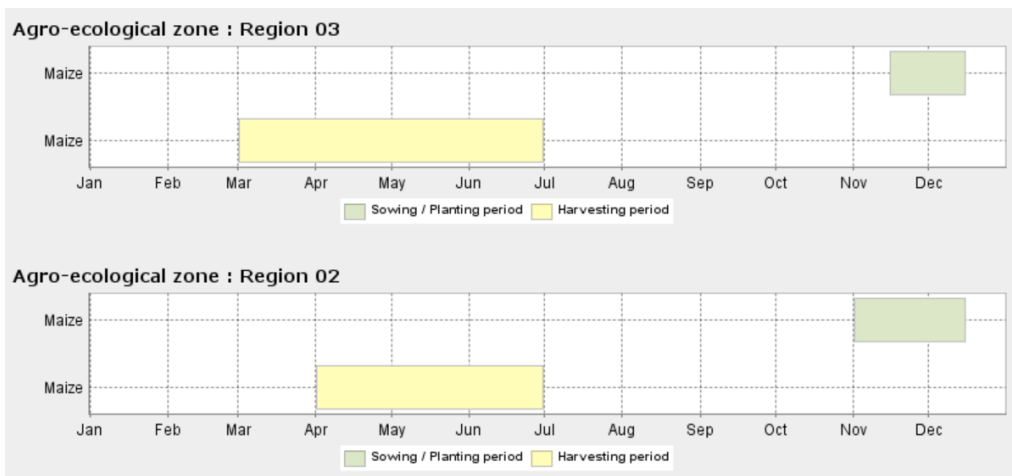


Figure 12: Maize cultivation cycle in agro-ecological regions (natural farming regions) II and III (FAO)

#### B. Data sources

In order to detect and map crop damage using satellite images, ground truth data of the crop and its multiple levels of damage are necessary. Two FAW field campaigns of about two weeks took place in 2018 and 2019 in the districts of Makoni and Chipinge. In April 2019, after the Cyclone Idai hit, a third field campaign took place in Chipinge. This district was badly affected by the floods and heavy winds and therefore it has been decided to collect samples of the different classes of damage. Data collection was made possible with the help of CIMMYT and their local partner, GOAL, who achieved the three field campaigns and helped us with transport, access to the sites, local authorities' authorizations, contact with farmers and access to their fields.

In a second step, satellite images of the area must be acquired as close as possible to the dates of the field campaigns, depending on their cloud cover content.

### 1. *Ground dataset*

#### a) FAW 2018 ground truthing

The 2018 FAW field data collection was conducted by CIMMYT with the primary goal of understanding the factors influencing FAW damage in African smallholder maize fields and quantifying its impact on yield (Baudron et al., 2019). The availability of this georeferenced FAW damage assessment data was an opportunity to evaluate the ability of remote sensing to detect such damage.

In total, 394 farming households were surveyed between the 2<sup>nd</sup> and 7<sup>th</sup> of February 2018 in Chipinge with approximately one third of this sample in each of the three Wards mentioned above. The same was implemented in Makoni between the 22<sup>nd</sup> and the 28<sup>th</sup> of March 2018 with a total of 397 households. In each of them, the head of the household was interviewed to gather information about the main maize field and this one was scouted for FAW afterwards. Each Ward was assessed by a team of four trained enumerators. The interview started with a standardized questionnaire in order to gather information about the main maize plot such as its size, the soil type, the presence or absence of a hedgerow, the previous crop and the number and dates of tillage, weeding operations and pesticides/herbicides/fertilizer applications. Then characteristics of the maize state were noted such as the maize growth stage estimated using the V notation, the maize variety and intercropped species if applicable.

Data were collected with Galaxy Tab A and Galaxy J5. The application CommCare was used to fill the questionnaire and GPS coordinates were automatically saved with an average location accuracy of 8.9 m.

The maize plot was then scouted using a 'W' pattern. Five-sampling points of 10 plants located on the same row were selected and assessed. The number of plants with leaf damage caused by FAW as well as plants with frass in the whorl were recorded at each sampling point.

The extent of the leaf damage was evaluated using the Davis scale from 1 to 9 and the score was given to each sampling point (Davis et al., 1992).

#### b) FAW 2019 ground truthing

The second FAW field campaign took place in the same Wards of Chipinge from the 18<sup>th</sup> to the 22<sup>nd</sup> of February 2019 and in Makoni from the 26<sup>th</sup> of February to the 1<sup>st</sup> of March. CIMMYT and GOAL organized this year's campaign with the same purpose of understanding the factors influencing FAW damage in African smallholder maize fields and quantifying its impact on yield. The exact same method as the previous campaign was used to assess 278 fields in Chipinge and 360 fields in Makoni. There was,

however, a slight change in the protocol to ensure that this year's GPS points were taken in the centre of the evaluated fields and not on the road or in the farmer's house as it was the case during the previous year. This campaign being this time directly linked to this study in remote sensing.

Beside the campaign run by GOAL, we went through each ward to visualize the physical context in which the fields were located. Various situations could be observed, georeferenced with a Garmin Etrex-10 and photographed in order to carry out a photointerpretation analysis on the satellite images available at the nearest dates. Furthermore, georeferenced points of non-maize features such as other crops, tree cover, grass, shrublands and bare soils were randomly taken in the area of study.

c) Cyclone Idai ground truthing

While not initially planned and in response to the cyclone crisis, this survey aims to assess the damage and possibly the crop biomass loss due to the cyclone. The data collection took place from the 1st to the 5th of April 2019 in Wards 16, 18 and 20 of Chipinge. Maize and sorghum fields were assessed since these are the main staple food of the region. Two measures of damage were reported from 434 maize fields and 251 sorghum fields, namely the percentage within a field of damage crops due to wind and the percentage of flooded crops. Two additional data were identified for each field and that are the crop biomass per field and the weed biomass. This campaign was made possible by CIMMYT and GOAL who trained the enumerators that collected the data and provided all the needed resources such as the Galaxy Tab A and Galaxy J5.

## 2. *Sentinel-2 images*

The Sentinel 2 mission is composed of two satellites, Sentinel 2A launched in 2015 and Sentinel 2B launched in March 2017. They are at a 180° angle of each other on the same orbit. Together, they have a 5 days revisit time since July 2017. The world imagery data is divided into tiles of 100 by 100 km and are projected in UTM/WGS84.

The three Wards of Makoni are entirely covered by the tile KUE and the tile KVC covers those of Chipinge.

The Sentinel-2 L1C (top of atmosphere) images for the 2017-2018 season were downloaded from the Sen2agri system which was released by UCLouvain in 2017 and funded by ESA. Four largely cloud-free images covering Chipinge were available on the following dates and were selected for further analysis:

- 24/01/2018, 3.07% cloud cover.
- 15/03/2018, 0.61% cloud cover.
- 20/03/2018, 0.00% cloud cover.
- 19/04/2018, 0.01% cloud cover.

As Makoni is concerned, the availability of cloud-free images is scarcer. The preliminary analysis on the 2017-2018 field campaign therefore focuses on Chipinge.

The images for the 2018-2019 season were directly downloaded from the Copernicus Open Access Hub made available by ESA. A view of the scenes available throughout de cropping season is displayed in appendix 2. Six largely cloud-free images are available over Chipinge for the period of interest as follows:

- 31/10/18, 0.00% cloud cover;
- 20/11/18, 0.05% cloud cover;
- 20/12/18, 1.16% cloud cover;
- 24/01/19, 8.44 % cloud cover;
- 28/02/19, 0.00% cloud cover (Figure 13);
- 25/03/19, 0.00% cloud cover.

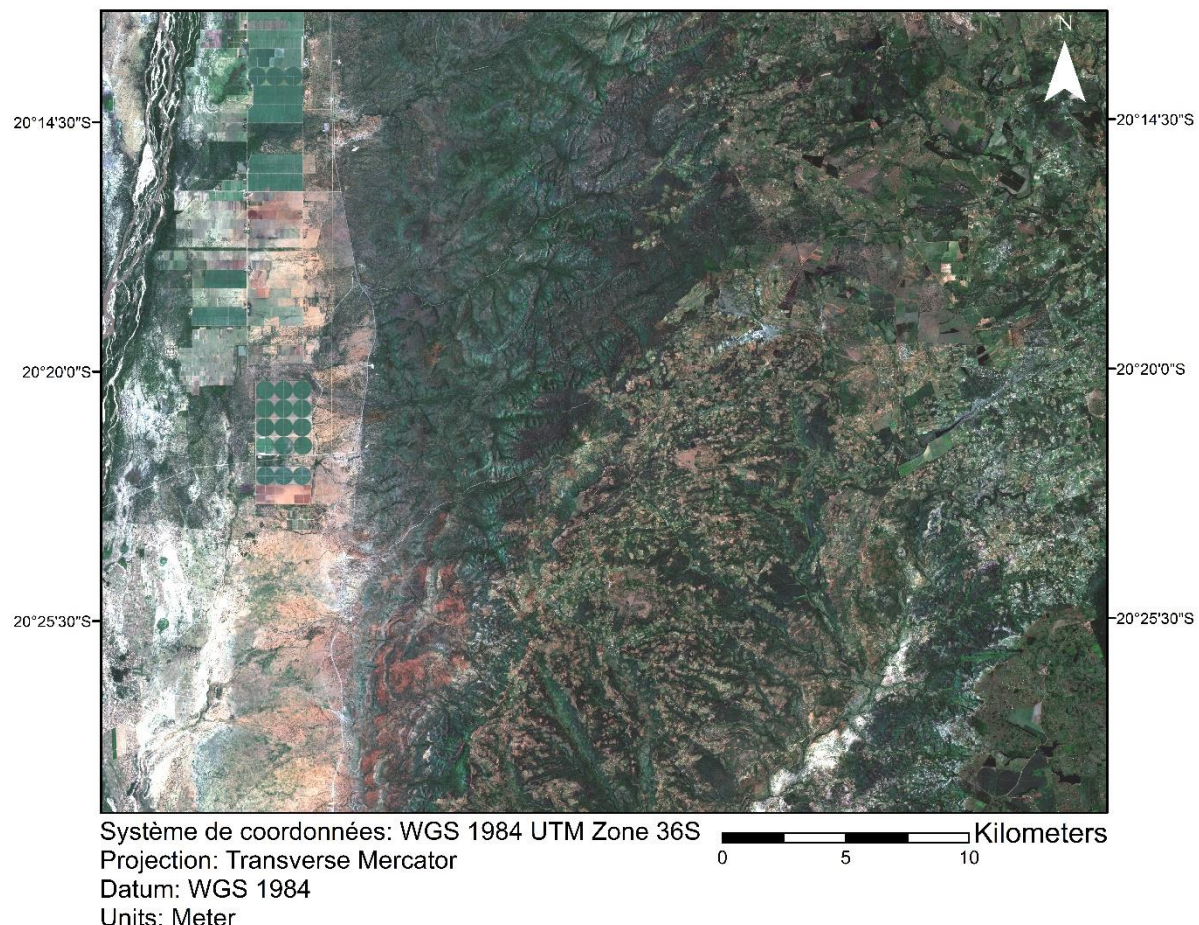


*Figure 13: Sentinel-2 true-colour image of the 28th of February 2019 over the three study Wards of Chipinge (from left to right, Ward 20, 16 and 18).*

The six largely cloud-free images for Makoni are available on these following dates:

- 29/10/18, 0.07% cloud cover;
- 13/11/18, 0.00% cloud cover;
- 01/02/19, 8.45% cloud cover;
- 21/02/19, 1.09% cloud cover;
- 03/03/19, 1.66% cloud cover;
- 27/04/19, 0.00% cloud cover.

### 3. Pléiades Images

Pléiades satellite system is a very high spatial resolution imagery that is able to provide scenes of any point of the globe within 24 hours and can have a daily revisit. Indeed, the two satellites Pléiades 1A and 1B launched in 2011 and 2012 are on the same orbit at 90° angle of each other. The two satellites have an optic instrument on board called the High-Resolution Imager (HiRI) that has a panchromatic band (0.47-0.94 µm) at 50 cm ground spatial resolution and four multispectral bands at 2 m ground spatial resolution. These four bands are the blue (0.43-0.55 µm), green (0.50-0.66 µm), red (0.59-0.71 µm) and NIR (0.74-0.94 µm). The Pléiades constellation is of a commercial type mainly for civil and military purposes. The image provider performs orthorectification to assure the geometric accuracy.

All the Pléiades images used for this research were specifically requested over the study area. Three acquisitions were planned in advance in order to cover the maize growing cycle. One was ordered in December, soon after the planting date. Another was planned in February to match the field campaign and the last one was acquired in late March, before the senescence of the plants. Three Wards in total were covered by Pléiades images namely Ward 16 in Chipinge and Ward 26 and 34 in Makoni. It was not intended to cover the other Wards since, initially, UAV imagery was planned over the sites of study. The country being in a climate of tension at the time, authorizations could not be obtained for this year season. The cloud free Pléiades images that cover Makoni were obtained at these following dates:

- Ward 26: 24/12/18 – 21/02/19 – 29/03/19
- Ward 34: 28/12/18 – 24/02/19 – 28/03/19

Those that cover Chipinge were acquired on these dates:

- Ward 16: 28/12/19 – 12/02/19 – 29/03/19 (Figure 14)

Soon after Cyclone Idai hit, two additional images were ordered over the two other Wards of Chipinge:

- Ward 18: 25/03/19 (Figure 14)
- Ward 20: 29/03/19

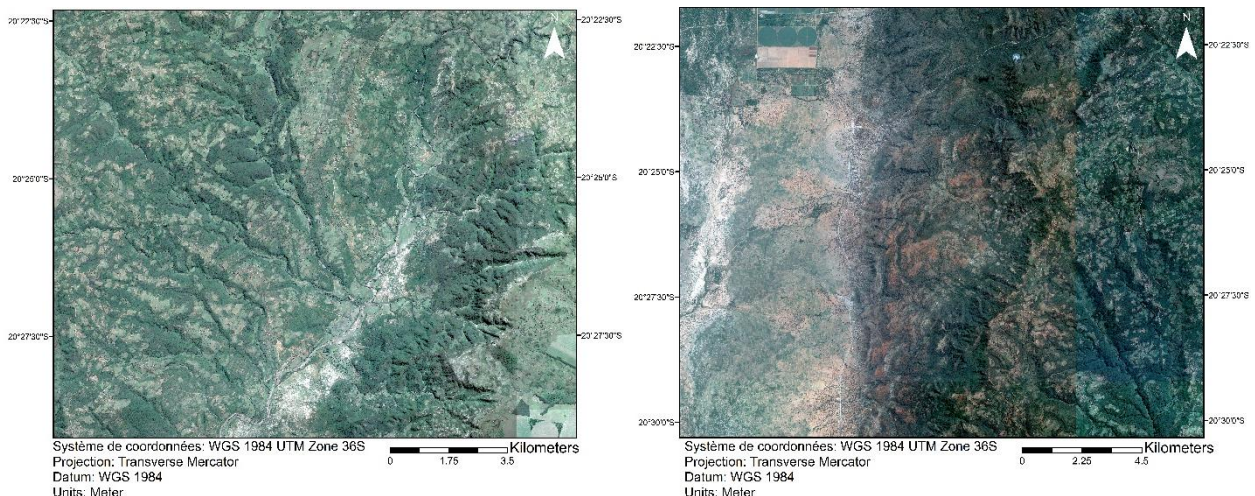


*Figure 14: Pléiades true-colours images acquired on the 25th of March 2019 over Ward 18 of Chipinge (left) and on the 29th of March 2019 over Ward 16 of Chipinge (right).*

#### **4. Software**

ArcMap 10.5.1 and ArcScene 10.5.1 from the Esri Arcgis suite were used to visualize the data and produce maps.

QGIS software was used to load the georeferenced data and create the shapefiles of the training and validation samples.

Sen2-Agri software, which was released by UCLouvain in 2017 and funded by ESA, was used to download part of the Sentinel-2 L1C images made available by ESA and pre-processed those images to produce L2A products.

Orfeo ToolBox (OTB) open-source project is a software initiated by the French Space Agency (CNES) that contains a library of algorithms for remote sensing image processing. It was used to perform RF classifications and compute confusion matrices.

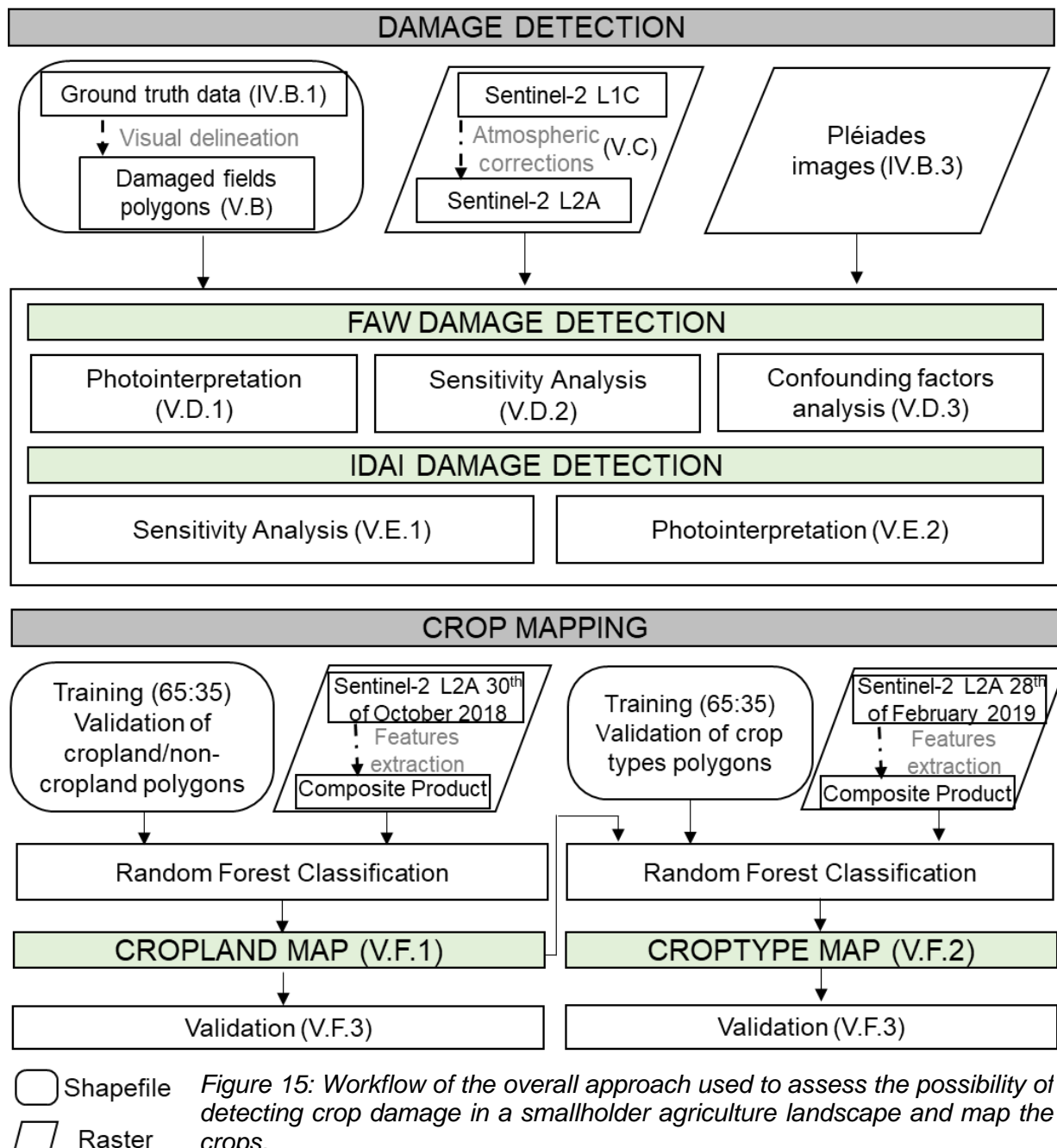
R-studio was used to develop R-scripts that operated the different image operations (cloud masking, features computation and extraction) and analyses. Several R packages were used for this master thesis:

- Raster
- Rgdal
- Rgeos
- Ggplot2

## V. Methods for Damage Detection and Crop Mapping

### A. Overall Approach

This section summarizes the overall approach (Figure 15) used to assess Sentinel-2 potential to detect damage on crops in a smallholder agriculture landscape as well as produce a crop type map. Sentinel-2 potential in detecting FAW damage will be assessed through a visual photointerpretation, a sensitivity analysis of the spectral features candidates and an analysis of the influence of confounding factors on FAW damage signal. The detection of cyclone Idai damage on crops will be assessed through a sensitivity analysis and a photointerpretation. Finally, a crop type map will be produced in two steps. First, a binary cropland mask will be produced and will serve as input for the crop type classification. Further explanations can be found hereafter.



## B. *In Situ* Data Preparation

The fields from each campaign were based on a visual photointerpretation to determine the limits of each plot. The nearest available Sentinel-2 image to the dates of the campaigns were used as well as the very high resolution imagery of Google Earth and the acquired Pléiades images. A negative buffer of the size of one pixel was applied to the shapefile in order to avoid the edge-effects and also discard the fields that were too small.

### 1. *FAW 2018 Field Campaign*

Last year's data collection was initially not designed for spatial analysis. Therefore, the georeferenced point was taken when the enumerator was starting the interview with the head of the household and that was usually inside the house or on the road. From the 791 assessed fields, 83 were delineated in Chipinge (45 in Ward 18, 26 in Ward 16 and 12 in Ward 20) and 66 in Makoni (30 in Ward 34, 19 in Ward 26 and 17 in Ward 28).

### 2. *FAW 2019 Field Campaign*

A total of 195 plots were drawn in Chipinge (48 in Ward 16, 84 in Ward 18 and 63 in Ward 20) and 241 in Makoni (89 in Ward 26, 61 in Ward 28 and 91 in Ward 34). Additionally, 103 polygons of other land covers were delineated over the study area.

### 3. *Idai Field Campaign*

A total of 459 fields were plotted over Chipinge with 283 maize fields and 176 sorghum fields. Additional polygons were added by photointerpretation to characterize the other land covers (other crops, bare soil, grassland, shrubland, tree cover, water, urban and rocks).

## C. Image Pre-processing

In order to use the satellite images for further analysis, two pre-processing operations are needed. First the level-1C top of atmosphere images must be atmospherically corrected to obtain level-2A products. The clouds and shadows are then removed from each band and derived features.

The Sen2-Agri L2A processor was used to produce L2A images by applying the Multi-sensor Atmospheric Correction and Cloud Screening (MACCS) chain on the top of atmosphere images from the 2017-2018 season. This level 2A processor uses a time series to detect the clouds and shadows and estimate water vapour and aerosol optical thickness (AOT) in order to correct the atmospheric effects (Sen2-Agri Consortium, 2018). The processor also produces a cloud mask containing different levels of cloud intensity and cloud shadows which was applied to all the bands and features to discard the unnecessary pixels.

The Sen2-Agri system encountered some software issues to download the 2018-2019 images. Therefore, the images directly downloaded from the Copernicus Open Access Hub were pre-processed with the Sen2Cor algorithm to obtain the level-2A products. This processor uses the bands at 60 m resolution relative to aerosols, water vapour and cirrus to correct the other bands that could be affected by the atmosphere. The processor works with a PlanetDEM Digital Elevation Model (DEM) and the correction is based on a one date image. Within the output products (atmospherically corrected bands), a classification scene is produced. Among the classified elements, there are the pixels of shadows and three levels of probability of cloud presence. This raster was reclassified into a binary one and was used to mask the bands and features from the clouds and shadows.

#### D. Fall Armyworm Damage Detection

In order to assess the potential of Sentinel-2 in detecting FAW damage on maize, three experiments were performed and are explained hereafter.

##### 1. Photointerpretation

During the field survey in 2019, the plots impacted by FAW were found in a variety of different contexts: dried fields due to El-Nin  induced drought effects; fields in mixed cropping and that were not weeded; small fields surrounded by trees and hedges and heterogenous fields in terms of planting dates. Besides, the damage of FAW were rather patchy within a field. Therefore, this experiment aims to determine the possibility of detecting FAW damage on Sentinel 2 images through visual photointerpretation, despite the presence of these other factors.

To do this, photos were taken on the field during the survey, a Sentinel-2 image is available almost at the same time (28<sup>th</sup> of February for Chipinge and the 1<sup>st</sup> of February for Makoni) as well as Pleiades images that are used for photointerpretation with higher spatial resolution.

##### 2. Sensitivity Analysis

This experiment aims to evaluate the separability potential of classes of damage for a set of Sentinel-2 spectral bands and derived VIs. For this purpose, a signature analysis was achieved using four Sentinel 2 spectral bands at 10 m resolution and six ones at 20 m resolution (Table 1). First, the experiment was performed at the field scale. The mean surface reflectance value of two fields with opposite levels of damage (based on the Davis score) was used for comparison. Then the mean surface reflectance value for all the pixels contained in all the fields of each category of damage was compared as well.

This analysis was also performed with VIs that are a combination of the spectral bands. They are used to highlight the sensitivity to vegetation while minimizing the effect of other factors such as soil brightness, atmospheric effects and so on. Based on the literature, a total of twelve vegetation indices were chosen to evaluate their capacity

in detecting the levels of FAW damage (Table 2). Some were chosen for their proven efficacy in detecting defoliation damage (see section II.C.3). Additional VIs were added for their specificity: GCI was chosen for its potential in estimating green chlorophyll content across a wide range of plant species; LAI estimates foliage cover; NDWI is used to monitor water content in leaves; NDRE, CIRE, MSRRe were chosen for their red-edge composition and their potential of improving LAI estimation by 10% (Xie et al., 2018).

The 2019 data being hardly usable due to the particular weather conditions of this season, the 2018 dataset was used as input data. The analysis was performed on the two nearest dates to the data collection in Chipinge namely on the 24<sup>th</sup> of January and the 20<sup>th</sup> of March.

*Table 1: Sentinel-2 bands used in this study and their respective wavelengths*

<b>Sentinel-2 Bands (10 m)</b>	<b>Range [nm]</b>	<b>Sentinel-2 Bands (20 m)</b>	<b>Range [nm]</b>
Band 2 (Blue)	490 ± 10 nm	Band 5 (Red-Edge)	705 ± 7.5nm
Band 3 (Green)	560 ± 32.5 nm	Band 6 (Red-Edge)	740 ± 7.5 nm
Band 4 (Red)	665 ± 17.5 nm	Band 7 (Red-Edge)	783 ± 10nm
Band 8 (NIR)	842 ± 15 nm	Band 8a (Narrow-NIR)	865 ± 10 nm
		Band 11 (SWIR)	1610 ± 45nm
		Band 12 (SWIR)	2190 ± 90nm

### 3. Confounding Factors Analysis

The combination of smallholder agriculture and the weather conditions of the 2019 season creates a complex situation where the crop signal can be mixed with other factors. This experiment was therefore designed to evaluate the amplitude of the confounding factors signals on that of FAW damage. It aims to analyse the difference of trajectories based on VIs' responses between healthy maize fields and damaged fields that are in a context where confounding factors are disturbing the signal. Therefore, the trajectory of healthy maize fields and damaged ones that are surrounded by confounding factors was plotted between two dates. Since it was noted during the field survey that this year, FAW outbreaks occurred at least six weeks after the planting date (i.e. around the second week of December), the trajectories were analysed between the 24th of January 2019 (no FAW) and the 28th of February 2019 (FAW infestation) for fields in Chipinge and between the 1st of February 2019 (no FAW) and the 3rd of March 2019 (FAW infestation) for the fields in Makoni. Any images available after these were impacted by the Cyclone Idai. Four categories of fields were selected based on situations observed during the field survey:

- Healthy fields that stayed healthy and are clear from confounding factors
- Healthy fields that got infested and almost entirely didn't grow due to the drought
- Healthy fields that got infested and are full of weeds and intercrops
- Healthy fields that got infested but are rather small and not dense

Table 2: Indices used in this study for the detection of the damage on maize and sorghum

Index	Description	Formula	Reference
NDVI	Normalized Difference Vegetation Index	$(\rho_{NIR} - \rho_{Red}) / (\rho_{NIR} + \rho_{Red})$	(Rouse and Haas, 1974)
EVI	Enhanced Vegetation Index	$G * \frac{\rho_{NIR} - \rho_{Red}}{(\rho_{NIR} + C1 * \rho_{Red} - C2 * \rho_{Blue} + L)}$ $G = 2.5 ; C1 = 6 ; C2 = 7.5 ; L = 1$	(Huete et al., 2002)
GCI	Green Chlorophyll Index	$(\rho_{NIR} - \rho_{Green}) - 1$	(Gitelson et al., 2003)
GNDVI	Green Normalized Difference Vegetation Index	$(\rho_{NIR} - \rho_{Green}) / (\rho_{NIR} + \rho_{Green})$	(Gitelson and Merzlyak, 1998)
GSAVI	Green Soil Adjusted Vegetation Index	$1.5 * \left[ \frac{\rho_{NIR} - \rho_{Green}}{\rho_{NIR} + \rho_{Green} + 0.5} \right]$	(Sripada, R. et al., 2005)
LAI	Leaf Area Index	$(3.618 * EVI - 0.118)$	(Boegh, E., et al., 2002)
SAVI	Soil Adjusted Vegetation Index	$1.5 * \frac{\rho_{NIR} - \rho_{Red}}{\rho_{NIR} + \rho_{Red} + L}$ where $L = 0.5$	(Huete, 1988)
MSAVI <sub>2</sub>	Modified Soil Adjusted Vegetation Index	$\frac{\left[ 2 * \rho_{NIR} + 1 - \sqrt{(2 * \rho_{NIR} + 1)^2 - 8 * (\rho_{NIR} - \rho_{Red})} \right]}{2}$	(Qi et al., 1994)
NDWI	Normalized Difference Water Index	$\frac{(\rho_{NIR} - \rho_{Swir})}{(\rho_{NIR} + \rho_{Swir})} ; 1628 \text{ nm} \leq \rho_{Swir} \leq 1652 \text{ nm}$	(Gao, 1996)
NDRE	Red-edge Normalized Difference Red-Edge Index	$\frac{\rho_{NIR} - \rho_{Red}_{edge}}{\rho_{NIR} + \rho_{Red}_{edge}}$ $710 \leq \rho_{Red}_{Edge} \leq 750$	(Gitelson and Merzlyak, 1994)
CIRE	Chlorophyll Index Red-Edge	$\left( \frac{\rho_{NIR}}{\rho_{Red}_{Edge}} \right) - 1 ; 710 \leq \rho_{Red\_Edge} \leq 750$	(Gitelson, 2005)
MSR <sub>Re</sub>	Modified Simple Ratio Red-Edge	$\frac{\left[ \left( \frac{\rho_{NIR}}{\rho_{Red}_{Edge}} \right) - 1 \right]}{\sqrt{\frac{\rho_{NIR}}{\rho_{Red}_{Edge}} + 1}} ; 710 \leq \rho_{Red\_Edge} \leq 750$	(Wu et al., 2008)

## E. Cyclone Idai Damage Detection

The method to evaluate Sentinel-2 potential in detecting cyclone Idai damage on crop proceeds in two steps: (i) a sensitivity analysis of Sentinel-2 spectral bands and derived VIs, (ii) a photointerpretation of the features selected as best responsive to levels of flattened/flooded damage in the first step. Both experiments are described hereafter.

### 1. Sensitivity Analysis

A signature analysis of the levels of each type of damage (i.e. flattened and flooded) was performed based on the mean surface reflectance value for all the pixels contained in the fields of each category of damage. The response of VIs (Table 2) to the levels of damage was also analysed. Furthermore, given the cyclone induced effects, additional indices related to the detection of water and flood were tested. Four of them were chosen based on the literature and are reported in Table 3. A fifth one was computed by testing the first SWIR band in the NDFI2. The cloud-free image on the 25th of March 2019 over Chipinge was picked for this post cyclone damage analysis.

*Table 3: Water indices tested in this study for the detection of flooded damage on maize and sorghum.*

Index	Description	Formula	Reference
NDWI	Normalized Difference Water Index	$(Green - \rho_{NIR}) / (\rho_{Green} + \rho_{NIR})$	(McFeeters, 1996)
MNDWI	Modified NDWI	$\frac{\rho_{Green} - \rho_{Swir}}{\rho_{Green} + \rho_{Swir}} ; \rho_{Swir} = 1640 \text{ nm MODIS}$	(Xu, 2006)
NDPI	Normalized Difference pond index	$\frac{\rho_{Swir} - \rho_{Green}}{\rho_{Green} + \rho_{Swir}} ; \rho_{Swir} = 1640 \text{ nm MODIS}$	(Lacaux et al., 2007)
NDFI2	Normalized Difference Flood Index_2	$\frac{\rho_{Red} - \rho_{Swir}}{\rho_{Red} + \rho_{Swir}} ; \rho_{Swir} = 2130 \text{ nm MODIS}$	(Boschetti et al., 2014)

The features showing the best potential of discerning the levels of damaged were selected and their discrimination power was further investigated by analysing the distribution of the fields' mean reflectance for the different levels of damage in order to visualize the dispersion around the median.

An analysis of variance (ANOVA) was also performed to examine the sensitivities of the spectral feature candidates.

A sensitivity analysis was also performed for the combination of two features. Indeed, by putting together the least correlated ones, more information could describe the levels of damage. Therefore, based on the correlation matrix, the combinations of features with a correlation that is less than 0.5 were plotted and a visual interpretation was performed to evaluate the possibilities of detecting the levels of damage.

## 2. *Photointerpretation*

Results from the previous step indicate that flattened damage are harder to detect than flood ones (see section VI.B.1). This analysis therefore focuses on detecting flood damage. From the sensitivity analysis, the best subset of spectral features to detect flood damage was chosen and a visual assessment was performed by looking at undamaged fields randomly chosen in Ward 18 and severely impacted fields in Ward 16.

To go further, a global visualization of the area on the 28th of February and the 25th of March was performed with the aim of determining if it was possible to detect the water. Water spectral signature is characterized by a low reflectance surface compared to other landscape components. Besides, water absorbs strongly at wavelengths of 1400 and 1900 nm and the SWIR channel is known to be more stable than NIR over inland water surface (Li et al., 2013). Therefore, a comparison of the two dates SWIR channel ( $1610 \pm 45$  nm) was made.

## F. *Crop Mapping*

The overall approach to produce a maize/sorghum mask involves three steps: (i) generate a cropland mask, (ii) mapping crop type within the existing cropland mask, (iii) validate the generated maps and evaluate the classification performances.

Throughout this work, we wanted to test the possibility of mapping the damage due to Cyclone Idai only and that for two main reasons. First of all, the damage due to the cyclone are much more extended and less patchy than those of FAW. Secondly, there was an opportunity to perhaps quantify the crop loss over a larger area than the field campaign and thus provide a quick and direct information to GOAL. The crop mask was therefore produced with the 2019 dataset of Chipinge since some farmers usually rotate their fields from one year to another.

### 1. *Binary Cropland Classification*

A pixel-based, supervised RF classification was used to discriminate crops from other land covers over the tile covering Chipinge. The ground dataset from the Idai campaign was used for maize and sorghum fields as well as the dataset of other landcovers from the FAW 2019 field campaign and photointerpretation. Each land cover class was split randomly into training (65/35) and validation subsets. All classes relative to crops were made as one and the other landcover classes constituted the second class. The training sample is used to train the model that feeds the classifier and the validation sample is used to assess the classification performance. Over the

trials of classification, the shapefile was enhanced to capture the purest pixel of each class.

All 10 bands of Sentinel-2 were used (Table 2) and resampled to 10 m as well as three common VIs (NDVI, GCI and MSAVI2). GCI was chosen for its ability to estimate leaf chlorophyll content across a wide range of plant species. MSAVI2 was selected because it suppresses the effects of soil fraction in pixels and increases the dynamic range of the vegetation signal which can be useful over more arid areas. The cropland mask was produced on the 31st of October 2018 image when the vegetation is not grown yet and the distinction between the cropland and other landcovers that included vegetation can be made.

The classification was generated through RF available in the library OTB. The user-defined parameters were set as OTB default values namely 100 trees, a maximum depth of 25 and a minimum of 25 features used at each node.

## 2. *Crop Type Classification*

A first crop type mask was generated by using as input the cropland mask produced in the previous step and an image of the growing season namely on the 28<sup>th</sup> of February 2019. The *in situ* training dataset contained three classes that are maize, sorghum and other crops. The RF classifier was used with the parameters set as default as well.

Other crop type masks were generated directly by using as input both images from the 30<sup>th</sup> of October 2018 and the 28<sup>th</sup> of February 2019 and a training dataset containing stratified landcovers to each area/Ward. This experiment was made following the results of the cropland mask and in order to enhance this one by understanding the classes responsible for contamination.

Finally, crop type masks were generated using a Pléiades image as input over ward 18 (image from the 25h of March 2019). Although this is after the cyclone hit, according to GOAL and the data we have, ward 18 was the less impacted village from Chipinge District. Besides, one can suppose that at the end of March the vegetation was more grown up than it was in February (dried out) since there were several rainfalls in between and thus a stronger crop signal.

## 3. *Validation method*

The validation of the generated maps was performed by computing a confusion matrix between the classified pixels and reference validation pixels. Several performance metrics were used namely the user's accuracy (UA) and producer accuracy (PA), the overall accuracy and the F1 score. This last metric is derived from the UA and PA of a specific class. The UA, also called precision, is the ratio between the correctly classified pixels and all the predicted pixels of the class. The PA, also referred as recall, is the ratio between the correctly classified pixels and the reference pixels of the class. The F-score for a class is computed as follows:

$$Fscore = \frac{2 * Precision * Recall}{Precision + Recall}$$

A visual validation was also performed, especially for the areas that were not covered by validation samples.

## VI. Results and Discussion

### A. Fall Armyworm Damage Detection

#### 1. Photointerpretation

The experience and knowledge gained in the field forced us to first and foremost analyse the conditions in which the fields infested by FAW were located. The detection of FAW damage on maize fields in Zimbabwe using Sentinel-2 images encounters different challenges due to the landscape typology and multiple confounding factors. Those are either related to weather conditions, the practices used in smallholder's agriculture, the spatial extents of FAW's damage and of course, the size of the fields that is very small.

First, the 2018-2019 cropping season has suffered from below-average rains. This year's crop production is expected to be lower than usual. Food insecurity outcomes were forecasted in most parts of the country (Famine Early Warning System Network, n.d.). The arid areas are badly affected with a significant rate of wilted crops. In the drier ward of Chipinge (ward 16), most of the maize didn't grow. The few fields with grown maize plants are not dense and most of them are infested by FAW. The pest is particularly present in this arid area considering the favourable temperature for its development and mating. The lack of maize plants, which is FAW's first diet, led to affected plants of Sorghum. This cereal is indeed better resistant to drought and was therefore planted by the farmers in this ward.

On the Figure 16 and Figure 17, we can see a field where the maize was planted around the second week of December but didn't grow at all. We came across a bare soil with some weeds here and there.

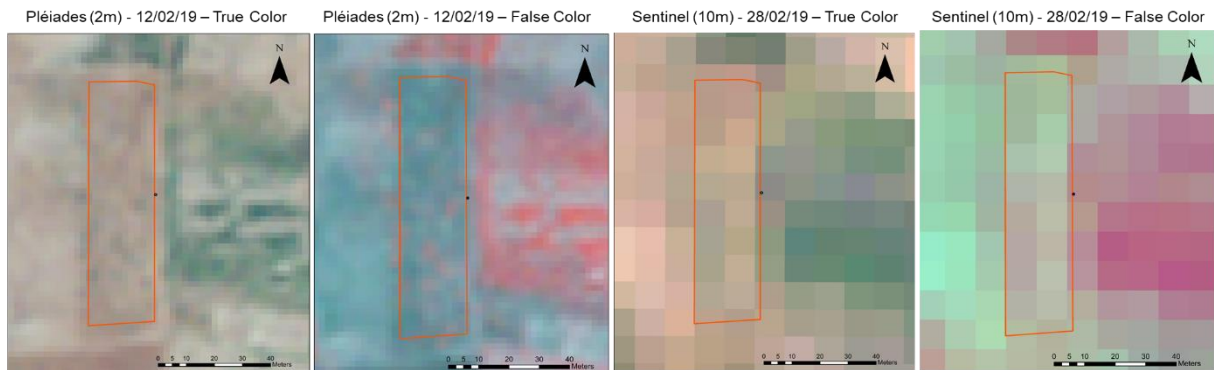


Figure 16: Illustration of a dried maize field in Ward 16 (Chipinge) ( $32.6575^{\circ}$ ;  $-20.4312^{\circ}$ ) on Pléiades (2 m) and Sentinel 2 (10 m) in true and false colours.



Figure 17: Picture taken on the 22nd of February 2019 of the field illustrated in Figure 16.

Another field in the same condition but in the southern part of Ward 16 is illustrated in Figure 18. We can see on the picture that only a few maize plants have grown. A few sunflowers plants were planted at the border of the field alongside the road.

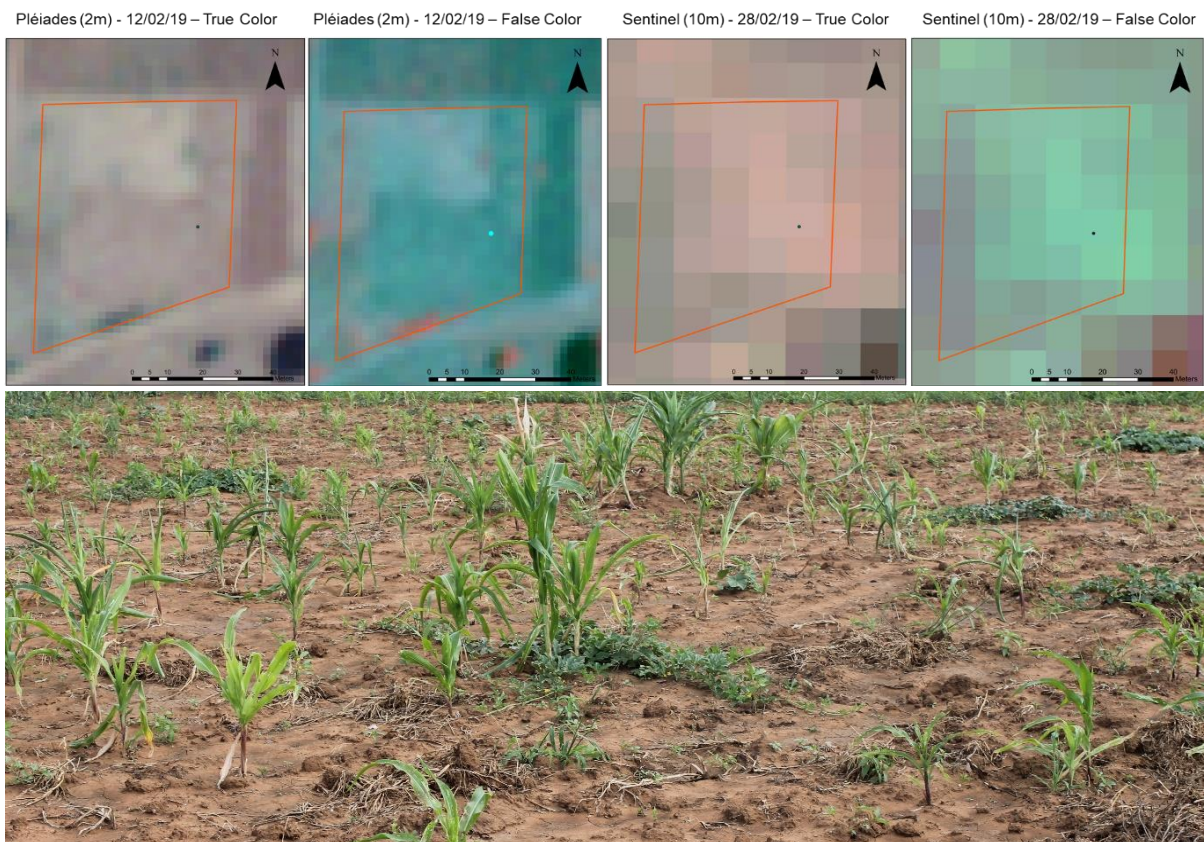
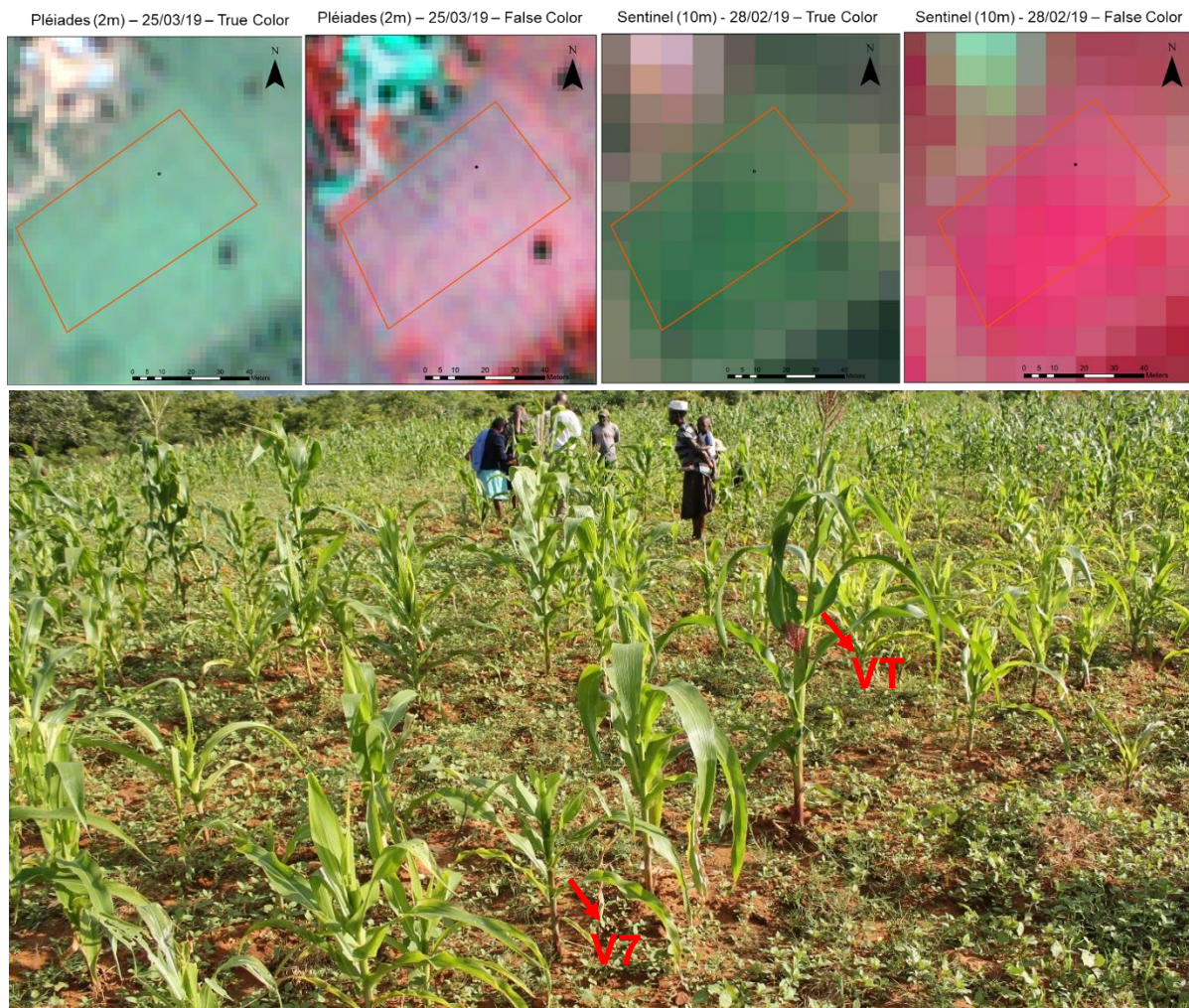


Figure 18: Illustration of a dried maize field in Ward 16 (Chipinge) ( $32.3658^{\circ}$ ;  $-20.4396^{\circ}$ ) on Pléiades (2 m) and Sentinel 2 (10 m) in true and false colours and a picture of that same field taken on the 22<sup>nd</sup> of February 2019.

The agricultural practices of smallholder farmers and their limited access to inputs and mechanization result in heterogeneous fields. Within the same plot (Figure 19), we can come across some maize plants still in the vegetative stages and others that are already tasselling. Also, farmers do not always weed their fields. Grasses are thus covering the ground which represents one important confounding factor for the detection of FAW's defoliation damage. Part of the farmers also plant mixed crops which will affect the signal as well.



*Figure 19: Illustration of a sparse and heterogeneous maize field in Ward 18 (Chipinge) ( $32.6079^{\circ}$ ;  $-20.3973^{\circ}$ ) on Pléiades (2 m) and Sentinel 2 (10 m) in true and false colours and a picture of that same field taken on the 19<sup>th</sup> of February 2019.*

Another field which is located in one of the highest parts of Ward 18 was already in the tasselling stage, starting senescence and the ground was covered with grasses and weeds (Figure 20).

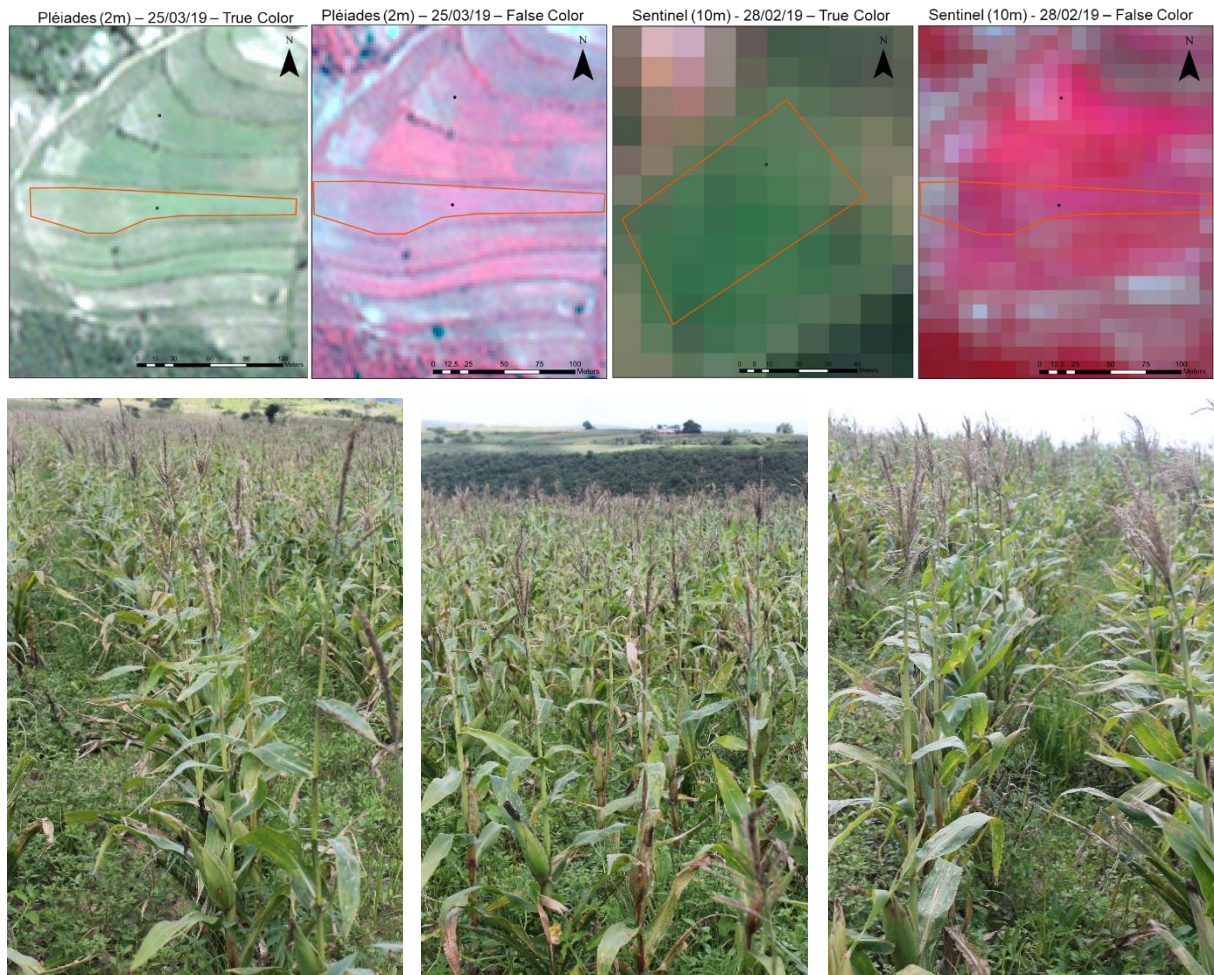


*Figure 20: Illustration of a weedy maize field already in the tasselling stage, in Ward 18 (Chipinge) ( $32.6479^{\circ}$ ;  $-20.4341^{\circ}$ ) on Pléiades (2 m) and Sentinel 2 (10 m) in true and false colours and a picture of that same field taken on the 21<sup>st</sup> of February 2019.*

Finally, the last noticeable constraint to detect FAW damage is the fact that those are very patchy within a field that is usually of a small size. From our knowledge acquired during our time in the field, it seems like rare that a plot is entirely destroyed. We came across fields in this condition but in the drier ward of Chipinge, where the maize plants were sparse, and the temperature was ideal for FAW.

On Figure 21, we can see a field that is located in Ward 18. Its size is quite representative of a good share of the fields in that area. We can see that when working with Sentinel 2, only two or three pixels are partially covering the field which leads to inherent edge effects. Moreover, the field was not dense and that it is the case for most of the fields in a smallholder agriculture context. FAW damage were patchy within

the field so that, even on Pléiades, the heterogenous pixels can be related to different factors and not necessarily to FAW damage.

The middle picture of Figure 21 shows the part of the field that was not impacted and the right side of the bottom picture shows a patch of damage in the field.

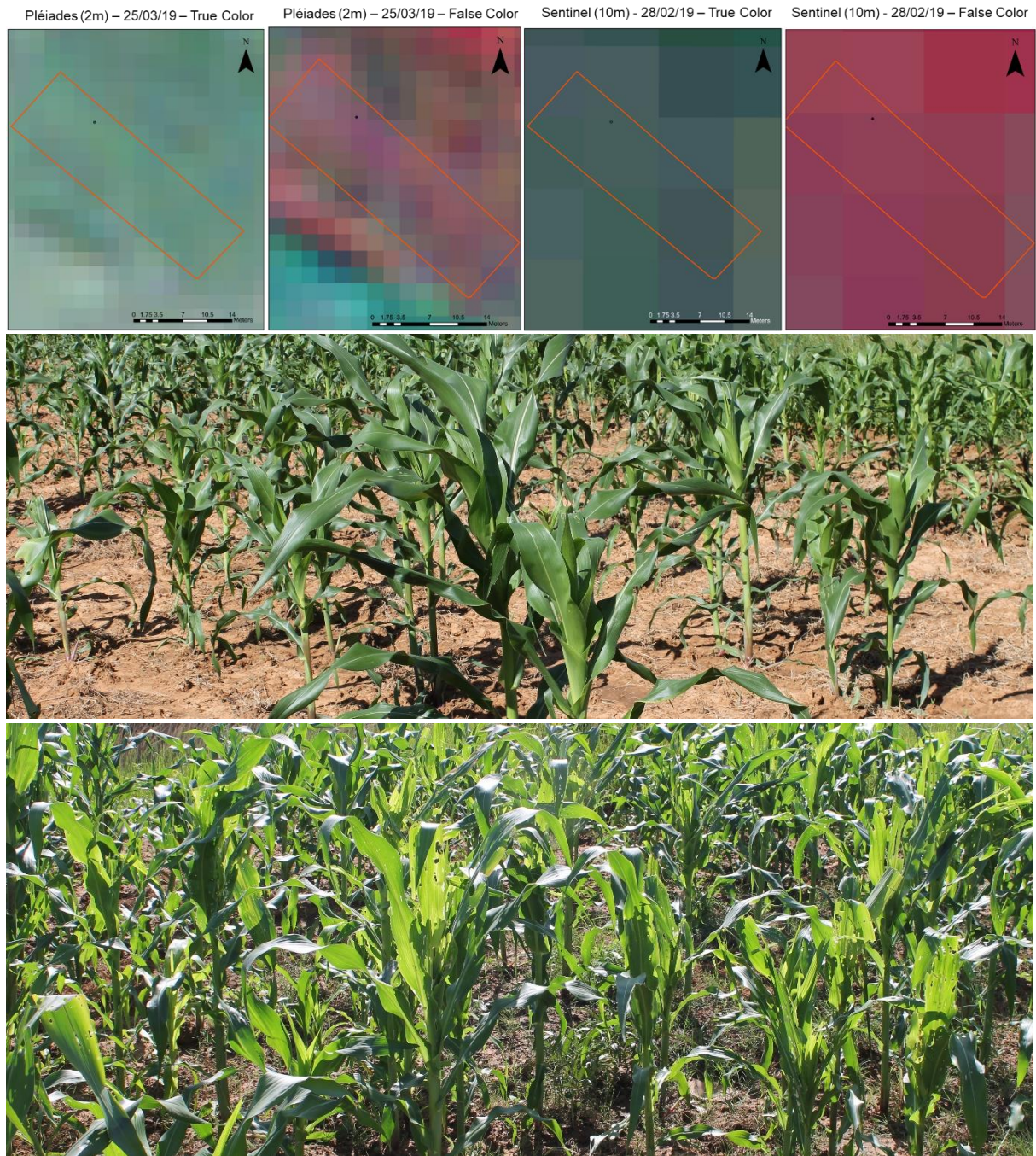


*Figure 21: Illustration of a maize field that is not dense, with patchy FAW damage in Ward 18 (Chipinge) ( $32.6026^{\circ}$ ;  $-20.3946^{\circ}$ ) on Pléiades (2 m) and Sentinel 2 (10 m) in true and false colours and pictures of that same field taken on the 19<sup>th</sup> of February 2019. The top picture is an undamaged part of the field and the bottom picture is of a damaged part.*

## 2. Sensitivity Analysis

The first sensitivity analysis involves two fields from Ward 18 that were selected based on the information collected through the campaign questionnaire. The fields were chosen for their similar context (no confounding factors) and opposed levels of damage. Both were weeded twice or more, had no intercrops and had a V stage of 6 in early February. The less damaged field has a Davis score of 3 and contains 6 pixels and the most impacted one has a Davis score of 7 and contains 9 pixels. On Figure 22 is represented the response of VIs and the spectral signature on the 20th of March 2018. The comparison could not be made on the 24th of January (available image closer to the field campaign) since one of the fields was under cloud cover.

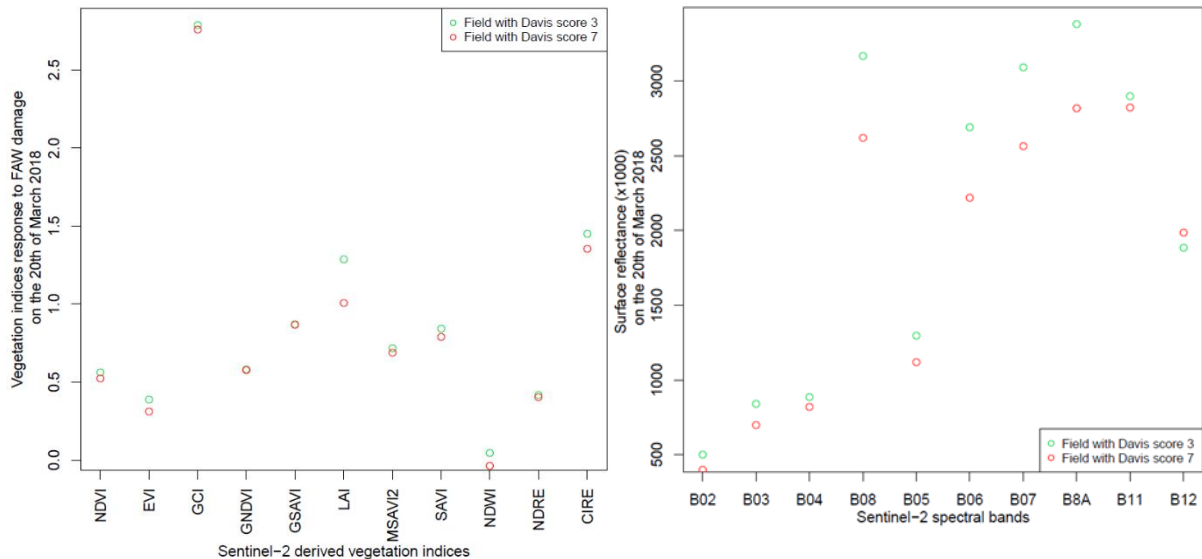


*Figure 22: VIs response (left) and surface reflectance of the ten original Sentinel-2 bands (right) on the 20<sup>th</sup> of March 2018. Two fields with distinct level of FAW damage (Davis score 3 and 7) and similar context are compared.*

When comparing the response of the VIs, it appears that there is a signal for NDVI, EVI, LAI, SAVI, NDWI and CIRE but the signal is weak. Indeed, the difference of value between the two fields is of 0.037, 0.077, 0.278, 0.057, 0.081 and 0.096 respectively for the cited VIs. The spectral signature shows coherent surface reflectance for band 3 (Green), band 8 (NIR), band 8A (narrow-NIR) and B12 (SWIR). Indeed, the green reflectance relates to chlorophyll pigment in the plant thus healthy vegetation corresponds to higher reflectance value. Similarly, the reflectance in the NIR is higher for healthy maize plants since it relates to the structural properties of the leaves. SWIR bands are known to be sensitive to water content. Thus, a healthy plant with higher water content will have a lower reflectance value. Nevertheless, an odd response is observed for band 11. Also, the response in the blue and red bands are unexpected since the wavelengths in the blue and red are absorbed by the chlorophyll pigments and thus the reflectance for healthier plant should be lower. However, the reflectance values are very close between the two fields.

Another pair of very similar fields contrasted with regards to damage can be studied even though no or only one operation of weeding took place. These fields, a healthy one in Ward 20 and a damaged one in Ward 18, are compared on Figure 23. Both had no intercrop, had one or fewer weeding operations and a V stage of 6 in early February. The VIs response and the surface reflectance value of the ten bands of Sentinel-2 are from the 24<sup>th</sup> of January 2019.

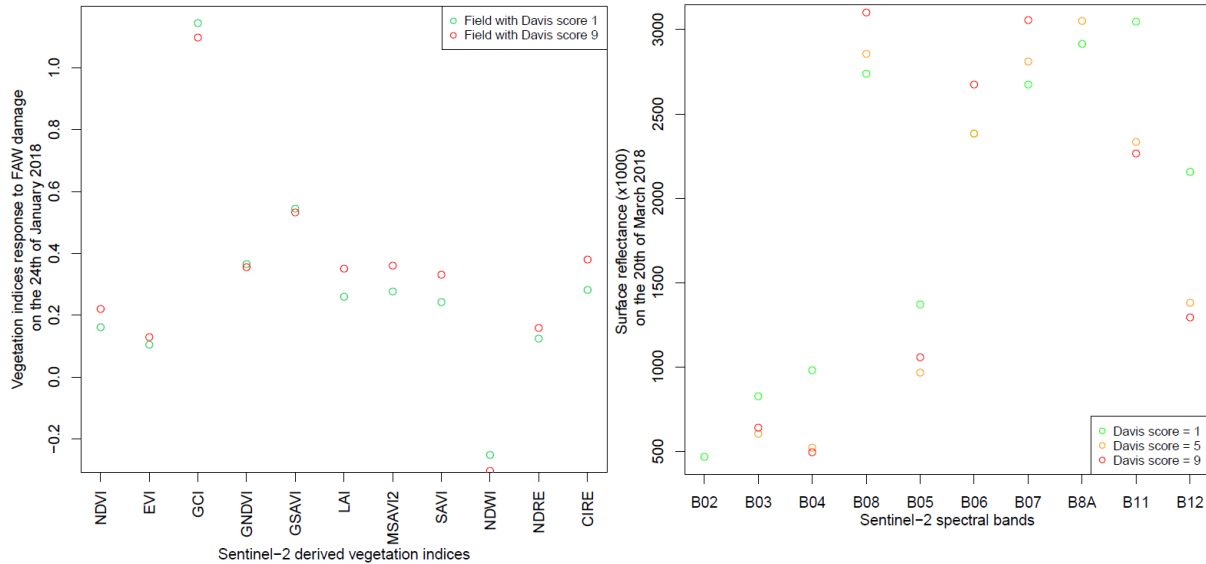


*Figure 23: VIs response (left) and surface reflectance of the ten original Sentinel-2 bands (right) on the 24<sup>th</sup> of January 2018. Two fields with distinct level of FAW damage (Davis score 1 and 9) and similar context are compared.*

Except from the GCI that appears to respond to the level of damage, the other VIs do not suggest that there is a signal sensitive to FAW damage. As the signature analysis is concerned, band 3 (Green) and band 8 (NIR) show surface reflectance values that are consistent with the expected outcome while the other bands' signal seems to fail to detect FAW damage. The potential FAW signal is probably masked by the grasses or weeds density variability.

Finally, the mean VIs/reflectance value for all the pixels contained in three categories of damage (Davis score 1, 5, and 9) is shown on Figure 24. When comparing the VIs response, there is apparently a slight signal for the mean value for the damage score of 5 and the one of 9. The signal seems yet not easily perceptible with a maximum difference of 0.16 for CIRE. The significance of this result should be statistically tested by taking into account the whole distribution of the fields classes. Nevertheless, the mean value of the healthy plants is systematically lower than the mean value of the damaged ones which is really unexpected. The signature analysis shows that the signal amplitude appears weak in the visible with a small surface reflectance range. The NIR, narrow-NIR and SWIR bands seems to fail to respond to FAW damage.

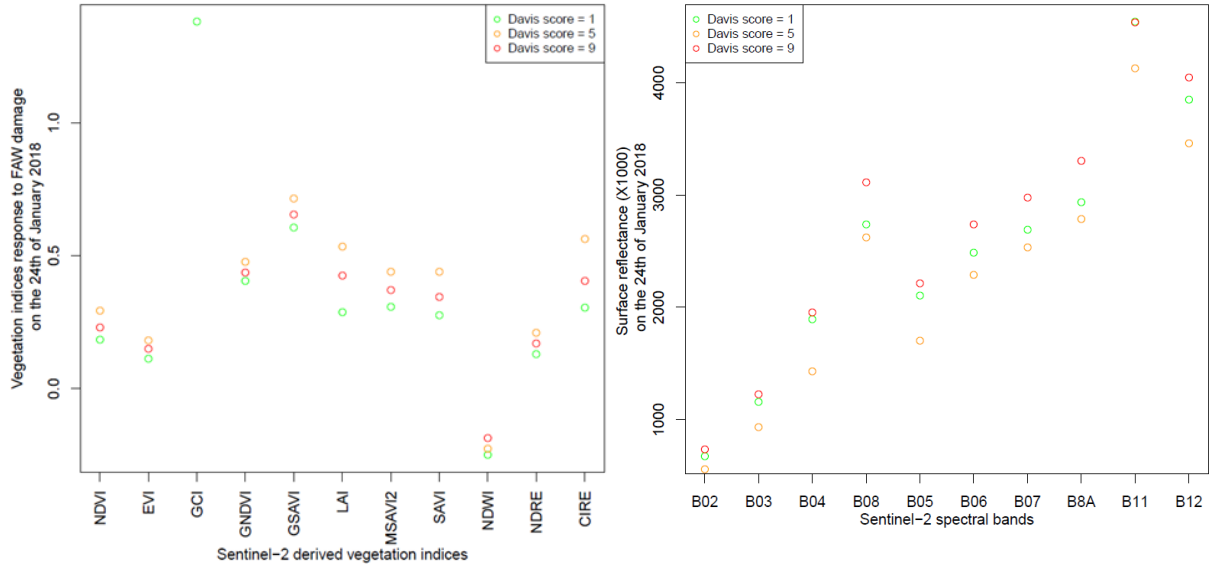


**Figure 24:** VIs response (left) and surface reflectance values of the ten original Sentinel-2 bands (right) to three levels of FAW damage (Davis score 1, 5 and 9) on the 24th of January 2018. The mean value of all the pixels in each category is considered.

The results shown for the sensitivity analysis must now be discussed.

The two similar fields with no confounding factors and contrasted damage compared in the first analysis show promising results for some VIs and Sentinel-2 bands. However, the range is quite small, and the surface reflectance is very low in the visible. Besides, the blue and red bands have unexpected values. This can be discussed and related to the corrections that L1C image of March 20 had. Indeed, MACCS chain corrected atmospheric effects, adjacency effects and slope effects to produce the level-2A image. The bands in the visible (blue and red) are particularly sensitive to the atmosphere. To correct its effects, an aerosol optical thickness layer (AOT) is produced through multi-temporal and multispectral analysis of the top of atmosphere value (Hagolle et al., 2015). The two fields being distant from each other and different in terms of correction target (i.e. the healthy field is considered as vegetation while the damaged one could be considered as soil due to the defoliation damage) they might have been both subject to different AOT corrections. A slight difference in AOT correction for a signal that is already very low could easily reverse the resulting reflectance value.

The mean pixel reflectance value for each category of damage must also be put in perspectives and discussed with the context of the fields based on the additional information collected through the campaign questionnaire. Indeed, we can note that, on the one hand, the fields that are the most damaged were only weeded once or not at all and one was intercropped with pumpkins. Moreover, the maize plants of those fields were at a V stage of 6-7 and belong to Ward 18 thus normally receiving more rainfalls. On the other hand, none of the healthy fields were intercropped and some were weeded twice or more. The average V stage of the maize was 3 and those fields

were located in Ward 16 and 20 where the rainfalls are scarcer, and the area is more arid. It is also important to say that the sample of fields for last year season was quite small. After the negative buffer, 57 fields were left over Chipinge and some were under cloud cover on the 24<sup>th</sup> of January. Only two fields were representative of a Davis score of 9 and nine of a Davis score of 1. That being said, we can assume that the signal of the fields with a damage score of 9 was mostly related to green vegetation of weeds, intercrops and bigger maize plants. This could explain the higher reflectance in the NIR and higher VIs responses. Also, the mid-category of fields with a damage score of 5 seems closer in terms of physical context to the fields with score 9. Indeed, the V stage of the maize was of 5-6, many of the fields were not weeded or once, and one was intercropped with pulses. They were almost all located in Ward 18, only one was in ward 16 and one in ward 20. The results being put in perspective, one can suppose that confounding factors might disturb the signal since it is not clear what signal is actually captured.

### 3. Confounding factors analysis

This experiment was implemented on all VIs tested in this work. The trajectories of each category of damage being very similar for all VIs, the result of the confounding factors analysis for NDRE values is shown on Figure 25 and summarized in Table 4.

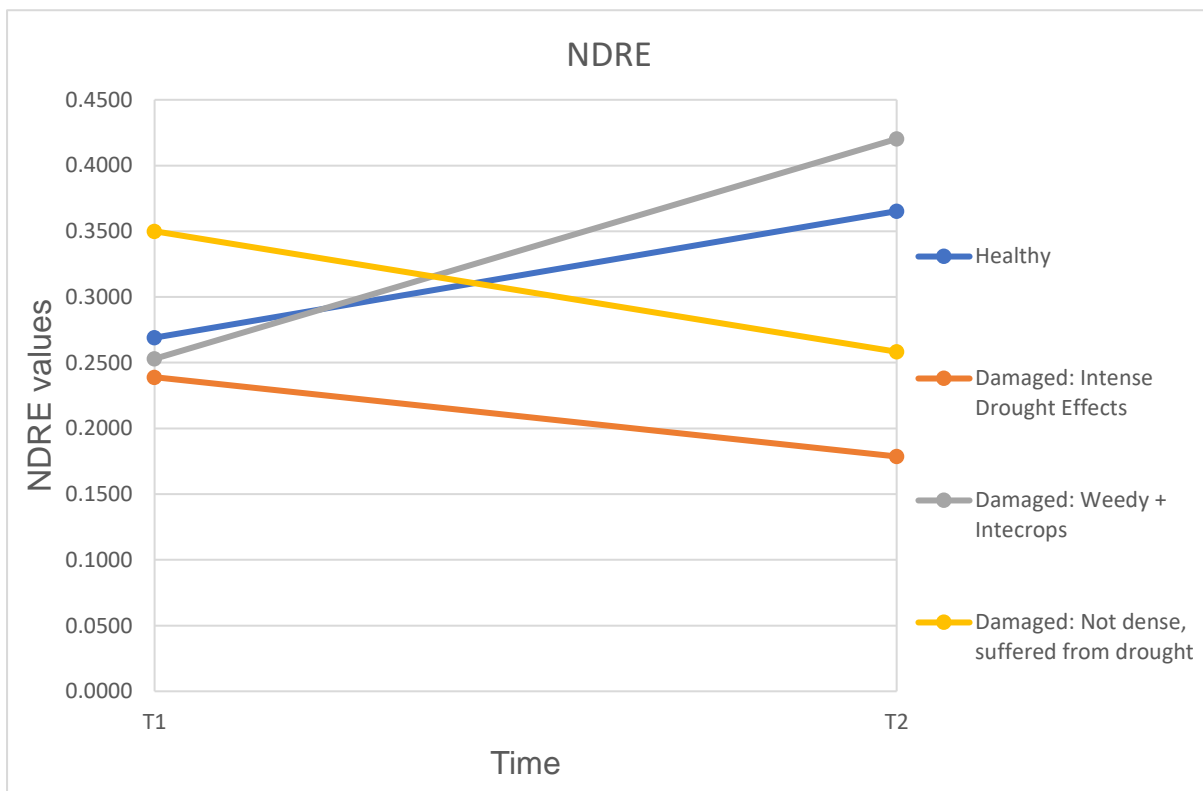


Figure 25: NDRE response between healthy maize fields and damaged fields that are in a context where confounding factors are disturbing the signal. The trajectories are analysed between the 24th of January 2019 and the 28th of February 2019 for fields in Chipinge and between the 1st of February 2019 and the 3rd of March 2019 for the fields in Makoni.

The NDRE was chosen because it depends on the band 5 in the red-edge and not the red band in the visible which makes it possible to overcome the problems of atmospheric corrections encountered in the sensitivity analysis. CIRE was left out due to a fairly large standard deviation.

The result shows that the signal amplitude of healthy fields that stayed healthy after FAW outbreak and are not surrounded by confounding factors is of 0.10. The difference of amplitude for fields that got damaged and suffered from intense drought effect at T2 is of -1.6. The fields that got damaged and were observed at T2 with weeds and/or intercrops have an amplitude difference of 0.58. Finally, the difference of amplitude is of -1.05 for fields that, at T2, were not dense and suffered from drought effects. The sensitivity analysis results showed that there is only a slight difference of NDRE value of 0.02 for fields with contrasted level of damage but no confounding factors (Figure 22). It seems therefore appropriate to say that the confounding factors are largely masking any FAW damage signal.

*Table 4: Mean values and standard deviation values for healthy fields and damaged fields that are in a context where confounding factors are disturbing the signal between the 24th of January 2019 and the 28th of February 2019 for fields in Chipinge and between the 1st of February 2019 and the 3rd of March 2019 for the fields in Makoni.*

NDRE	T1		T2			Signal amplitude difference with healthy fields
	Mean Value	Standard Deviation	Mean Value	Standard Deviation	Slope	
Healthy	0.27	0.03	0.37	0.05	0.10	1.00
Damaged: Intense drought effects	0.24	0.07	0.18	0.04	-0.06	-1.60
Damaged: Weedy + intercrops	0.25	0.11	0.42	0.03	0.17	0.58
Damaged: Not Dense, suffered from drought	0.35	0.08	0.26	0.07	-0.09	-1.05

## B. Cyclone Idai Damage Detection

### 1. Sensitivity Analysis

The mean VIs and water indices values for each category of maize/sorghum flood damage is shown on Figure 26.

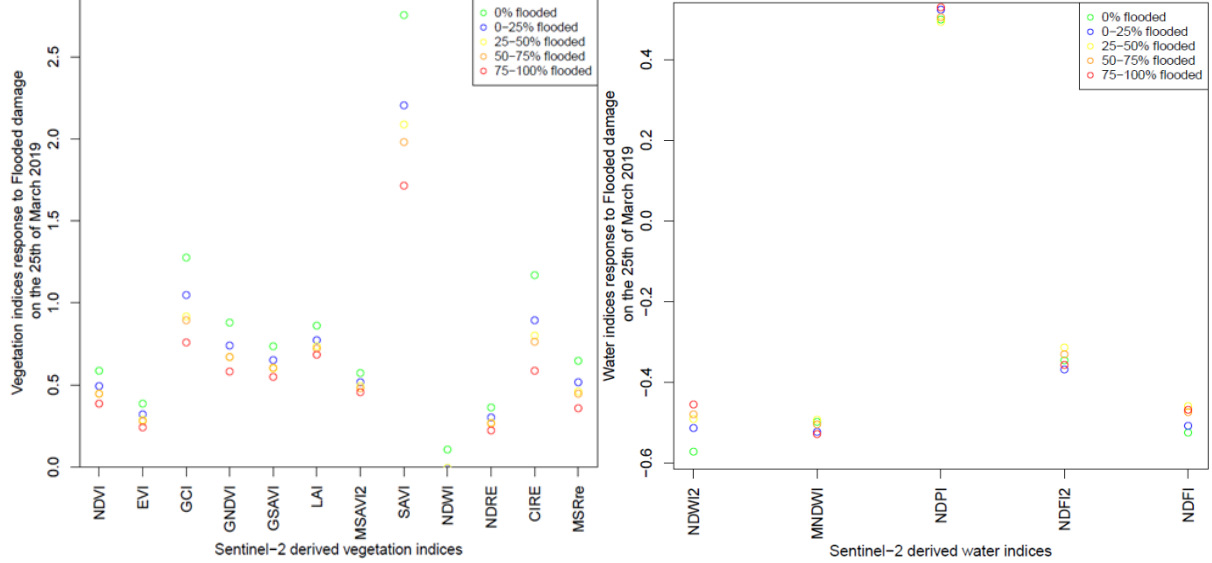


Figure 26: Mean VIs response (left) and mean water indices response (right) for each category of maize/sorghum flood damage on the 25<sup>th</sup> of March 2019.

When comparing the VIs response, there is a clear signal for SAVI which seems to discriminate the five levels of flood damage. Almost all the other VIs and particularly the GCI and CIRE also show a promising response to detect flood damage but with a lower level of the intermediate classes discrimination. As the water indices is concerned, the NDWI2 that is relative to water bodies has a clear signal to differentiate three classes of flood damage (i.e. the two extremes ones and the intermediate ones together). The other water indices signal is weak. The spectral signature analysis results are shown on Figure 27. Water having a lower surface reflectance value than vegetation (except in the blue), the most impacted fields should have the lowest value of the five categories. Coherent surface reflectance is observed for the less and most impacted fields in the blue band, the NIR/narrow-NIR and red-edge 6 and 7 bands. However, the reflectance values of the intermediate categories for the last four mentioned bands are unexpected. The other Sentinel-2 spectral bands do not seem to have a signal responsive to flood damage.

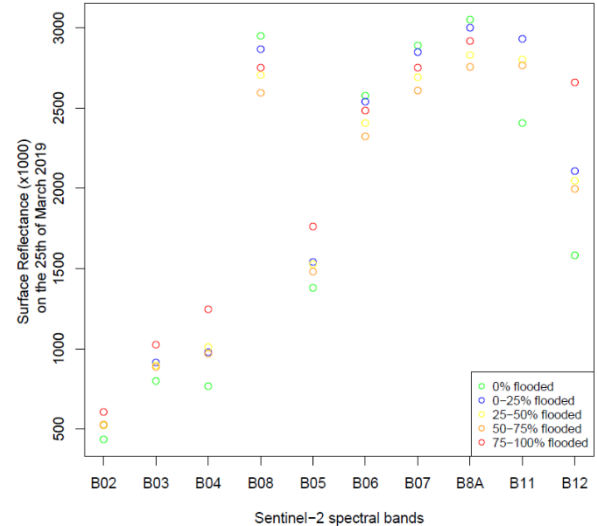
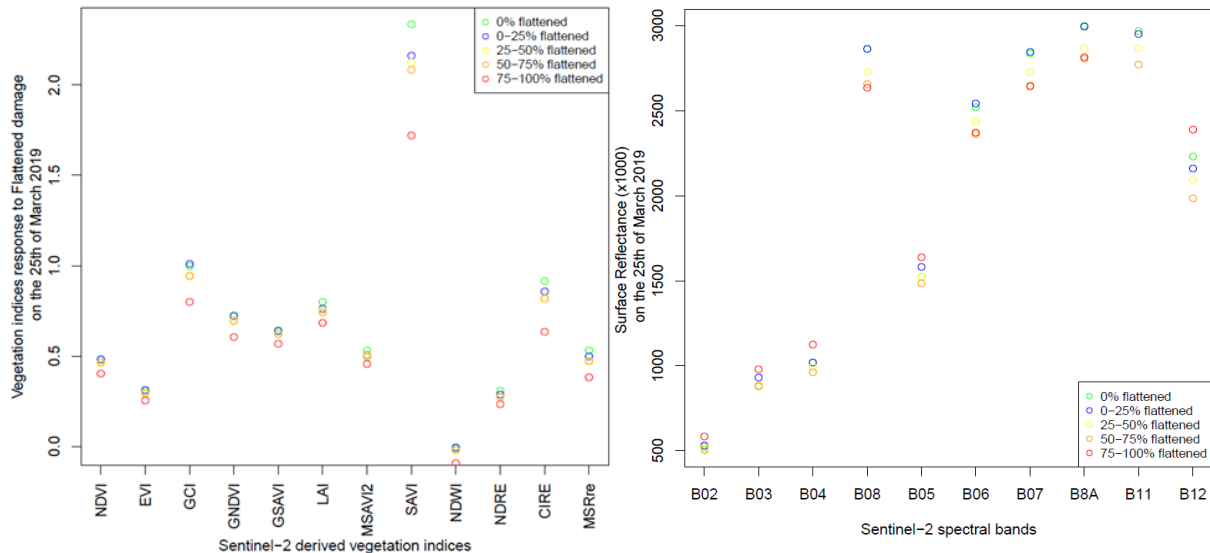


Figure 27: Mean surface reflectance values of the ten original Sentinel-2 bands for the five categories of flood damage on the 25<sup>th</sup> of March 2019

The fields were also impacted with flattened damage. The mean VIs and surface reflectance values for each category of maize/sorghum flattened damage is shown on Figure 28.



*Figure 28: Mean VIs response (left) and mean surface reflectance values of the ten original Sentinel-2 bands (right) for the five categories of flattened damage on the 25<sup>th</sup> of March 2019*

A first observation is that SAVI and CIRE seems both to have correlated response with the five levels of flattened damage although the signal for the intermediate classes seems weaker. These two VIs thus appear to have a signal to discriminate clearly three categories of flattened damage. The other VIs seem to have a slight signal for the extreme classes of damage. The spectral signature analysis shows that, in the visible and first red-edge band, the most impacted fields have a higher reflectance value than the spared ones. From the second red-edge band to the narrow-NIR band, the opposite is observed while in the second SWIR band, the most flattened fields have a higher mean surface reflectance value. On Figure 29 can be observed photos from the news illustrating flattened crop fields after cyclone Idai. It can be observed that in the concerned landscape, flattened crop fields seem to show a greater proportion of soil than vegetation. The class with the greater flattened damage has thus a signal that is influenced by the one of the soil. In the visible, the soil spectral signature is higher than healthy vegetation. In the red-edge and NIR part of the spectrum, the soil reflectance values get lower than vegetation. In the mid-infrared and SWIR, the soil spectral signature is higher than vegetation. Thus, it appears that there is a signal in the NIR/narrow-NIR and red-edge to distinguish three levels of flattened damage as well as a weaker signal in the visible.



*Figure 29: Pictures taken after Idai illustrating flattened crop fields in Chimanimani, Zimbabwe on the 17<sup>th</sup> of March 2019 (left, credits to Xinhua from “New China”) and Beira, Mozambique (right, credits to Thomson Reuters, nd.)*

To sum up, flood damage can be best distinguished by SAVI, GCI, CIRE, NDWI2 and the blue and NIR bands that seem the most responsive. Flattened damage can be best distinguished by SAVI, CIRE, band 6, 7 in the red-edge and 8, 8A in the NIR/narrow-NIR. Their potential is further investigated by analysing the distribution of the fields’ mean reflectance for the different levels of damage in order to visualize the dispersion around the median. The distributions of the features selected as best responsive to flood damage are shown on Figure 30.

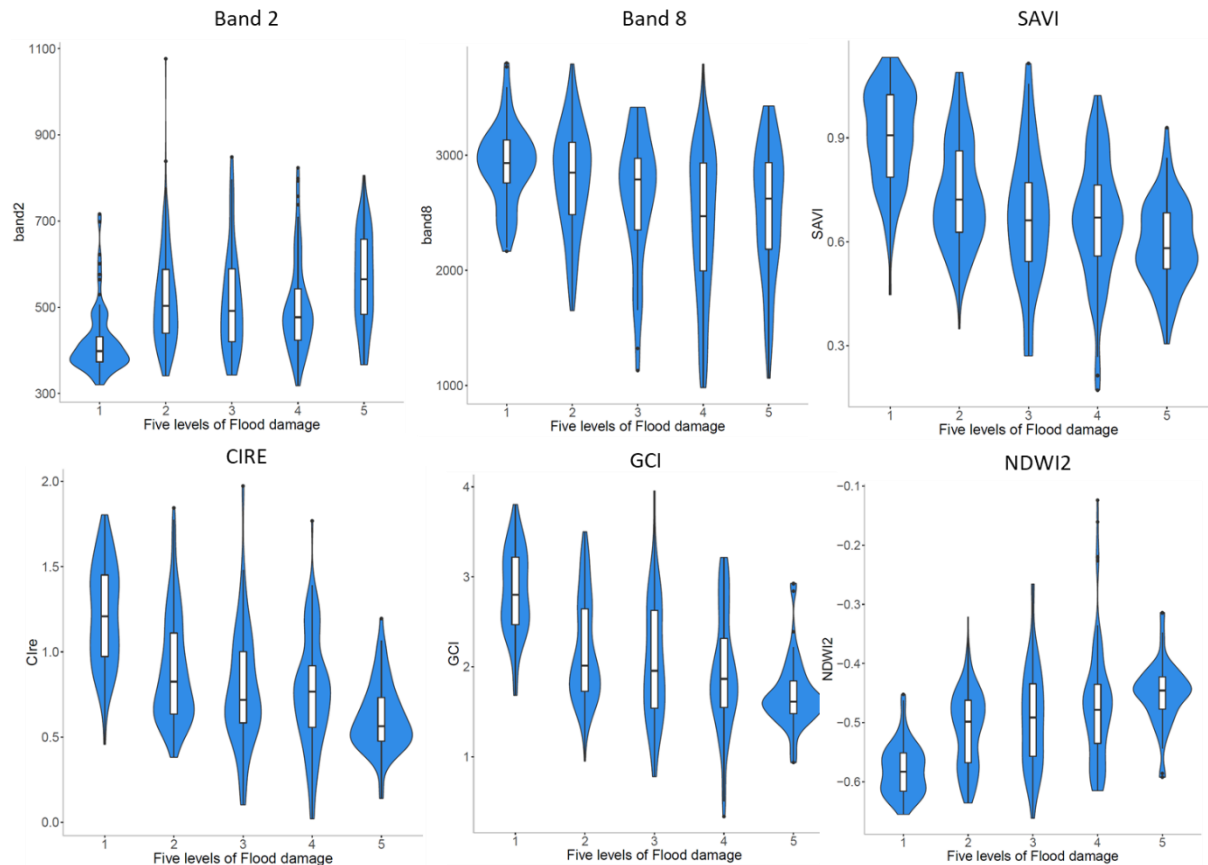


*Figure 30: Distribution of the bands/VIs response for each category of flood damage around the median. The graph is composed of a boxplot and a mirrored distribution of the data (blue).*

Within the white box can be found fifty percent of the data that are distributed around the median with the bottom line of the box, being the first quartile and the top line is the third quartile. The blue shape corresponds to the mirrored distribution of the data. This one helps to determine if the data are overlapping or not between the levels of damage and more precisely how many levels of damage could be distinguished. For the detection of flood damage, it would seem possible to distinguish the two extreme categories with the GCI, NDWI2 and perhaps the NIR, blue, CIRE and SAVI since 50% of the data and more are not overlapping at all. The three intermediate categories seem that they could be detected as one.

With respect to flattened damage, the results can be seen on Figure 31. For bands 6, 7, 8 and 8A, the white box of the unimpacted category (i.e. 50% of the fields) have a distinct higher reflectance values than the white box of the most impacted category. Distribution overlaps between the categories of flattened damage are, however, more pronounced than for flood damage.

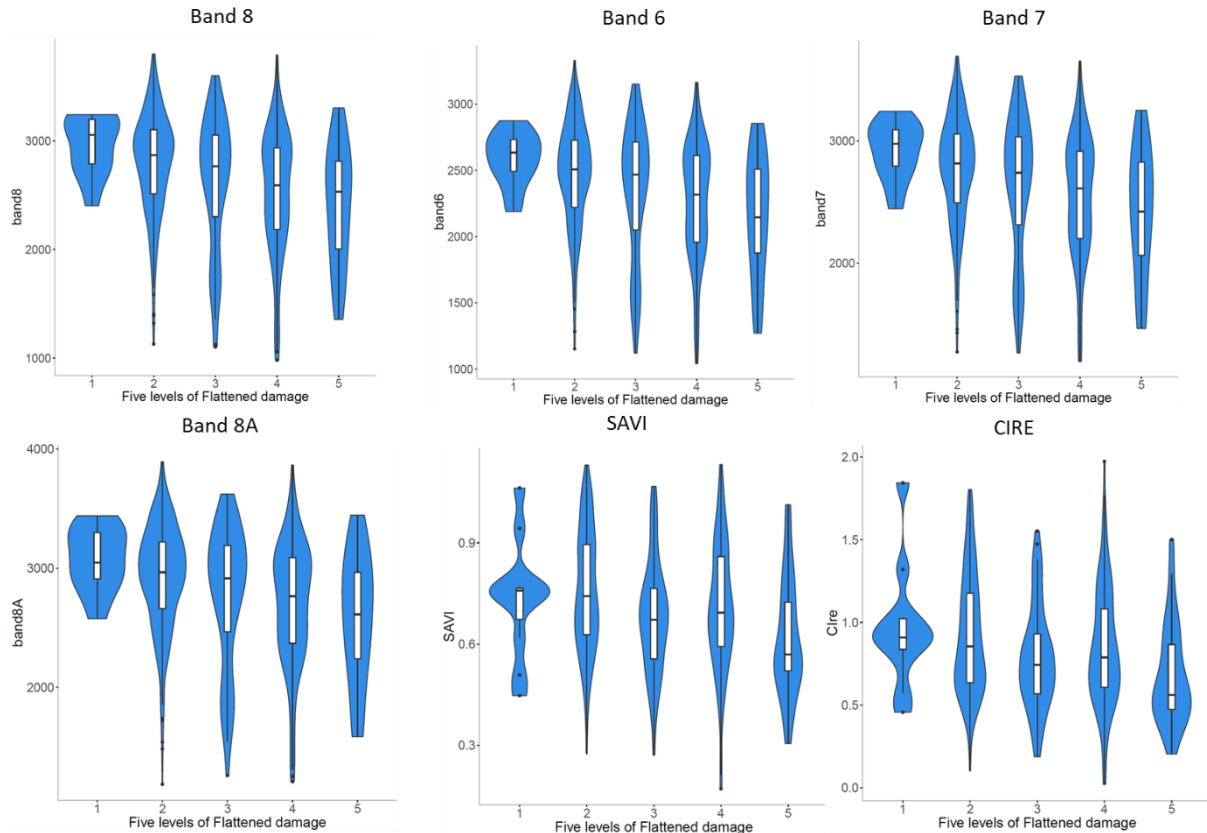


*Figure 31: Distribution of the bands/VIs response for each category of flattened damage around the median. The graph is composed of a boxplot and a mirrored distribution of the data (blue).*

An analysis of variance (ANOVA) was performed to test the significance of the differences in spectral features to explain the levels of damage. This analysis did not bring supplementary information since almost all the results were statistically significative.

Finally, we have looked at the information that a combination of two features could bring for those that were the less correlated. The results are shown in Table 5. The combination of features with a correlation that is less than 0.5 are highlighted in green. This threshold was arbitrarily chosen. The VIs being highly correlated with one another, the values are not represented in Table 5.

*Table 5: Correlation values between the spectral features tested in this study. The VIs being highly correlated, it is not summarized here. The combination of features with a correlation that is less than 0.5 are highlighted in green.*

	band2	band3	band4	band8	band5	band6	band7	band8A	band11	band12
band2	1.00	0.93	0.89	0.20	0.80	0.26	0.22	0.24	0.80	0.84
band3	0.93	1.00	0.88	0.50	0.93	0.55	0.51	0.53	0.87	0.87
band4	0.89	0.88	1.00	0.24	0.90	0.32	0.27	0.27	0.88	0.92
band8	0.20	0.50	0.24	1.00	0.59	0.98	0.99	0.99	0.52	0.41
band5	0.80	0.93	0.90	0.59	1.00	0.66	0.61	0.62	0.92	0.91
band6	0.26	0.55	0.32	0.98	0.66	1.00	1.00	0.99	0.57	0.47
band7	0.22	0.51	0.27	0.99	0.61	1.00	1.00	1.00	0.54	0.43
band8A	0.24	0.53	0.27	0.99	0.62	0.99	1.00	1.00	0.56	0.44
band11	0.80	0.87	0.88	0.52	0.92	0.57	0.54	0.56	1.00	0.98
band12	0.84	0.87	0.92	0.41	0.91	0.47	0.43	0.44	0.98	1.00
NDVI	-0.60	-0.37	-0.66	0.56	-0.31	0.47	0.51	0.51	-0.32	-0.45
EVI	-0.39	-0.12	-0.46	0.75	-0.07	0.67	0.71	0.71	-0.11	-0.25
LAI	-0.39	-0.12	-0.46	0.75	-0.07	0.67	0.71	0.71	-0.11	-0.25
SAVI	-0.60	-0.37	-0.66	0.56	-0.31	0.47	0.51	0.51	-0.32	-0.45
MSAVI2	-0.57	-0.35	-0.62	0.56	-0.28	0.48	0.52	0.52	-0.27	-0.40
GSAVI	-0.55	-0.30	-0.46	0.65	-0.13	0.58	0.61	0.61	-0.12	-0.25
GNDVI	-0.55	-0.30	-0.46	0.65	-0.13	0.58	0.61	0.61	-0.12	-0.25
GCI	-0.61	-0.37	-0.54	0.61	-0.22	0.54	0.58	0.57	-0.23	-0.35
NDWI	-0.63	-0.42	-0.66	0.42	-0.37	0.35	0.39	0.37	-0.54	-0.62
NDVIre	-0.53	-0.32	-0.57	0.61	-0.26	0.52	0.56	0.57	-0.24	-0.37
Cire	-0.56	-0.35	-0.61	0.58	-0.31	0.49	0.54	0.54	-0.30	-0.42
MSRre	-0.55	-0.34	-0.60	0.59	-0.29	0.50	0.55	0.55	-0.28	-0.40
NDWI2	0.55	0.30	0.46	-0.65	0.13	-0.58	-0.61	-0.61	0.12	0.25

All the highlighted combinations were then plotted and their capacity to separate the levels of damage was visually evaluated. The four best combinations of features to distinguish flood levels of damage are shown on Figure 32. Particularly, one promising observation is that the combination of band 8 (NIR) and band 12 (SWIR) as well as band 8 (SWIR) and the GCI are able to clearly separate the fields with no damage from the ones with the worst level of flood damage. Non-impacted fields seem particularly detectable from all other fields.

As regards to the flattened damage, there is not one class that can be distinctly separated from the others with any combination of features.

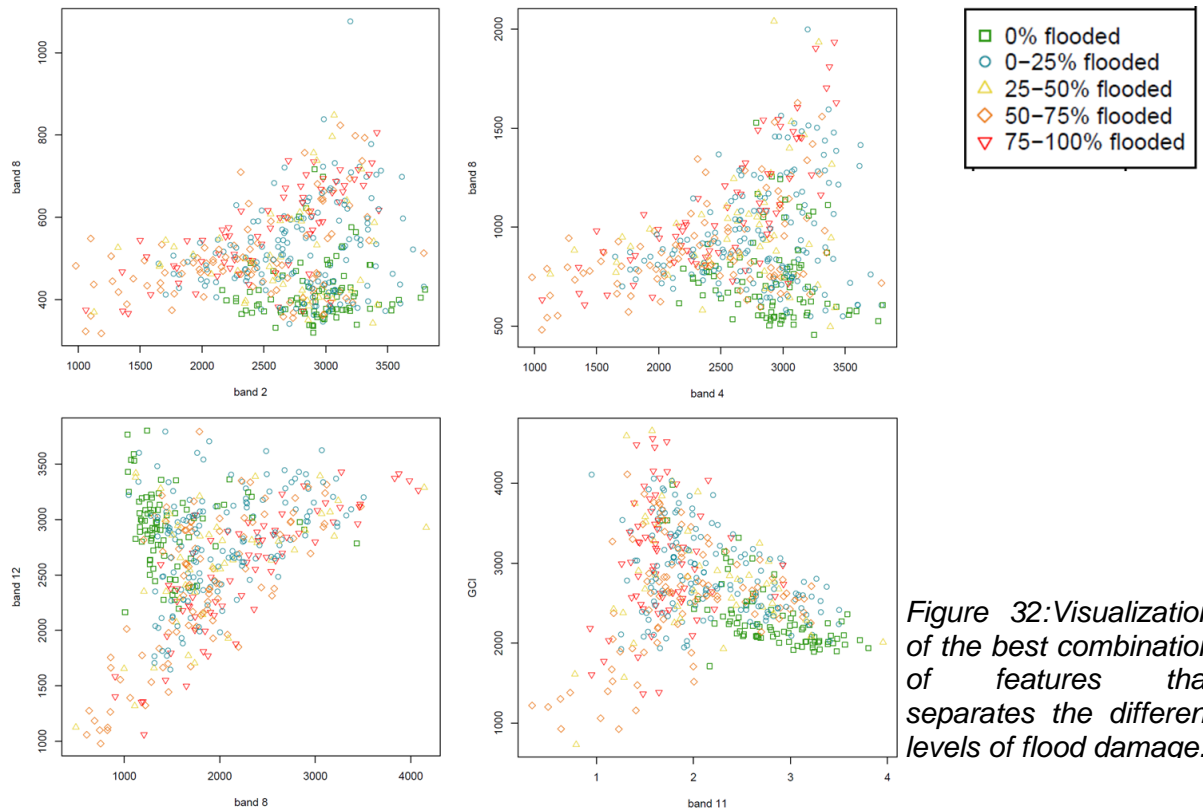


**Figure 32:** Visualization of the best combination of features that separates the different levels of flood damage.

Several results can be drawn from the sensitivity analysis and further discussed. In general, it appears that Sentinel-2 better detects flood damage than flattened damage. Indeed, from the sensitivity analysis and the data distribution investigation could be retained 2 original channels (the NIR and blue) and four derived VIs (GCI, NDWI2, CIRE and SAVI) that seem to be able to distinguish 3 levels of flood damage (the extreme ones and the intermediate levels as one category). Furthermore, the combination of the SWIR band with the NIR band and the SWIR with the GCI can distinguish the unimpacted fields from the most damaged category of flood damage and perhaps also from the intermediate categories as one class. As the flattened damage are concerned, it appears more difficult to clearly distinguish the extreme levels of damage as the data distribution analysis showed more overlaps between the spectral response of the fields from each level of damage. Besides, no combination of features could be retained. This could be due to the fact that the signal of flattened crop is more complex to detect than floods. Indeed, when crops are flattened, the plants are actually still there, green and on the ground. The resulting signal is thus a mix of green vegetation and soil in a context where the fields are of a small size and confounding factors were already present (see section VI.A.1).

## 2. Photointerpretation

The flood detection potential for the previously identified features was further investigated with a visualization of the healthy and the most impacted fields. Four spectral features (GCI, NDWI2, NIR and CIRE) and two combinations of features (Band 8 - Band 2 and Band 8 and Band 12) are shown in Figure 33. The four less

impacted fields (green, top left) are located in Ward 18 and the five most damaged ones (top right) are in Ward 16. The illustration of the green plot and the two red ones (bottom) comes from Ward 16 as well.

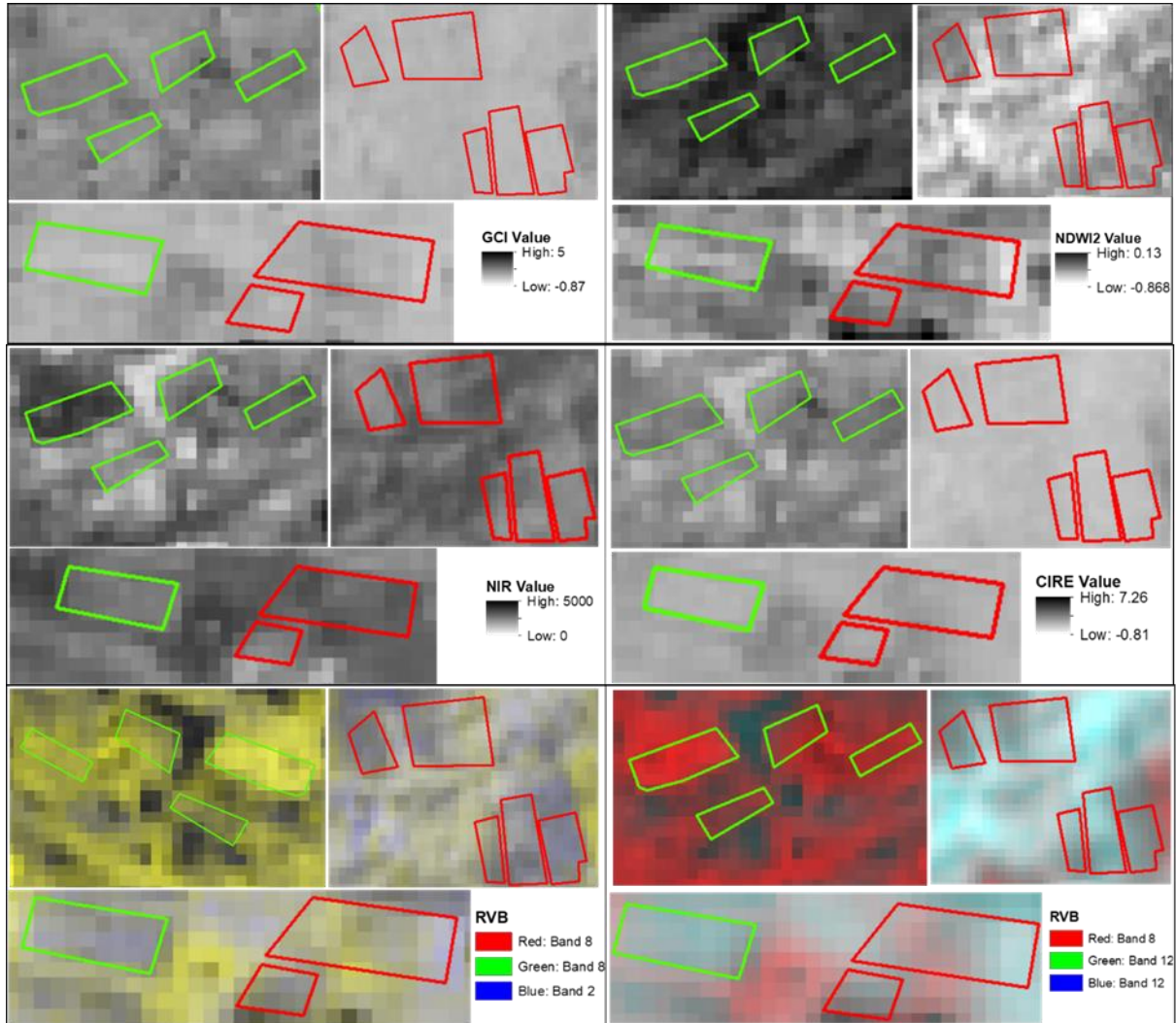
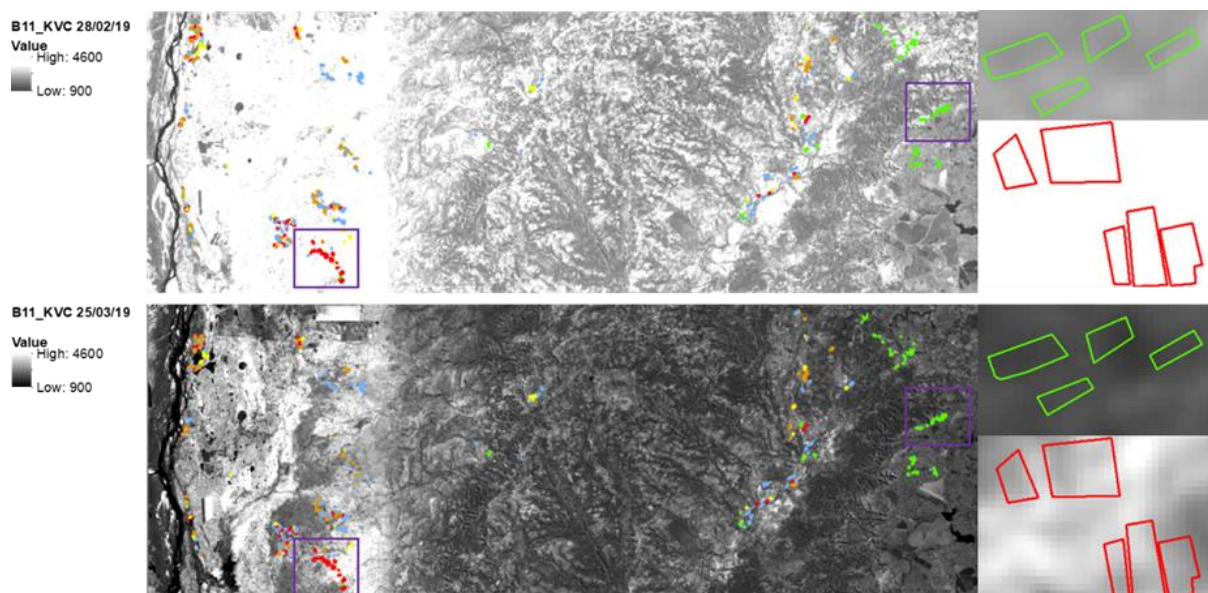


Figure 33: Visualization of the extreme classes (first level of damage in green and last in red) of flood damage on four features (GCI, NDWI2, NIR, CIRE) and two combinations of features (Band 8 - Band 2 and Band 8 and Band 12), on the 25th of March 2019.

All these features and combination of features seem to distinctively separates the signal between the undamaged fields from Ward 18 and the flooded ones from ward 16, especially the two pairs of bands and the NDWI2. The distinction between Wards is dominated by an existing gradient. Indeed, Ward 16 being initially dry and rather flat (Figure 9), it was badly impacted by the cyclone and heavy floods. On the other hand, Ward 18 is in the highlands with a contrasted topography that could facilitate the water flow and is surrounded by the forest that could temper the cyclone effects. The comparison of the two fields with opposite levels of damage in Ward 16 (bottom pair of fields) highlights the fact that the undamaged field of Ward 16 does not have the same signal as the ones from Ward 18. Indeed, the field seems more impacted in Ward 16 than Ward 18 although they are labelled with the same level of damage.

The Ward gradient is highlighted on Figure 34. The top figure represents the SWIR band on the 28<sup>th</sup> of February 2019 (before the cyclone) and the bottom figure represents the SWIR band on the 25<sup>th</sup> of March 2019 (after cyclone). The overall area is darker on the date after the cyclone, meaning that the SWIR signal intensity is lower. This can be generally translated into water covering the Chipinge area. For example, the Save River on the left of the area filled up and overflowed its banks. Also, Ward 16, which was the most arid area of Chipinge in February, shows the lowest SWIR surface reflectance values. This area also has the greatest number of flooded fields from the ground survey. The examples on the right of Figure 34 shows fields in Ward 18 (green) that were relatively humid in February and got slightly more after the cyclone. On the other hand, fields in Ward 16 (red) seem to have been completely dry in February and got under water in March.



*Figure 34: Comparison of the SWIR channel ( $1610 \pm 45 \text{ nm}$ ) of the 28th of February 2019 and the 25th of March 2019 over the study area of Chipinge. The five categories of flood damaged fields are represented in five colours (in order: green, blue, yellow, orange and red) and the two extreme classes are compared on the two dates.*

In order to get a better idea of the spectral differences between the two categories and the two dates, the delta of the surface reflectance was computed by subtracting band 11 of the 25th of March to band 11 of the 28th of February 2019 (Figure 35). The fields damaged by the flooding are displayed in colour depending on the level of damage and the two categories of fields selected before are shown on the right part of Figure 35. This computation means that if an area got flooded, the presence of water will diminish the reflectance value in the SWIR. The resulting delta value should then be positive. The regions that stayed the same such as rivers will have a delta of zero. Finally, a negative value of delta could translate the fact that in one month, more vegetation has grown and thus the signal has increased. If not flooded, the resulting value should be below zero.

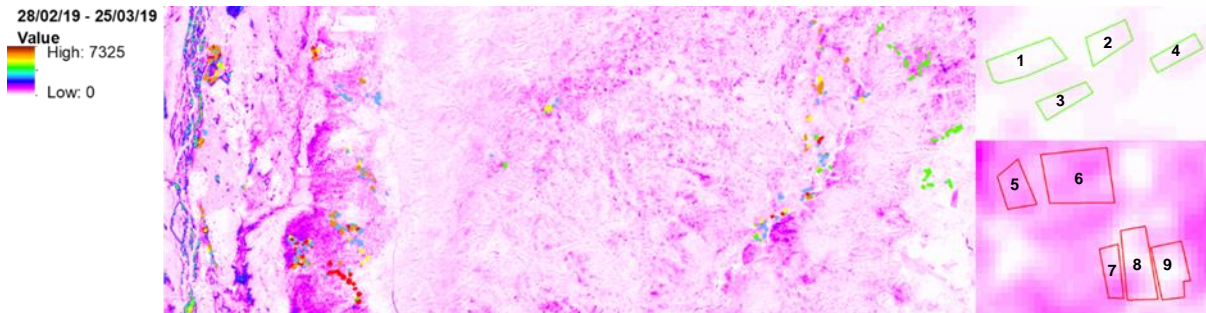


*Figure 35: Delta of surface reflectance in the SWIR channel ( $1610 \pm 45$  nm) between the 28th of February and the 25th of March over the study area of Chipinge. The five categories of flood damaged fields are represented in five colours (in order: green, blue, yellow, orange and red) and the two extreme classes are compared.*

That being said, for a matter of visualization, all the values below or equal to zero were set to zero and the positive values are thus represented in shades of purple and blue. We can see on the west part of the area that the Save River is white, and the overflowed banks are in colours. Ward 16 was clearly flooded by the cyclone and the highlands of Ward 18 seem to have been less damaged which is consistent with the ground truth data. One can now see more clearly that the red fields on the right of the figure were more impacted compared to the green ones. On Table 6 can be found the mean delta value of each polygon and the average value per category which confirms the observation.

*Table 6: Delta of SWIR surface reflectance values of flooded fields with a damage score of 1 (green) and 5 (red) and the average value of the four represented plots of each category.*

ID	Damage level	Delta	
		28/02/19 - 25/03/29	Average
1	Flooded 0-25%	46.59	
2	Flooded 0-25%	42.18	67.38
3	Flooded 0-25%	94.13	$\pm 23.19$
4	Flooded 0-25%	86.62	
5	Flooded 75-100%	544.30	
6	Flooded 75-100%	532.25	
7	Flooded 75-100%	451.31	385.79
8	Flooded 75-100%	251.61	$\pm 139.41$
9	Flooded 75-100%	215.02	

However, there is some heterogeneity within a category. For example, bottom right plots with ID 8 and 9 shown on the right of Figure 35 seems less impacted than the rest of the fields from the same category and indeed, the delta value is equal to more than half of three other represented fields. Overall, this is not an isolated case. On Figure 36 are shown three illustrations of Ward 20, Ward 16 and Ward 18 from left to right respectively. Ward 20 seems the most impacted by the cyclone and that probably from the overflow of the river. Within these three illustrations can be found several intensities of signal for one category and similar intensities between categories.

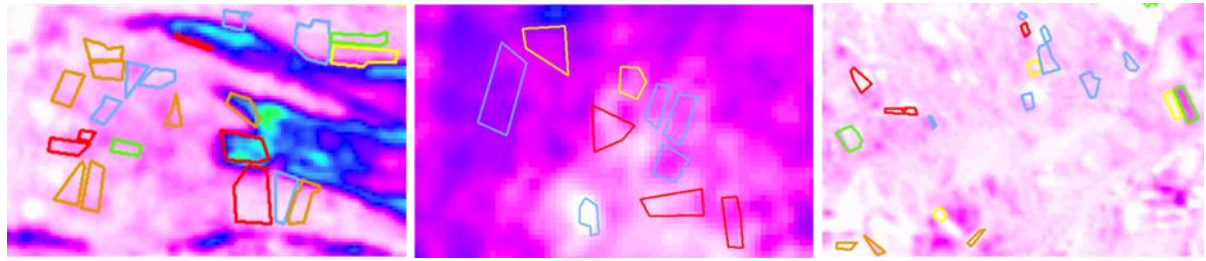


*Figure 36: Delta of SWIR surface reflectance between the 28th of February and the 25th of March 2019 in Ward 20 (left), Ward 16 (middle) and Ward 18 (right) of Chipinge. The five categories of flood damaged fields are represented in five colours (in order: green, blue, yellow, orange and red).*

To sum up, flood damage can be detected with Sentinel-2. The extreme categories of damage are particularly detectable between Wards. However, due to the presence of a gradient relative to each Ward, there is some heterogeneity in the dataset which would be problematic in a potential stage of classification of these damages. Indeed, it should be stratified by zone, which would make the work complicated, especially in terms of field data coverage. This heterogeneity may be due to the state of each field, but also potential errors that occurred during the method. Starting with the field campaign, it seems appropriate to recall that it was carried out by a team of 12 people, each covering a specific Ward. The attribution of the level of damage, although categorized as a percentage of flooded crops, remains dependent on the gradient in each Ward. Therefore, whoever assessed the damage in Ward 18 probably compared the fields between them to determine the damage and then assigned the worst score to the Ward's most impacted fields. Similarly, the person who took care of a part of Ward 20 will have assigned the lowest score to the least impacted plot that may be similar to Ward 18 intermediate damaged fields, and the same hypothesis can be applied to other classes of damage. Then comes the delineation of the polygons of each field based on a photointerpretation. These being particularly small and unclean in terms of signal, the limits were not always easy to set even with the 2 m spatial resolution Pléiades images. Finally, as mentioned above in the FAW analysis, the states of the fields are heterogeneous to start with and thus the signal within a category can be different from field to field just because of the confounding factors already present.

## C. Crop Mapping

### 1. Binary cropland mask

The cropland mask generated with Sentinel-2 image of the 31<sup>st</sup> of October and a binary training *in situ* data (crop/non-crop) is shown on Figure 37.

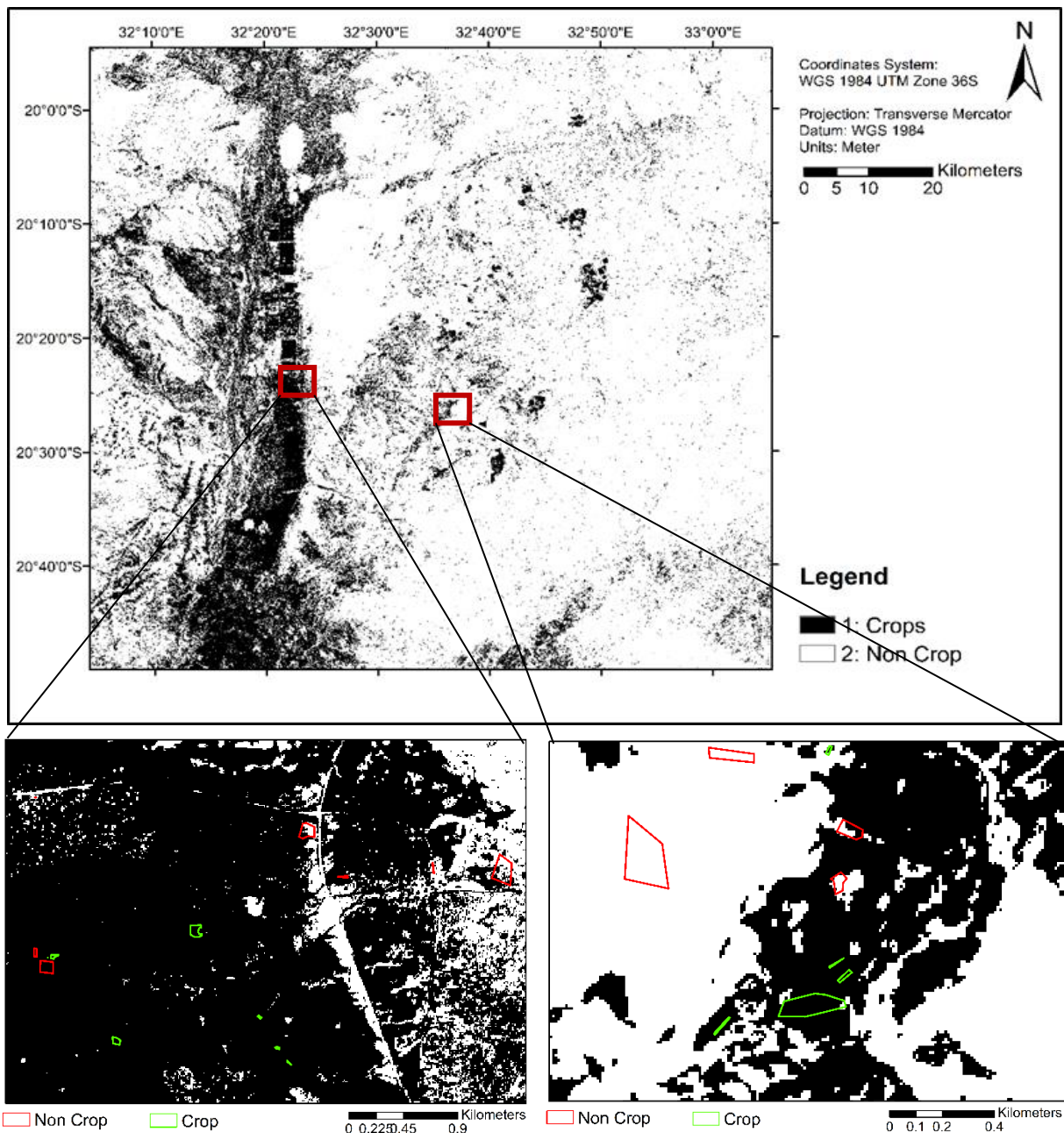


Figure 37: Crop land mask obtained over the tile covering Chipinge with one date Sentinel-2 image as input (30th of October 2018) and 2 classes of landcovers namely crop (maize, sorghum and other crops) and non-crop as well as two zoomed in sections (bottom).

Visually, this cropland mask seems to encounter several issues. First, a main area of crop misclassification is identified in the northwest part of the tile, on the left of the river, where, according to a visual comparison with Google Earth, it seems that this whole area is occupied by a natural park and therefore mainly tree cover and shrubland. Second, it appears that Ward 16 is entirely covered with crops where other land covers should be found in this area (i.e. grass and shrublands). Crop seems to have been predicted as a “patch” and lack of clear delineations. However, the zoomed in sections indicate rather well predicted pixels inside the ground truth polygons except for some non-crop on the left. This can be further discussed statistically through the confusion matrix shown on Table 7. The cropland mask was performed with an overall accuracy of 79.48%. This is mainly pulled up by the non-cropland class that has the highest F-score. Indeed, the one of cropland is of 60.97% with a precision that is much lower than recall and is of about 50%. This means that half of the predicted crops are contamination and should have been predicted as non-crop. This result should be put in perspective with the spatial distribution and size of the *in situ* validation dataset. Indeed, the validation polygons cover the three Wards of the study. Therefore, the accuracy of remote areas is not represented in the performance metrics. Areas that are visually identified as contamination would draw crop precision even more down.

*Table 7: Confusion matrix between the cropland mask of Figure 37 and the *in situ* validation dataset. Precision, recall, F-score and overall accuracy were computed based on the matrix.*

Predicted	Reference			Precision	F-score
	1	2	SUM		
1	6224	6414	12638	0.49	60.97
2	1605	24812	26417	0.93	86.08
<b>SUM</b>	<b>7829</b>	<b>31226</b>			<b>Overall Accuracy</b>
<b>Recall</b>	0.80	0.79	39055	79,48%	

## 2. Crop-type mapping

The first generated crop type map based on the previously obtained cropland mask, using the Sentinel-2 image on the 28<sup>th</sup> of February 2019 and *in situ* training dataset containing three classes of crop types (maize, sorghum and other crops) is shown on Figure 38. The errors mentioned for the cropland mask and its performance metrics must be considered for the analysis of this crop type mask.

Visually, one can notice that sorghum stands out in Ward 16 and maize in Ward 18, which is consistent with the reality of the field. The zoomed in section in Ward 16 (bottom left of Figure 38) shows ground truth maize and sorghum polygons. Generally, the classification seems satisfying. Although, some confusions seem to occur between the two crop types since some fields were predicted as maize instead of sorghum. This confusion may be due to the physiological resemblance (and thus signal resemblance) between these two crops. The zoomed in section in Ward 18 (bottom right of Figure 38) displayed with a Pléiades image underneath shows main issues encountered in the classification of this Ward which are related to the previous crop

mask. Indeed, it stands out that a major part of agricultural fields was not detected as crop at all. The circled area in the centre left of the zoom shows predicted maize and sorghum while it is actually urban (houses), shrubs and grass. The top right circle shows predicted maize where it should be grass and bare soil. Finally, the bottom right circle shows a bare soil road predicted as maize and other crops.

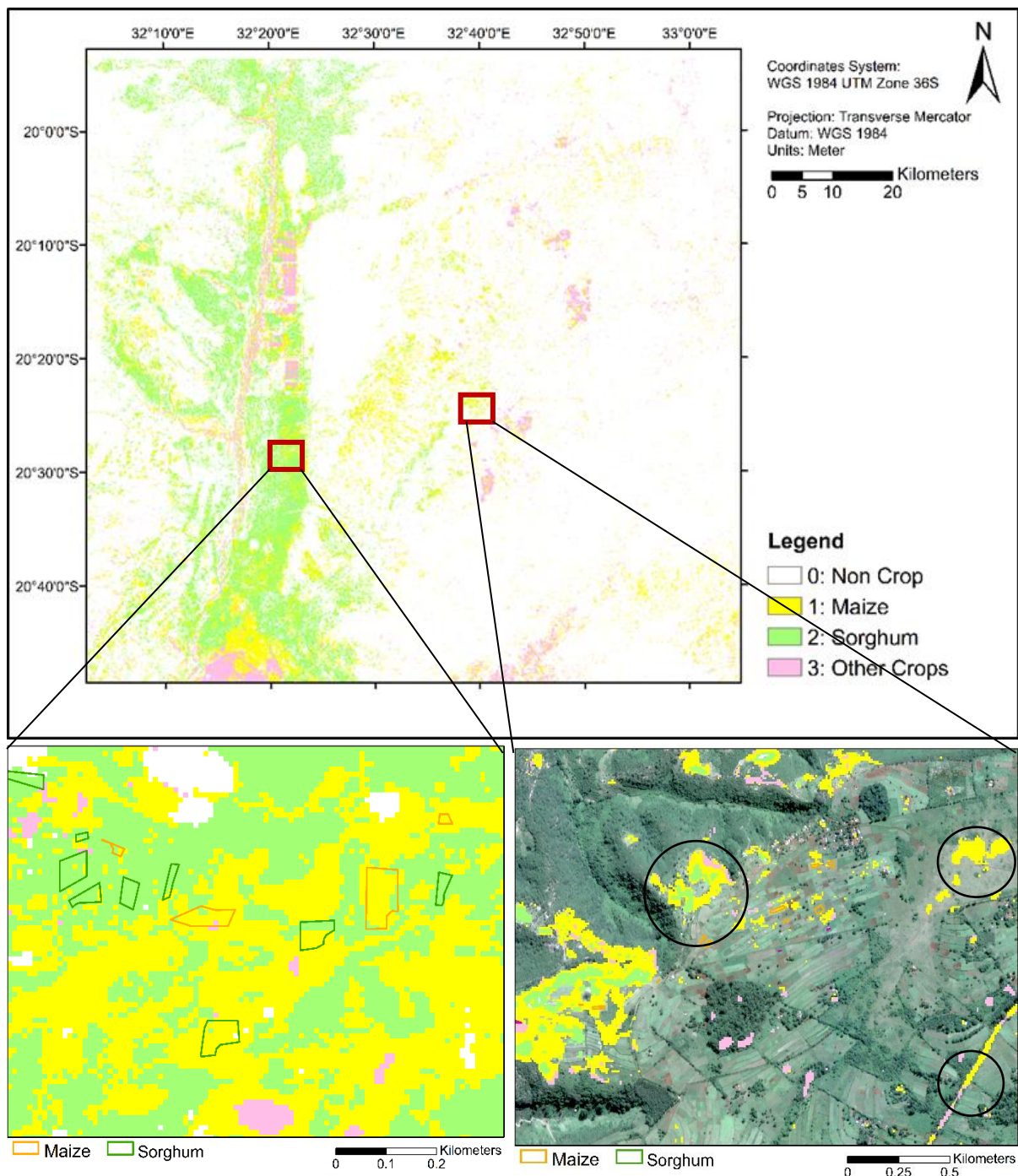


*Figure 38: Crop type mask obtained over the tile covering Chipinge with one date Sentinel-2 image as input (28th of October 2018), a crop mask obtained on the 30th of October 2018 and 3 classes of landcovers namely maize, sorghum and other crops. Two zoomed in sections are also displayed and one is shown with a Pléiades image underneath (bottom right).*

Statistically, the overall accuracy of the crop type map is of 92.59%, which is high (Table 8). However, it is mainly pulled up by the other crop class which has a F-score of 99.16% and the pixels of this class are numerous which makes them weigh a lot in the overall accuracy. The individual performances of maize and sorghum are of 71.69% and 64.98% respectively. Maize has few contamination which is good and more omissions. Indeed, maize pixels were predicted as sorghum which pulls sorghum precision down.

*Table 8: Confusion matrix between the crop type mask of Figure 38 and the in situ validation dataset. Precision, recall, F-score and overall accuracy were computed based on the matrix.*

Predicted	Reference			SUM	Precision	F-score
	1	2	3			
1	561	86	19	666	0.84	71.69
2	296	374	2	672	0.54	64.98
3	19	19	4865	4903	0.99	99.16
<b>SUM</b>	<b>876</b>	<b>479</b>	<b>4886</b>	<b>6241</b>	<b>Overall Accuracy</b>	
<b>Recall</b>	<b>0.62</b>	<b>0.8</b>	<b>0.99</b>		<b>92.59%</b>	

In light of the good statistical results and the mitigated visual accuracy assessment, several observations can be made and discussed.

First, as already mentioned, the spatial distribution and representativeness of the validation samples must be considered as it positively influences the performance metrics.

Second, the signal purity of crop classes in the training sample should also be discussed. Indeed, crop fields pixels in Ward 16 are characterized by a mixture of maize/sorghum plants, grasses and/or weeds and bare soil while in Ward 18 they are of a very small size (about four pixels after buffer) and surrounded by hedges, trees, and houses. As it was highlighted in Figure 38, a lot of Ward 18 fields were not detected and instead, grasses and bare soil were classified as crop. Besides, inside the maize or sorghum class, there are more training samples over Ward 16 than Ward 18. One hypothesis is that samples of Ward 18 were overlooked by the RF classifier and the signal of grass and bare soil in Ward 18 was close to the signal of crop fields in Ward 16.

Finally, the spatial distribution of the training sample can also explain the issues encountered remotely. Indeed, the contamination in the national park could mean that the shrublands and tree covers away from the training sample area have a slightly different spectral profile. The confusion being with maize and sorghum, it means that shrublands in the national park have a similar signal than maize and sorghum. A comparison of the national park area and Ward 16 on Sentinel-2 image and Google Earth is shown on Figure 39. There appears to be signal similarities between the contaminated zone of the National Park and maize/sorghum fields of Ward 16.

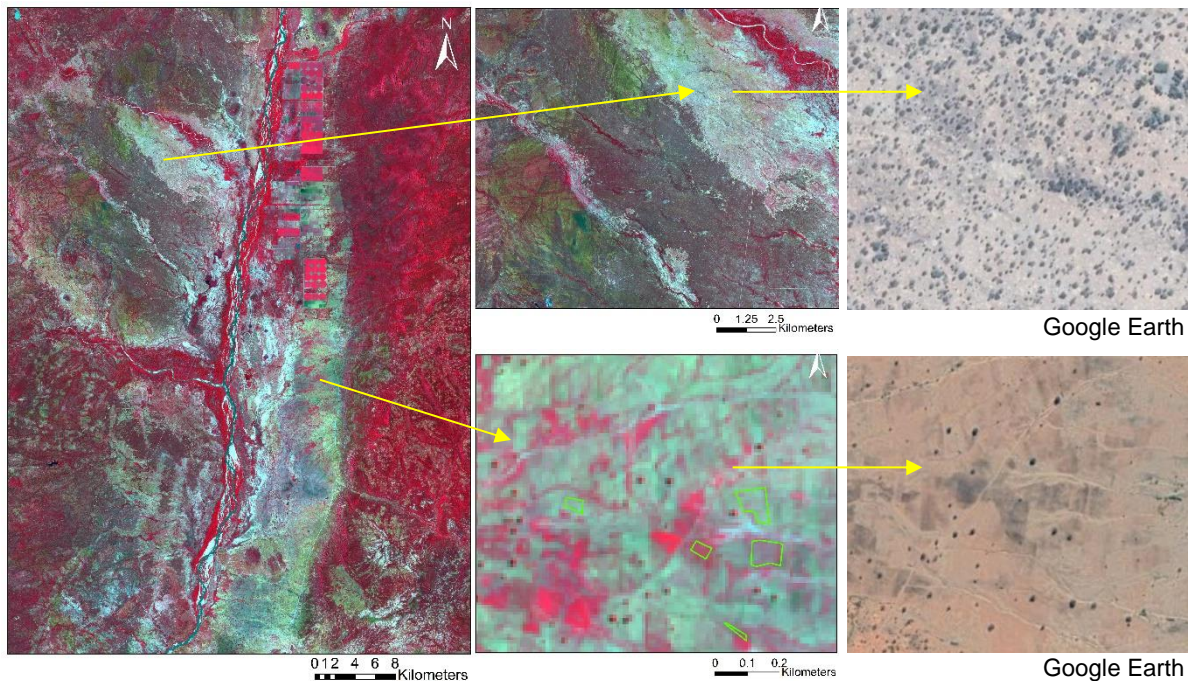


*Figure 39: Visualization on the 28<sup>th</sup> of February Sentinel-2 image of the National park (middle top) and fields in Ward 16 (middle bottom) as well as on Google Earth imagery (right)*

Following these results, a classification with landcovers stratified to each zone was performed. The input shapefile was modified, and the classes of maize and sorghum were divided into three wards. Moreover, training samples were added in the natural park area to specify the variety of signal encountered for shrubland meaning shrubs on bare soil, shrubs on grass and shrubland. The polygons were purified to a maximum. Only the pixels that were pure both on the 31<sup>st</sup> of October and the 28<sup>th</sup> of February were kept with a minimum of 4 pixels. Multiple classifications were performed, and none showed satisfactory results. Each time a class was taking over the others especially between crops, grass and shrublands that are the ones that appear to be the closest to each other in terms of signal. Also, there was systematically a class that was not predicted and there was still confusion in the area of the natural park. A resulting classification is shown on Figure 40. Visually, it looks like there is almost no more contamination in the natural park area (bottom left of Figure 40). The save riverbanks do not seem contaminated by crops either. On the other hand, maize and sorghum are misclassified, especially in ward 16 where sorghum is almost entirely confused with grass and shrublands (bottom centre of Figure 40). Crop fields in Ward 18 are still not detected and sorghum is contaminating hedges and shrubs (bottom right of Figure 40). Also, the predicted water and rocks in the bottom of the tile should be classified as crops like in the previous classification. Statistically, the F-score of maize and sorghum (48% and 4% respectively) confirms the visual observations. An important confusion occurs between tree covers, shrubs, grasses and sorghum.

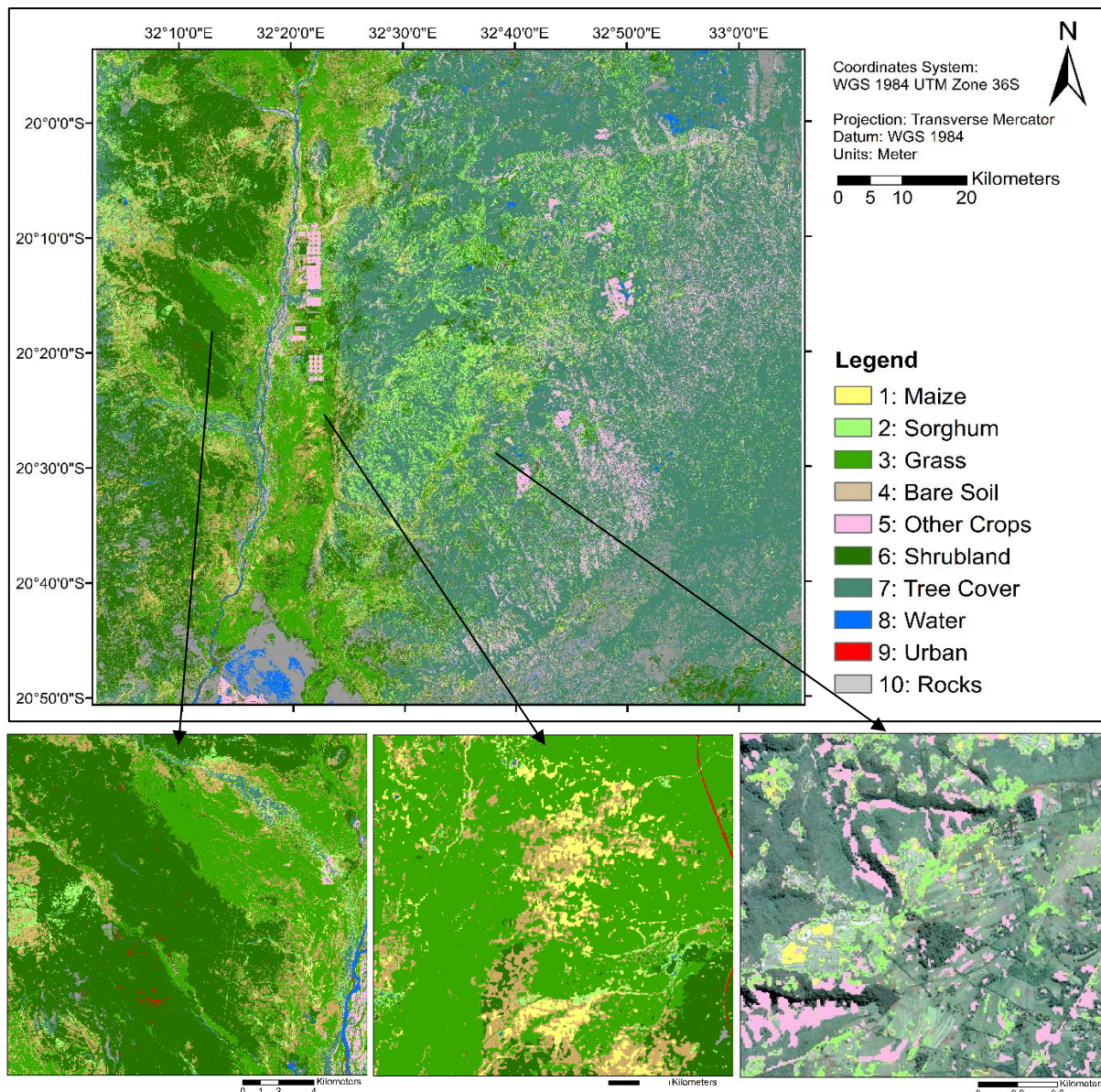


**Figure 40:** Crop type map generated with two dates Sentinel-2 images as input (30th of October 2018 and 28th of February 2019) and in situ training data containing 10 classes of land covers. Each class was stratified and split into subclasses according to wards and problematic areas. There are three zoomed in sections of the Natural Park (left), Ward 16 (middle) and Ward 18 (right).

**Table 9:** Confusion matrix between the crop type mask of Figure 40 and the in situ validation dataset. Precision, recall, F-score and overall accuracy were computed based on the matrix

Reference	4	5	7	8	9	10	6	3	1	2	SUM	Precision	F-score
Predicted	BS	OC	TC	Water	Urban	Rocks	Shrub	Grass	Mais	Sorgho			
4 BS	3656	0	0	0	12	0	216	116	0	0	4000	0.91	0.93
5 OC	4	8357	2410	0	1	0	169	174	0	0	11115	0.75	0.75
7 TC	0	907	9227	0	1	32	0	0	0	0	10167	0.91	0.82
8 Water	0	1706	0	951	2	0	0	0	0	0	2659	0.36	0.53
9 Urban	0	7	0	7	34	26	0	0	0	0	74	0.46	0.22
10 Rocks	0	13	0	0	0	615	0	0	0	0	628	0.98	0.95
6 Shrub	0	24	71	2	89	0	6010	339	43	0	6578	0.91	0.68
3 Grass	201	189	288	0	92	0	3095	1243	334	267	5709	0.22	0.33
1 Mais	0	11	10	0	0	0	162	18	422	46	669	0.63	0.48
2 Sorgho	2	18	260	0	0	0	1337	43	299	47	2006	0.02	0.04
<b>SUM</b>	3863	11232	12266	960	231	673	10989	1933	1098	360	43605	<b>Overall Accuracy</b>	
<b>Recall</b>	0.95	0.74	0.75	0.99	0.15	0.91	0.55	0.64	0.38	0.13		70.09%	

The results of this second crop type classification attempt can be discussed in parallel with the first crop type classification.

If we strictly compare what was done differently between the two crop types classifications, one can understand that in the first case, the shapefile was not constructed to embrace the diversity of shrublands and grasslands which signals were then overlapped by those of crops. Indeed, both classes are quite similar throughout the year. Shrublands are rather unvegetated in October while the crop season has not started yet and both classes still look similar in terms of signal a few months later. In general, crop fields are not dense thus pixels of bare soils are visible. Similarly, several zones of shrublands are composed of quite sparse trees and pixels of bare soil in between. The same was noticed for grass/weeds. Thus, since the shapefile of the first crop type classification did not contain samples of shrubs on bare soil or on grassland, the areas of the national parks in Masvingo Province were contaminated with crops. On the other hand, the opposite happened for the second classification. The classes of shrublands (shrubs on bare and shrubs on grass) took over the sorghum class. Therefore, it seems that the resemblance of those classes' signals does not allow classifying such a complex environment correctly.

The third generated crop type map covers Ward 18 and uses higher spatial resolution imagery (Pléiades). The resulting classes of maize and sorghum obtained from this classification are shown on Figure 41 with the Pléiades image underneath. A zoom in the agricultural fields with the Pléiades image underneath shows us that what the algorithm really detects is crops within a field but not the field as it was sown. What was actually classified in between is grass and shrubs which can be justified with the reality of the field and the complex environment. On Table 10 are shown the validation results. The main confusions with maize are highlighted in red and are grass and shrublands which brings precision down (55%) and results in an F-score of 59%. Sorghum was not predicted probably because there are only a few fields of it in Ward 18 and the training sample was smaller than the other classes. Therefore, to get a better idea of the classification accuracy, the classes were combined and reduced to two: maize and sorghum vs. others (Table 11). One can notice that the result is much more satisfying with an F-score, precision and recall of about 63% for crops. This is better than what was obtained with Sentinel-2 since less contamination occurred but still there are limitations even with a satellite of 2 m spatial resolution. A similar classification was performed over Ward 16 with a Pléiades images of the 29th of March 2019. Once more, maize and sorghum were highly confused with grass and shrublands and showed an F-score dropping to 0.48 (Appendix 3 and 4).

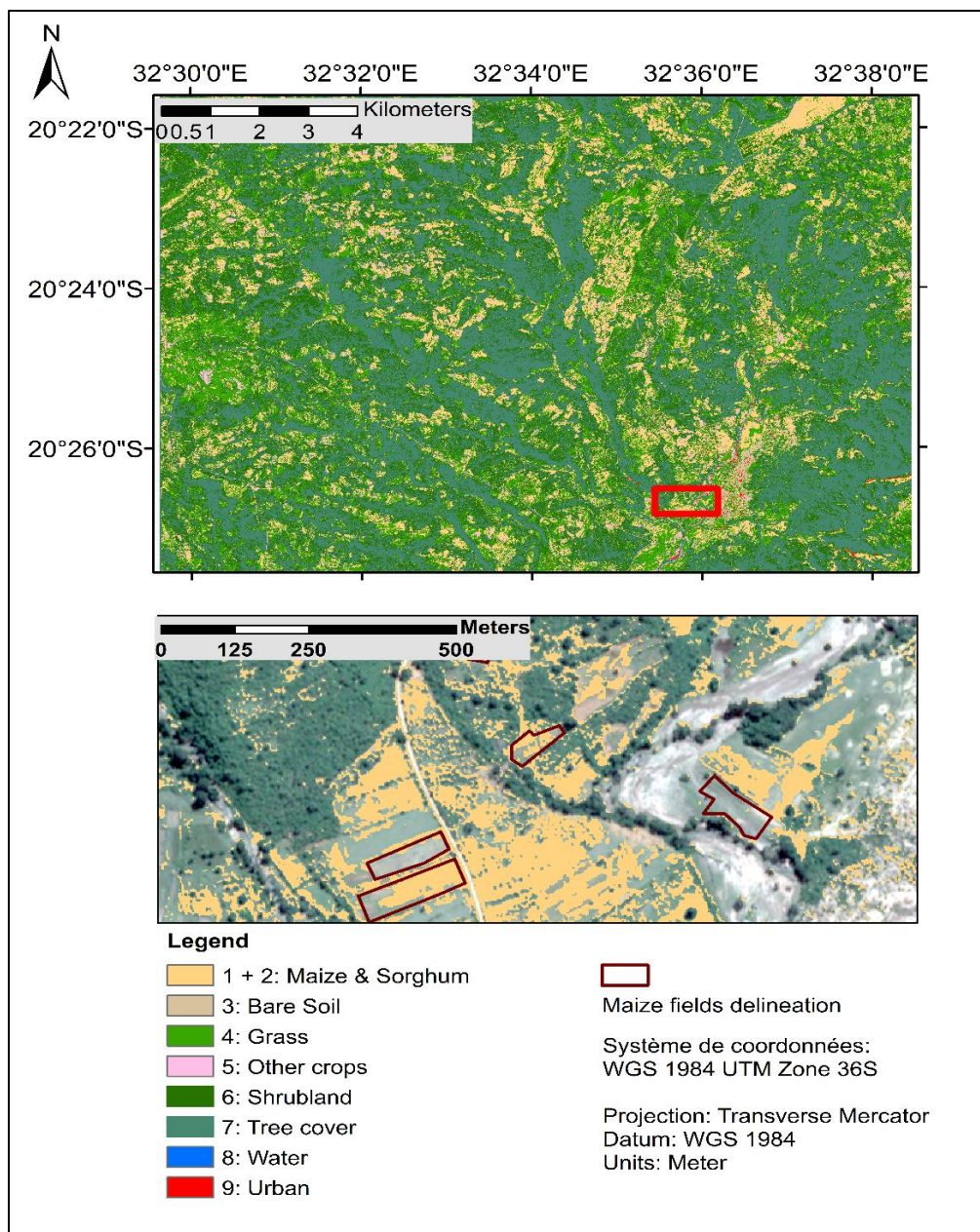


Figure 41: Crop type map generated over ward 18 of Chipinge and obtained with one Pléiades image as input (25th of March 2019) and a shapefile that contained 9 classes of landcovers.

Table 10: Confusion matrix between the crop type mask of Figure 41 and the in situ validation dataset. Precision, recall, F-score and overall accuracy were computed based on the matrix

Predicted	Reference									<b>Precision</b>	<b>F-score</b>
	1	2	3	4	5	6	7	8	9		
1	10492	1742	0	2739	647	3531	23	0	1	19175	0.55
2	0	0	0	0	0	0	0	0	0	0	0
3	15	13	662	0	151	5	0	0	168	1014	0.65
4	5086	1472	0	3387	289	8263	170	0	80	18747	0.18
5	425	127	30	7	1039	204	0	3	70	1905	0.55
6	119	0	0	111	43	25408	5180	0	4	30865	0.82
7	0	0	0	0	10	18969	12383	0	0	31362	0.39
8	0	0	0	0	0	0	0	13246	1	13247	1.00
9	0	2	157	0	14	0	0	3	555	731	0.76
<b>SUM</b>	16137	3356	849	6244	2193	56380	17756	13252	879	117046	<b>Overall Accuracy</b>
<b>Recall</b>	0.65	0.00	0.78	0.54	0.47	0.45	0.70	1.00	0.63		57.39%

Predicted	Reference		SUM	Precision	F-score
	M+S	Other			
M+S	12234	6941	19175	0.64	0.63
Other	7259	90612	97871	0.93	0.93
<b>SUM</b>	<b>19493</b>	<b>97553</b>	117046	<b>Overall Accuracy</b>	
<b>Recall</b>	0.63	0.93		87.86%	

Table 11: Reduced confusion matrix to cereals (Maize + sorghum) and other landcovers of the classification illustrated in Figure 40

## VII. General discussion

In view of the results encountered in the literature for the detection of damage, we wanted to directly test the potential of Sentinel-2, free of access, in a sub-local area of Zimbabwe. The challenges encountered in this study led us to use a trial-and-error method and so reduce the scale of work and test a higher spatial resolution. The cropland classifications we could obtain with this satellite were not suitable to use for a more precise classification that is of the damage of the plants. In fact, the production of maize/sorghum mask was the first challenge. The first step was to create a crop, non-crop mask which could be obtained with an F-score for crop of 60.97%. Once the crop pixels were isolated, the inter-variability between classes was reduced and the classification of maize, sorghum and other crops was performed. Out of the performance rate of 60.97%, maize was classified with an F-score of 71.69% and sorghum with an F-score of 64.98%. In order to improve these F-scores, it was decided to work with a 10 or more separated classes classification and examine how and why certain classes were confused. It turns out that the heterogeneity of signals for agriculture creates an overlap with the ones of shrublands and grasslands. The spatial resolution of Sentinel 2 can be questioned in the light of these results, but not only. The test of using the available Pléiades images to produce this crop mask also shows a spectral confusion with a sensor of 2 m spatial resolution. The F-score for maize and sorghum was of 63% for Ward 18 and 48% for Ward 16, both having misclassification problems with grass and shrublands. The results directly underline the challenges faced by remote sensing in smallholder agriculture in part of Zimbabwe. Indeed, those are related to a farming system that is a rain-fed production for predominantly household consumption. The agricultural landscape is composed of low-management fields, fallows, abandoned fields and many other natural vegetation types. The fields are rather shapeless, and the boundaries are not easily defined between neighbouring fields. Their size is small and there is a confusion between fields and natural vegetation. Furthermore, fields themselves are heterogeneous due to the low cropping intensity, the many scattered trees and mixed cropping. This results in a variability of spectral signatures that both tested satellites have difficulties to detect at the scale of the district.

Furthermore, the method can also be discussed especially considering recent studies that have investigated the challenges of smallholder maize mapping. Different promising methods can be mentioned and are discussed hereafter.

First, several studies have proven the efficacy of using multi-temporal imagery for improved performances. Indeed, Debats et al. (2016) used a general computer vision approach to map crop fields in South Africa using DigitalGlobe Worldview-2 imagery with a 2 m spatial resolution. They showed that multi-temporal imagery increased performances more than adding multi-spectral bands particularly for the rainfed smallholder fields. This means that the seasonal changes in texture and patterns

describe more the fields than the spectral signature. The main issue with this method is the high cost it would have been to cover only the two districts of Makoni and Chipinge all year long with very high-resolution (VHR) imagery. However, a multi-temporal technique could be used with Sentinel-2 imagery to improve the cropland mask and then the crop-type mask. Lambert et al. (2018) achieved to produce a crop-type map using Sentinel-2 time series with an existing VHR cropland mask over Mali's cotton belt. The results show an F-score of 70% and above for all the main crop types except for sorghum that did not perform that well. One prospect for our study would be to investigate more the use of time series. Although, the main problem is the cloud coverage over our area (appendix 2).

One solution to overcome the cloud issue would be to use both optical and radar data. Indeed, part of the Copernicus program consists of the Sentinel 1 mission which is composed of a Synthetic Aperture Radar (SAR) sensor. This type of instrument works independently of cloud cover and lack of illumination, it is capable of acquiring data day and night. Sentinel-1 carries a single C-band operating at a centre frequency of 5.405 GHz and in four exclusive imaging modes with different resolutions and coverage.

The mission is composed of a constellation of two satellites, Sentinel 1A and Sentinel 1B, sharing the same orbital plane and covering the entire world's land masses on a biweekly basis (ESA, 2000 - 2019). One further investigation would then be to assess Sentinel-1 potential to fill the gap of clouded Sentinel-2 images to produce our cropland and crop-type mask. More recently, Jin et al. (2019) tested the combination of the two Sentinel missions for a time series cropland and crop-type mapping over Kenya and Tanzania. They captured the seasonality by generating composite where each pixel as the median value of a feature for the season. They tested several combinations of features and it appears that SAR features in combination with optical ones could improve the cropland mask accuracy over Tanzania where cloud-free images were scarcer. On the other hand, they found out that the crop-type mask was not performing as well as expected and that it relied much more on spectral features.

A third suggestion would be to consider an OBIA over our study sites. The main issue with this technique is to accurately delineate the fields due to their small size, irregular shapes and lack of physical boundaries between each other. However, a recent study has investigated the potential of a fully convolutional network in combination with a globalization and grouping algorithm to segment VHR of WorldView-2/3 over two study areas in Nigeria and Mali (Persello et al., 2019). The convolutional network is trained to detect field boundaries despite the complex landscape. The detected sparse contours are then used to extract a hierarchy of closed segments employing the Oriented Watershed Transform (OWT) and iteratively merging adjacent regions based on the average strength of their common boundary (*Ibid.*). Finally, this hierarchy information is used by a combinatorial grouping algorithm to determine the field segments. They could demonstrate an F-score for field boundaries delineation of 0.7

and 0.6 for both study areas. Their research also highlights the usefulness of the 0.5 m panchromatic band to detect the transition in the textural patterns between fields composed of narrow crop rows. For fields with sparser vegetation, the use of the pan-sharpened multispectral bands was needed since the spectral information was more relevant to distinguish the different crop types.

Let's not forget to mention the great potential of UAV images. Although pricey, their extremely high spatial resolution would be one major solution to overcome all the challenges encountered in these landscapes. These images have proved their efficiency in many precision agriculture applications. However, planning UAV flights is not an easy process. Indeed, it was initially planned to cover both of our study areas with UAV but it was impossible due to administrative issues in Zimbabwe.

One can also mention the extent of the ground truthing coverage. Indeed, the challenges we came across during this work led us to expand our training areas by adding polygons in order to cover the diversity of landcovers in the landscape. This was based mainly on photointerpretation. However, the not so clear transition between fields and other vegetation types led us to some arbitrariness in positioning the field boundaries. More data concerning the landcovers could also enhance work like this. This could be done by spending more time on the field collecting data but also via already existing surveys or future ones. Indeed, an NGO like GOAL who helped us during this work is constantly in action in the field and makes several data collections. Agreements to collect some additional landcovers data by survey they carry out, could after some time, form an even more accurate database. For the specific case of Fall Armyworm, one can mention the recent development of the FAO FAMEWS global platform. It is an online app to be used whenever a field infested by FAW is scouted via a rigorous protocol explained on the app or when pheromone traps are checked. All the data are georeferenced and free of access. Recently, around mid-May, the app was used for the first time in Zimbabwe. By the time this app will get more famous, this could represent one major database available for new investigations.

In general, we can end up discussing what could have been done differently. Indeed, the fact that we started to work with Sentinel 2 was probably not the best choice after the knowledge we acquired during our time in the field. Besides, the studies cited above all rely on VHR images which already encountered challenges in smallholder agriculture landscape. We could therefore have planned to start with higher resolution directly. However, this choice was made because we could not get the drone images initially planned and therefore only order Pléiades images later on, and that is after, unfortunately, the cyclone hit.

## VIII. Conclusion and prospects

It is now appropriate to dive back into the objectives initially defined at the beginning of this work and to evaluate in which way we were able to respond to them. Our main objective was to evaluate Sentinel-2 capacity in detecting damage on maize in a smallholder agricultural landscape.

Firstly, we looked at defoliation damage due to Fall Armyworm. It turns out that those damage are rather patchy within a field. This in combination with a complex landscape, one must conclude that Sentinel-2 does not have the spatial characteristic to overcome the configuration of these smallholder fields that, on top of the already existing confounding factors, suffered from intense drought. Secondly, this work took a turn after Cyclone Idai hit our study area. Chipinge being badly impacted by extensive floods and heavy winds, it was decided to evaluate Sentinel-2 capacity in detecting the resulting damage. As results, it appears possible to detect flood damage. Indeed, some features, namely the GCI, NDWI2, the NIR band and the CIRE that uses a band in the red-edge appears to be able to differentiate the extreme classes of damage. However, we could also notice that the distribution of the data was overlapping between levels which creates quite confusion. Furthermore, by comparing Sentinel-2 images before and after the Cyclone, we could clearly see with the SWIR band the areas that got flooded. However, there were some inadequacies between what we could visually see and the ground truth data which highlights the great challenges when it comes to using remote sensing in complex environment. This work has therefore highlighted the difficulties that must be overcome in order to be able to detect crop damage remotely in a context of small-scale agriculture and Sentinel-2 shows limitations for this work.

An intermediate objective of this master thesis was to create a crop-type mask and more specifically a maize/sorghum mask. The first step was to create a cropland mask by using one date image before the crop season started and the result could be obtained with an F-score for crop of 60.97% and an OA of 79.48%. Once the crop pixels were isolated, the inter-variability between classes was reduced and the classification of maize, sorghum and other crops was performed on a one date image during the crop season. Out of the performance rate of 60.97%, maize was classified with an F-score of 71.69%, sorghum with an F-score of 64.98% and other crops with one of 99.16%. The OA of this second step was of 92.59%. The validated area shows thus satisfactory results. However, one should note that our visual validation could highlight multiple misclassified areas and the confusion mainly occurred with grasslands and shrublands which signals overlap with crops' ones. Afterwards, VHR imagery was tested to produce the cropland mask. The F-score for maize and sorghum was of 63% for Ward 18 and 48% for Ward 16, both having misclassification problems with grass and shrublands. The VRH sensor's characteristics thus show some limitations as well and these issues might be highly related with the

characteristics of the fields in Zimbabwe that are of small size and rainfed, plus the unusual climatic situation on this crop season.

To sum up, the use of remote sensing for crop damage detection comes with challenges in a context of smallholder agriculture. However, this work could highlight many of them and opens the door on several perspectives. Indeed, detecting damage would seem more appropriate with VHR and UAV imagery. To overcome the spectral overlap between the levels of damage, one could test the use of hyperspectral imagery on station in order to isolate their signal. Now to produce a crop-type mask over these landscapes, the same recommendations can be made but not only. Sentinel-2 time series have shown successful results in the past and to overcome the cloud coverage issue, the use of Sentinel-1 SAR sensor might be an option to consider. More investigations should be made in this field since these applications could have tremendous beneficial effects for the concerned farmers.

## IX. Bibliography

- Adelabu, S., Mutanga, O., Adam, E., 2014. Evaluating the impact of red-edge band from Rapideye image for classifying insect defoliation levels. *ISPRS J. Photogramm. Remote Sens.* 95, 34–41. <https://doi.org/10.1016/j.isprsjprs.2014.05.013>
- Agritex, 2017. Rainfall characteristics in the five natural regions of Zimbabwe. URL <http://www.moa.gov.zw/index.php/zim/> (accessed 6.6.19).
- Ashley, T.R., 1986. Geographical Distributions and Parasitization Levels for Parasitoids of the Fall Armyworm, *Spodoptera frugiperda*. *Fla. Entomol.* 69, 516. <https://doi.org/10.2307/3495384>
- Barfield, C.S., Mitchell, E.R., Poeb, S.L., 1978. A Temperature-Dependent Model for Fall Armyworm Development<sup>1,2</sup>. *Ann. Entomol. Soc. Am.* 71, 70–74. <https://doi.org/10.1093/aesa/71.1.70>
- Barton, C.V.M., 2012. Advances in remote sensing of plant stress. *Plant Soil* 354, 41–44. <https://doi.org/10.1007/s11104-011-1051-0>
- Baudron, F., Zaman-Allah, M.A., Chaipa, I., Chari, N., Chinwada, P., 2019. Understanding the factors influencing fall armyworm (*Spodoptera frugiperda* J.E. Smith) damage in African smallholder maize fields and quantifying its impact on yield. A case study in Eastern Zimbabwe. *Crop Prot.* 120, 141–150. <https://doi.org/10.1016/j.cropro.2019.01.028>
- Behmann, J., Steinrücken, J., Plümer, L., 2014. Detection of early plant stress responses in hyperspectral images. *ISPRS J. Photogramm. Remote Sens.* 93, 98–111. <https://doi.org/10.1016/j.isprsjprs.2014.03.016>
- Boegh, E., H. Soegaard, N. Broge, C. Hasager, N. Jensen, K. Schelde, and A. Thomsen, 2002. Airborne Multi-spectral Data for Quantifying Leaf Area Index, Nitrogen Concentration and Photosynthetic Efficiency in Agriculture. *Remote Sensing of Environment* 81, 179–193. [https://doi.org/10.1016/S0034-4257\(01\)00342-X](https://doi.org/10.1016/S0034-4257(01)00342-X)
- Boschetti, M., Nutini, F., Manfron, G., Brivio, P.A., Nelson, A., 2014. Comparative Analysis of Normalised Difference Spectral Indices Derived from MODIS for Detecting Surface Water in Flooded Rice Cropping Systems. *PLoS ONE* 9, e88741. <https://doi.org/10.1371/journal.pone.0088741>
- Breiman Leo, 2001. Random Forest, in: Machine Learning. pp. 5–32.
- Bruzzone, L., Serpico, S.B., 2000. A technique for feature selection in multiclass problems. *Int. J. Remote Sens.* 21, 549–563. <https://doi.org/10.1080/014311600210740>
- Capinera, J.L., 2017. Fall Armyworm, *Spodoptera frugiperda* (J.E. Smith) (Insecta: Lepidoptera: Noctuidae) [WWW Document]. URL <http://edis.ifas.ufl.edu/in255> (accessed 10.18.18).
- Capinera, John L., 2000. Fall armyworm, *Spodoptera frugiperda* (J.E. Smith), Featured Creatures, University of Florida [WWW Document]. Featur. Creat. Entomol. Nematol. URL

[http://entnemdept.ufl.edu/creatures/field/fall\\_armyworm.htm#top](http://entnemdept.ufl.edu/creatures/field/fall_armyworm.htm#top) (accessed 1.11.19).

Chemura, A., Mutanga, O., Dube, T., 2017. Separability of coffee leaf rust infection levels with machine learning methods at Sentinel-2 MSI spectral resolutions. *Precis. Agric.* 18, 859–881. <https://doi.org/10.1007/s11119-016-9495-0>

Clyde William Sanger, Kenneth Ingham et al., 2019. Zimbabwe. *Zimbabwe. Encycl. Br.*

Davis, F.M. (usda-A., Ng, S.S., Williams, W.P., 1992. Visual rating scales for screening whorl-stage corn for resistance to fall armyworm. *Tech. Bull. - Miss. Agric. For. Exp. Stn. USA.*

Debats, S.R., Luo, D., Estes, L.D., Fuchs, T.J., Caylor, K.K., 2016. A generalized computer vision approach to mapping crop fields in heterogeneous agricultural landscapes. *Remote Sens. Environ.* 179, 210–221. <https://doi.org/10.1016/j.rse.2016.03.010>

Drusch, M., Del Bello, U., Carlier, S., Colin, O., Fernandez, V., Gascon, F., Hoersch, B., Isola, C., Laberinti, P., Martimort, P., Meygret, A., Spoto, F., Sy, O., Marchese, F., Bargellini, P., 2012. Sentinel-2: ESA's Optical High-Resolution Mission for GMES Operational Services. *Remote Sens. Environ.* 120, 25–36. <https://doi.org/10.1016/j.rse.2011.11.026>

Dumas, P., Legeai, F., Lemaitre, C., Scaon, E., Orsucci, M., Labadie, K., Gimenez, S., Clamens, A.-L., Henri, H., Vavre, F., Aury, J.-M., Fournier, P., Kerfoot, G.J., d'Alençon, E., 2015. *Spodoptera frugiperda* (Lepidoptera: Noctuidae) host-plant variants: two host strains or two distinct species? *Genetica* 143, 305–316. <https://doi.org/10.1007/s10709-015-9829-2>

Erickson, B.J., Johannsen, C.J., Vorst, J.J., Biehl, L.L., 2004. Using Remote Sensing to Assess Stand Loss and Defoliation in Maize. *Photogramm. Eng. Remote Sens.* 70, 717–722. <https://doi.org/10.14358/PERS.70.6.717>

ESA, n.d. Sentinel Data Access Overview - Sentinel Online [WWW Document]. URL <https://sentinel.esa.int/web/sentinel/sentinel-data-access> (accessed 4.10.19).

European Space Agency (ESA), 2000. Sentinel-1 - Missions - Sentinel Online [WWW Document]. URL <https://sentinel.esa.int/web/sentinel/missions/sentinel-1> (accessed 7.13.19).

Famine Early Warning System Network, n.d. Zimbabwe | Famine Early Warning Systems Network [WWW Document]. URL <http://fews.net/southern-africa/zimbabwe> (accessed 3.25.19).

FEWS NET, USAID, 2019. Southern Africa Food Security Alert [WWW Document]. URL <http://fews.net/southern-africa/alert/february-1-2019> (accessed 6.16.19).

Food and Agriculture Organization of the United Nations, 2019. Map of areas affected by Fall Armyworm in Africa and Asia : FAO in Emergencies [WWW Document]. URL <http://www.fao.org/emergencies/resources/maps/detail/en/c/902959/> (accessed 8.16.19).

Food and Agriculture Organization of the United Nations, 2019. 2018/19 El-Niño [WWW Document]. URL <https://reliefweb.int/report/zimbabwe/fao-2019-humanitarian-appeal-201819-el-ni-o-response-plan-southern-africa> (accessed 6.16.19).

- Food and Agriculture Organization of the United Nations, 2018. Integrated management of the fall armyworm on maize: a guide for farmer field schools in Africa.
- Franke, J., Menz, G., 2007. Multi-temporal wheat disease detection by multi-spectral remote sensing. *Precis. Agric.* 8, 161–172. <https://doi.org/10.1007/s11119-007-9036-y>
- Gao, B., 1996. NDWI—A normalized difference water index for remote sensing of vegetation liquid water from space. *Remote Sens. Environ.* 58, 257–266. [https://doi.org/10.1016/S0034-4257\(96\)00067-3](https://doi.org/10.1016/S0034-4257(96)00067-3)
- Gitelson, A., Merzlyak, M.N., 1994. Spectral Reflectance Changes Associated with Autumn Senescence of *Aesculus hippocastanum* L. and *Acer platanoides* L. Leaves. Spectral Features and Relation to Chlorophyll Estimation. *J. Plant Physiol.* 143, 286–292. [https://doi.org/10.1016/S0176-1617\(11\)81633-0](https://doi.org/10.1016/S0176-1617(11)81633-0)
- Gitelson, A.A., 2005. Remote estimation of canopy chlorophyll content in crops. *Geophys. Res. Lett.* 32, L08403. <https://doi.org/10.1029/2005GL022688>
- Gitelson, A.A., Gritz †, Y., Merzlyak, M.N., 2003. Relationships between leaf chlorophyll content and spectral reflectance and algorithms for non-destructive chlorophyll assessment in higher plant leaves. *J. Plant Physiol.* 160, 271–282. <https://doi.org/10.1078/0176-1617-00887>
- Gitelson, A.A., Merzlyak, M.N., 1998. Remote sensing of chlorophyll concentration in higher plant leaves. *Adv. Space Res.* 22, 689–692. [https://doi.org/10.1016/S0273-1177\(97\)01133-2](https://doi.org/10.1016/S0273-1177(97)01133-2)
- Goergen, G., Kumar, P.L., Sankung, S.B., Togola, A., Tamò, M., 2016. First Report of Outbreaks of the Fall Armyworm *Spodoptera frugiperda* (J E Smith) (Lepidoptera, Noctuidae), a New Alien Invasive Pest in West and Central Africa. *PLOS ONE* 11, e0165632. <https://doi.org/10.1371/journal.pone.0165632>
- Hagolle, O., Huc, M., Villa Pascual, D., Dedieu, G., 2015. A Multi-Temporal and Multi-Spectral Method to Estimate Aerosol Optical Thickness over Land, for the Atmospheric Correction of FormoSat-2, LandSat, VENµS and Sentinel-2 Images. *Remote Sens.* 7, 2668–2691. <https://doi.org/10.3390/rs70302668>
- Harrison, R.D., Thierfelder, C., Baudron, F., Chinwada, P., Midega, C., Schaffner, U., van den Berg, J., 2019. Agro-ecological options for fall armyworm (*Spodoptera frugiperda* JE Smith) management: Providing low-cost, smallholder friendly solutions to an invasive pest. *J. Environ. Manage.* 243, 318–330. <https://doi.org/10.1016/j.jenvman.2019.05.011>
- Huete, A., Didan, K., Miura, T., Rodriguez, E.P., Gao, X., Ferreira, L.G., 2002. Overview of the radiometric and biophysical performance of the MODIS vegetation indices. *Remote Sens. Environ.* 83, 195–213. [https://doi.org/10.1016/S0034-4257\(02\)00096-2](https://doi.org/10.1016/S0034-4257(02)00096-2)
- Huete, A.R., 1988. A soil-adjusted vegetation index (SAVI). *Remote Sens. Environ.* 25, 295–309. [https://doi.org/10.1016/0034-4257\(88\)90106-X](https://doi.org/10.1016/0034-4257(88)90106-X)
- International Federation of Red Cross, 2019. Information bulletin: Zimbabwe - Cyclone Idai [WWW Document]. URL <https://reliefweb.int/report/zimbabwe/zimbabwe-cyclone-idai-information-bulletin-n-1> (accessed 6.16.19).

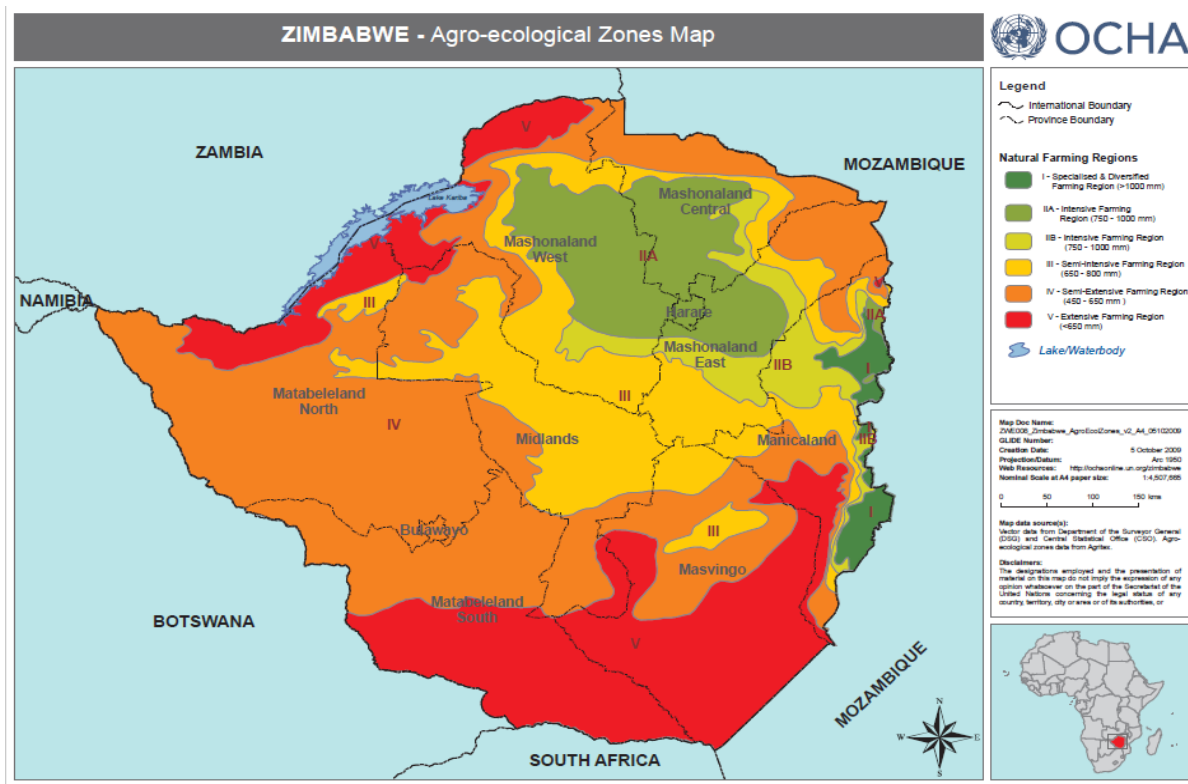
- Jin, Z., Azzari, G., You, C., Di Tommaso, S., Aston, S., Burke, M., Lobell, D.B., 2019. Smallholder maize area and yield mapping at national scales with Google Earth Engine. *Remote Sens. Environ.* 228, 115–128. <https://doi.org/10.1016/j.rse.2019.04.016>
- Johnson, S.J., 1987. Migration and the life history strategy of the fall armyworm, *Spodoptera frugiperda* in the western hemisphere. *Int. J. Trop. Insect Sci.* 8, 543–549. <https://doi.org/10.1017/S1742758400022591>
- Kumela, T., Simiyu, J., Sisay, B., Likhayo, P., Mendesil, E., Gohole, L., Tefera, T., 2019. Farmers' knowledge, perceptions, and management practices of the new invasive pest, fall armyworm (*Spodoptera frugiperda*) in Ethiopia and Kenya. *Int. J. Pest Manag.* 65, 1–9. <https://doi.org/10.1080/09670874.2017.1423129>
- Lacaux, J.P., Tourre, Y.M., Vignalles, C., Ndione, J.A., Lafaye, M., 2007. Classification of ponds from high-spatial resolution remote sensing: Application to Rift Valley Fever epidemics in Senegal. *Remote Sens. Environ.* 106, 66–74. <https://doi.org/10.1016/j.rse.2006.07.012>
- Lambert, M.-J., Traoré, P.C.S., Blaes, X., Baret, P., Defourny, P., 2018. Estimating smallholder crops production at village level from Sentinel-2 time series in Mali's cotton belt. *Remote Sens. Environ.* 216, 647–657. <https://doi.org/10.1016/j.rse.2018.06.036>
- Liu, M., Wang, T., Skidmore, A.K., Liu, X., 2018. Heavy metal-induced stress in rice crops detected using multi-temporal Sentinel-2 satellite images. *Sci. Total Environ.* 637–638, 18–29. <https://doi.org/10.1016/j.scitotenv.2018.04.415>
- Luginbill P., 1928. The fall Armyworm. U.S Dep. Agric. Tech. Bull. No. 34, pp. 1-91.
- Macauley, H., 2015. Cereal crops: rice, maize, millet, sorghum, wheat: background paper. Conference on 'Feeding Africa' Dakar, Senegal, 21–23 October 2015.
- Mas, J.F., Flores, J.J., 2008. The application of artificial neural networks to the analysis of remotely sensed data. *Int. J. Remote Sens.* 29, 617–663. <https://doi.org/10.1080/01431160701352154>
- McFEETERS, S.K., 1996. The use of the Normalized Difference Water Index (NDWI) in the delineation of open water features. *Int. J. Remote Sens.* 17, 1425–1432. <https://doi.org/10.1080/01431169608948714>
- Mohite, J., Twarakavi, N., Pappula, S., 2018. Evaluating the Potential of Sentinel-2 for Low Severity Mites Infestation Detection in Grapes, in: IGARSS 2018 - 2018 IEEE International Geoscience and Remote Sensing Symposium. Presented at the IGARSS 2018 - 2018 IEEE International Geoscience and Remote Sensing Symposium, IEEE, Valencia, pp. 4651–4654. <https://doi.org/10.1109/IGARSS.2018.8519071>
- Mountrakis, G., Im, J., Ogole, C., 2011. Support vector machines in remote sensing: A review. *ISPRS J. Photogramm. Remote Sens.* 66, 247–259. <https://doi.org/10.1016/j.isprsjprs.2010.11.001>
- Moyo, S., 2000. The Political Economy of Land Acquisition and Redistribution in Zimbabwe, 1990-1999. *J. South. Afr. Stud.* 26, 5–28. <https://doi.org/10.1080/030570700108351>

- Nagoshi, R.N., Koffi, D., Agboka, K., Tounou, K.A., Banerjee, R., Jurat-Fuentes, J.L., Meagher, R.L., 2017. Comparative molecular analyses of invasive fall armyworm in Togo reveal strong similarities to populations from the eastern United States and the Greater Antilles. PLOS ONE 12, e0181982. <https://doi.org/10.1371/journal.pone.0181982>
- NOAA, National Weather Service, 2019. ENSO: Recent Evolution, Current Status and Predictions [WWW Document]. URL [https://www.cpc.ncep.noaa.gov/products/analysis\\_monitoring/lanina/enso\\_evolution-status-fcsts-web.pdf](https://www.cpc.ncep.noaa.gov/products/analysis_monitoring/lanina/enso_evolution-status-fcsts-web.pdf) (accessed 6.16.19).
- Otim, M.H., Tay, W.T., Walsh, T.K., Kanyesigye, D., Adumo, S., Abongosi, J., Ochen, S., Sserumaga, J., Alibu, S., Abalo, G., Asea, G., Agona, A., 2018. Detection of sister-species in invasive populations of the fall armyworm *Spodoptera frugiperda* (Lepidoptera: Noctuidae) from Uganda. PLOS ONE 13, e0194571. <https://doi.org/10.1371/journal.pone.0194571>
- Oumar, Z., Mutanga, O., 2013. Using WorldView-2 bands and indices to predict bronze bug (*Thaumastocoris peregrinus*) damage in plantation forests. Int. J. Remote Sens. 34, 2236–2249. <https://doi.org/10.1080/01431161.2012.743694>
- Pashley, D.P., 1988. Current Status of Fall Armyworm Host Strains. Fla. Entomol. 71, 227. <https://doi.org/10.2307/3495425>
- Pashley, D.P., 1986. Host-associated Genetic Differentiation in Fall Armyworm (Lepidoptera: Noctuidae): a Sibling Species Complex? Ann. Entomol. Soc. Am. 79, 898–904. <https://doi.org/10.1093/aesa/79.6.898>
- Persello, C., Tolpekin, V.A., Bergado, J.R., de By, R.A., 2019. Delineation of agricultural fields in smallholder farms from satellite images using fully convolutional networks and combinatorial grouping. Remote Sens. Environ. 231, 111253. <https://doi.org/10.1016/j.rse.2019.111253>
- Prasanna, B.M., Huesing, J.E., Eddy, R., Peschke, V.M., 2018. Fall Armyworm in Africa: a guide for integrated pest management. 120.
- Qi, J., Chehbouni, A., Huete, A.R., Kerr, Y.H., Sorooshian, S., 1994. A Modified Soil Adjusted Vegetation Index. Remote Sensing of Environment 48, 119–126. [https://doi.org/10.1016/0034-4257\(94\)90134-1](https://doi.org/10.1016/0034-4257(94)90134-1)
- Rose, A.H., Silversides, R.H., Lindquist, O.H., 1975. MIGRATION FLIGHT BY AN APHID, RHOPALOSIPHUM MAIDIS (HEMIPTERA: APHIDIDAE), AND A NOCTUID, SPODOPTERA FRUGIPERDA (LEPIDOPTERA: NOCTUIDAE). Can. Entomol. 107, 567–576. <https://doi.org/10.4039/Ent107567-6>
- Rouse, W., Haas, R.H., 1974. MONITORING VEGETATION SYSTEMS IN THE GREAT PLAINS WITH ERTS 9.
- Rumpf, T., Mahlein, A.-K., Steiner, U., Oerke, E.-C., Dehne, H.-W., Plümer, L., 2010. Early detection and classification of plant diseases with Support Vector Machines based on hyperspectral reflectance. Comput. Electron. Agric. 74, 91–99. <https://doi.org/10.1016/j.compag.2010.06.009>
- Shunlin Liang, Xiaowen Li, Jindi Wang, 2012. A Systematic View of Remote Sensing, in: Advanced Remote Sensing. pp. 1–31. <https://doi.org/10.1016/B978-0-12-385954-9.00001-0>

- Simmons, A.M., Marti, O.G., 1992. Mating by the Fall Armyworm (Lepidoptera: Noctuidae): Frequency, Duration, and Effect of Temperature. Environ. Entomol. 21, 371–375. <https://doi.org/10.1093/ee/21.2.371>
- Sripada, R., et al., 2005. Determining In-Season Nitrogen Requirements for Corn Using Aerial Color-Infrared Photography. North Carolina State University.
- Wu, C., Niu, Z., Tang, Q., Huang, W., 2008. Estimating chlorophyll content from hyperspectral vegetation indices: Modeling and validation. Agric. For. Meteorol. 148, 1230–1241. <https://doi.org/10.1016/j.agrformet.2008.03.005>
- Xie, Q., Dash, J., Huang, W., Peng, D., Qin, Q., Mortimer, H., Casa, R., Pignatti, S., Laneve, G., Pascucci, S., Dong, Y., Ye, H., 2018. Vegetation Indices Combining the Red and Red-Edge Spectral Information for Leaf Area Index Retrieval. IEEE J. Sel. Top. Appl. Earth Obs. Remote Sens. 11, 1482–1493. <https://doi.org/10.1109/JSTARS.2018.2813281>
- Xu, H., 2006. Modification of normalised difference water index (NDWI) to enhance open water features in remotely sensed imagery. Int. J. Remote Sens. 27, 3025–3033. <https://doi.org/10.1080/01431160600589179>
- Xue, J., Su, B., 2017. Significant Remote Sensing Vegetation Indices: A Review of Developments and Applications. J. Sens. 2017, 1–17. <https://doi.org/10.1155/2017/1353691>
- Yuan, L., Zhang, H., Zhang, Y., Xing, C., Bao, Z., 2017. Feasibility assessment of multi-spectral satellite sensors in monitoring and discriminating wheat diseases and insects. Optik 131, 598–608. <https://doi.org/10.1016/j.ijleo.2016.11.206>
- Yuan, L., Zhang, J., Shi, Y., Nie, C., Wei, L., Wang, J., 2014. Damage Mapping of Powdery Mildew in Winter Wheat with High-Resolution Satellite Image. Remote Sens. 6, 3611–3623. <https://doi.org/10.3390/rs6053611>
- Zadoks, J.C., Chang, T.T., Konzak, C.F., 1974. A decimal code for the growth stages of cereals. Weed Res. 14, 415–421. <https://doi.org/10.1111/j.1365-3180.1974.tb01084.x>
- Zhang, J., Huang, Y., Yuan, L., Yang, G., Chen, L., Zhao, C., 2016. Using satellite multispectral imagery for damage mapping of armyworm (*Spodoptera frugiperda*) in maize at a regional scale: Using satellite images to map regional armyworm damage in maize. Pest Manag. Sci. 72, 335–348. <https://doi.org/10.1002/ps.4003>

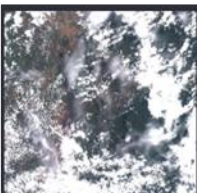
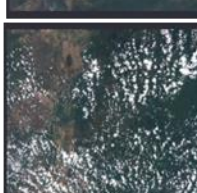
## X. Appendices

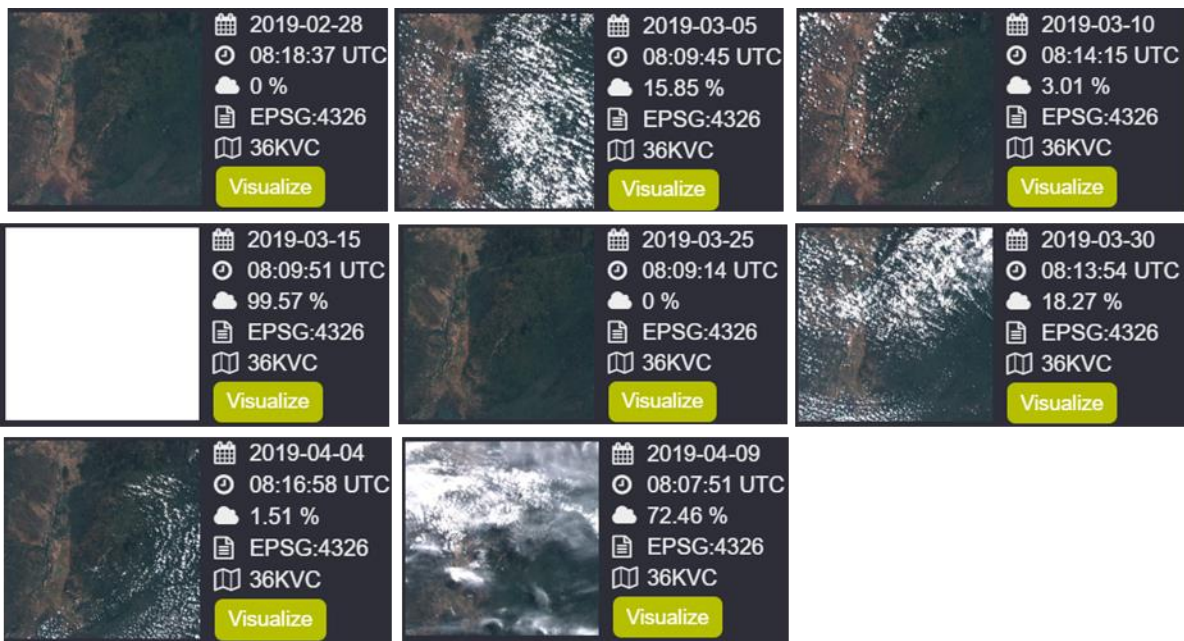
Appendix 1: Natural farming regions (NR) of Zimbabwe (map created by OCHA)



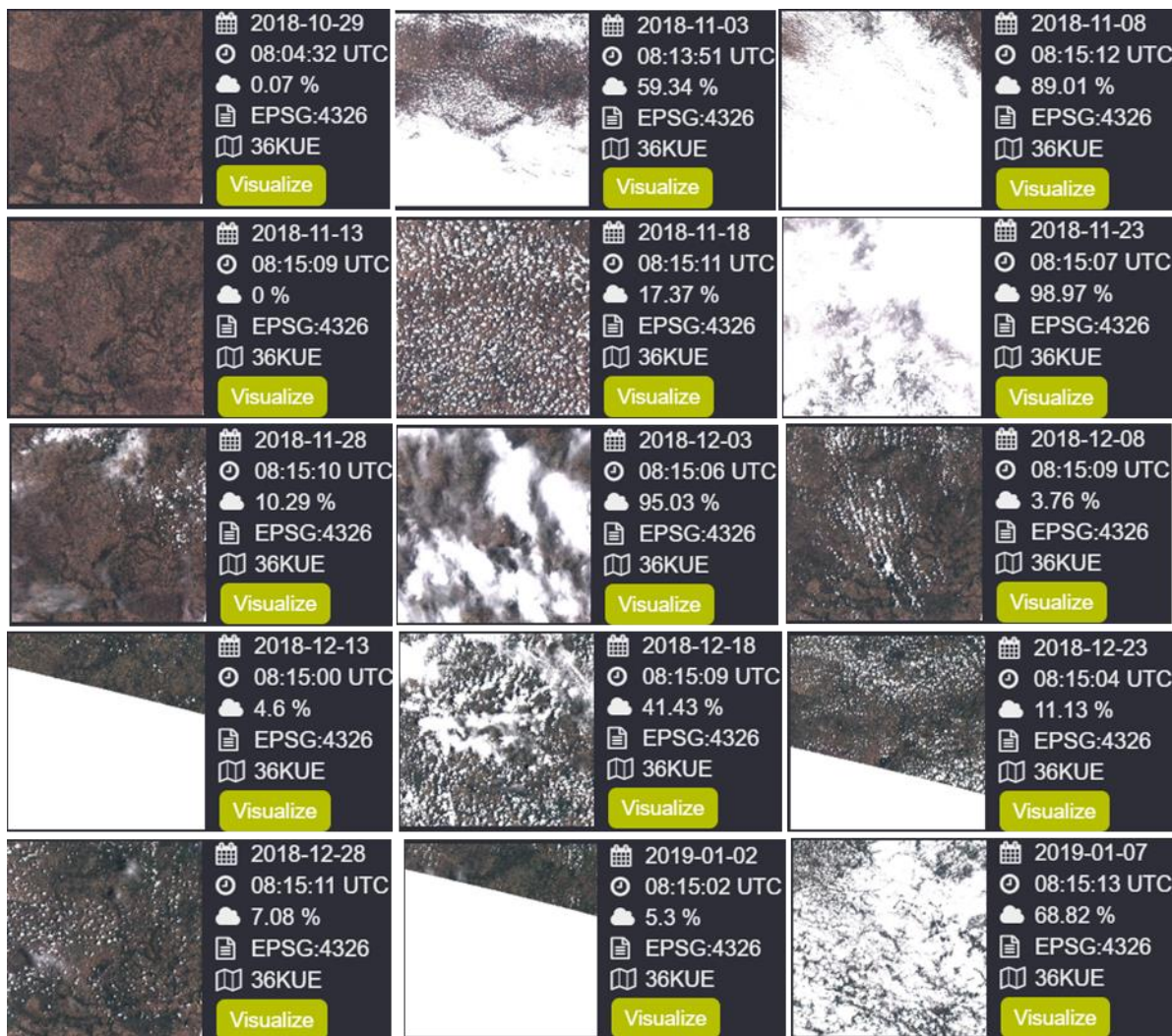
Appendix 2: View of the Sentinel-2 time series for the 2018-2019 cropping season over Chipinge (tile KVC) and Makoni (tile KUE).

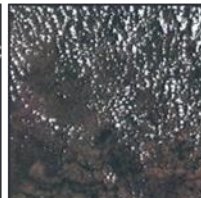
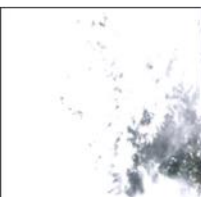
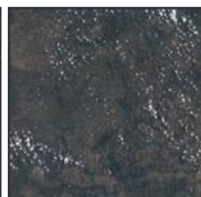
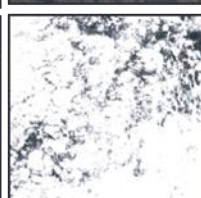
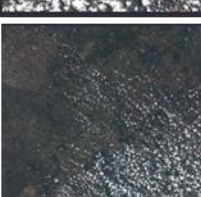
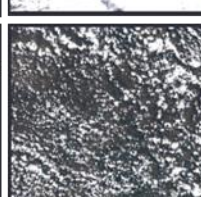
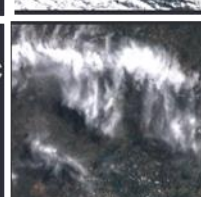
- Chipinge

	<p>2018-10-31 08:00:18 UTC 0 % EPSG:4326 36KVC</p> <p><a href="#">Visualize</a></p>		<p>2018-11-05 07:57:57 UTC 12.54 % EPSG:4326 36KVC</p> <p><a href="#">Visualize</a></p>		<p>2018-11-10 08:05:40 UTC 9.16 % EPSG:4326 36KVC</p> <p><a href="#">Visualize</a></p>
	<p>2018-11-15 08:05:42 UTC 8.63 % EPSG:4326 36KVC</p> <p><a href="#">Visualize</a></p>		<p>2018-11-20 08:05:38 UTC 0.05 % EPSG:4326 36KVC</p> <p><a href="#">Visualize</a></p>		<p>2018-11-25 08:05:41 UTC 64.56 % EPSG:4326 36KVC</p> <p><a href="#">Visualize</a></p>
	<p>2018-11-30 08:05:36 UTC 69.94 % EPSG:4326 36KVC</p> <p><a href="#">Visualize</a></p>		<p>2018-12-05 08:05:40 UTC 37.27 % EPSG:4326 36KVC</p> <p><a href="#">Visualize</a></p>		<p>2018-12-10 08:05:37 UTC 59.99 % EPSG:4326 36KVC</p> <p><a href="#">Visualize</a></p>
	<p>2018-12-15 08:05:36 UTC 26.46 % EPSG:4326 36KVC</p> <p><a href="#">Visualize</a></p>		<p>2018-12-20 08:05:36 UTC 1.16 % EPSG:4326 36KVC</p> <p><a href="#">Visualize</a></p>		<p>2018-12-25 08:05:41 UTC 96.85 % EPSG:4326 36KVC</p> <p><a href="#">Visualize</a></p>
	<p>2018-12-30 08:05:39 UTC 53.85 % EPSG:4326 36KVC</p> <p><a href="#">Visualize</a></p>		<p>2019-01-04 08:05:43 UTC 90.59 % EPSG:4326 36KVC</p> <p><a href="#">Visualize</a></p>		<p>2019-01-09 08:05:40 UTC 27.16 % EPSG:4326 36KVC</p> <p><a href="#">Visualize</a></p>
	<p>2019-01-14 08:05:44 UTC 90.58 % EPSG:4326 36KVC</p> <p><a href="#">Visualize</a></p>		<p>2019-01-19 08:05:41 UTC 50.76 % EPSG:4326 36KVC</p> <p><a href="#">Visualize</a></p>		<p>2019-01-24 08:05:45 UTC 8.44 % EPSG:4326 36KVC</p> <p><a href="#">Visualize</a></p>
	<p>2019-01-29 08:05:42 UTC 26.59 % EPSG:4326 36KVC</p> <p><a href="#">Visualize</a></p>		<p>2019-02-03 08:05:45 UTC 31.52 % EPSG:4326 36KVC</p> <p><a href="#">Visualize</a></p>		<p>2019-02-08 08:05:42 UTC 29.77 % EPSG:4326 36KVC</p> <p><a href="#">Visualize</a></p>
	<p>2019-02-13 08:05:45 UTC 49.98 % EPSG:4326 36KVC</p> <p><a href="#">Visualize</a></p>		<p>2019-02-18 08:05:41 UTC 94.79 % EPSG:4326 36KVC</p> <p><a href="#">Visualize</a></p>		<p>2019-02-23 08:16:10 UTC 0.38 % EPSG:4326 36KVC</p> <p><a href="#">Visualize</a></p>

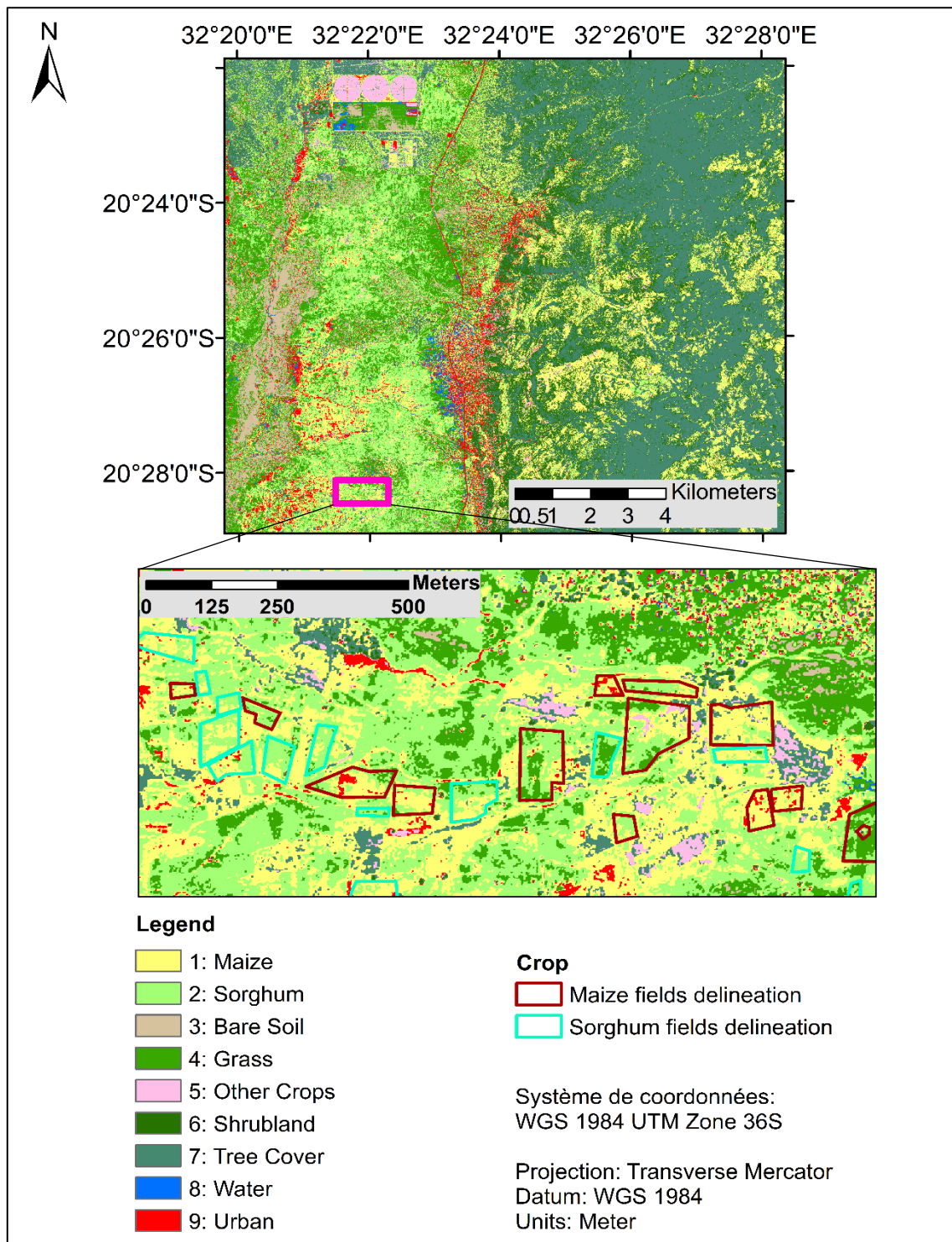


- Makoni



	<p>📅 2019-01-12 ⌚ 08:15:10 UTC ☁️ 99.54 % 📄 EPSG:4326 📖 36KUE</p> <p><a href="#">Visualize</a></p>		<p>📅 2019-01-17 ⌚ 08:15:14 UTC ☁️ 74.81 % 📄 EPSG:4326 📖 36KUE</p> <p><a href="#">Visualize</a></p>		<p>📅 2019-01-22 ⌚ 08:15:11 UTC ☁️ 100 % 📄 EPSG:4326 📖 36KUE</p> <p><a href="#">Visualize</a></p>
	<p>📅 2019-01-27 ⌚ 08:15:15 UTC ☁️ 26.1 % 📄 EPSG:4326 📖 36KUE</p> <p><a href="#">Visualize</a></p>		<p>📅 2019-02-01 ⌚ 08:15:11 UTC ☁️ 8.45 % 📄 EPSG:4326 📖 36KUE</p> <p><a href="#">Visualize</a></p>		<p>📅 2019-02-06 ⌚ 08:15:15 UTC ☁️ 97.31 % 📄 EPSG:4326 📖 36KUE</p> <p><a href="#">Visualize</a></p>
	<p>📅 2019-02-11 ⌚ 08:15:11 UTC ☁️ 23.77 % 📄 EPSG:4326 📖 36KUE</p> <p><a href="#">Visualize</a></p>		<p>📅 2019-02-16 ⌚ 08:15:14 UTC ☁️ 30.08 % 📄 EPSG:4326 📖 36KUE</p> <p><a href="#">Visualize</a></p>		<p>📅 2019-02-21 ⌚ 08:29:51 UTC ☁️ 1.09 % 📄 EPSG:4326 📖 36KUE</p> <p><a href="#">Visualize</a></p>
	<p>📅 2019-02-26 ⌚ 08:24:12 UTC ☁️ 98.44 % 📄 EPSG:4326 📖 36KUE</p> <p><a href="#">Visualize</a></p>		<p>📅 2019-03-03 ⌚ 08:26:15 UTC ☁️ 1.66 % 📄 EPSG:4326 📖 36KUE</p> <p><a href="#">Visualize</a></p>		<p>📅 2019-03-08 ⌚ 08:19:25 UTC ☁️ 7.27 % 📄 EPSG:4326 📖 36KUE</p> <p><a href="#">Visualize</a></p>
	<p>📅 2019-03-13 ⌚ 08:26:15 UTC ☁️ 33.67 % 📄 EPSG:4326 📖 36KUE</p> <p><a href="#">Visualize</a></p>		<p>📅 2019-03-18 ⌚ 08:23:12 UTC ☁️ 85.68 % 📄 EPSG:4326 📖 36KUE</p> <p><a href="#">Visualize</a></p>		<p>📅 2019-03-23 ⌚ 08:19:42 UTC ☁️ 50.33 % 📄 EPSG:4326 📖 36KUE</p> <p><a href="#">Visualize</a></p>
	<p>📅 2019-03-28 ⌚ 08:19:48 UTC ☁️ 3.19 % 📄 EPSG:4326 📖 36KUE</p> <p><a href="#">Visualize</a></p>		<p>📅 2019-04-02 ⌚ 08:21:13 UTC ☁️ 27.25 % 📄 EPSG:4326 📖 36KUE</p> <p><a href="#">Visualize</a></p>		<p>📅 2019-04-07 ⌚ 08:25:06 UTC ☁️ 58.27 % 📄 EPSG:4326 📖 36KUE</p> <p><a href="#">Visualize</a></p>
	<p>📅 2019-04-12 ⌚ 08:29:17 UTC ☁️ 97.15 % 📄 EPSG:4326 📖 36KUE</p> <p><a href="#">Visualize</a></p>				X

Appendix 3: Classification of Ward 16 obtained with a Pléiades image and a shapefile of 9 landcovers classes as input.



Appendix 4: Confusions matrices of the classification produced for Ward 16 with a Pléiades images

Predicted	Reference									Precision	F-score
	1	2	3	4	5	6	7	8	9		
1	8116	5505	12	1736	60	13759	9249	0	75	38512	0.21074
2	7679	10338	284	5894	1135	18847	327	0	28	44532	0.23215
3	51	303	8614	351	89	5161	4	0	235	14808	0.58171
4	3144	6878	1645	9757	719	15851	17	0	93	38104	0.25606
5	348	107	0	107	0	2681	735	1	69	4048	0
6	93	0	0	8	0	4815	23971	1	28	28916	0.16652
7	407	23	0	52	0	5349	278765	0	34	284630	0.9794
8	21	71	61	4	0	441	0	0	74	672	0
9	2424	1543	2221	206	0	2178	5	15	1494	10086	0.148126
<b>SUM</b>	22283	24768	12837	18115	2003	69082	313073	17	2130	464308	<b>Overall Accuracy</b>
<b>Recall</b>	0.3642	0.4174	0.671	0.5386	0	0.0697	0.8904	0	0.7014		69.33%

Predicted	Reference		SUM	Precision	F-score
	1+2	Other			
1+2	31638	51406	83044	0.380979	0.48638
Other	15413	365851	381264	0.959574	0.91632
<b>SUM</b>	47051	417257	<b>Overall Accuracy</b>		
<b>Recall</b>	0.6724	0.8768	464308		85.60%



## Detecting crop damage using Sentinel-2 imagery in a smallholder agriculture landscape

- Céline Champagne

Smallholder farmers in Sub-Saharan African countries are facing more and more challenges in terms of agriculture. Not only the lack of mechanization remains a problem to feed the population that continues to grow but in addition, external threats such as the invasive pest Fall armyworm and climate hazards increase the risk of food insecurity and famine in some countries.

Determining the extent of such damage requires extensive field work and a lot of time when it is necessary to act quickly to deliver food aid. Remote sensing can represent a real solution to this problem. Indeed, monitoring crops remotely is a technique that has been used successfully for several years now. The recent availability of free of access Sentinel-2 imagery opens the door to these kind of technologies for any developing countries.

Therefore, this master thesis aims, in collaboration with CIMMYT who is actively working on these matters in Zimbabwe, to assess the feasibility of detecting damage on maize in two districts of the country using satellite imagery. An intermediate objective is to produce a crop types map over the area of study.

Firstly, we looked at defoliation damage due Fall Armyworm. It turns out that those damage are rather patchy within a field. This in combination with a complex landscape, one must conclude that Sentinel-2 does not have the spatial characteristic to overcome the configuration of these smallholder fields that, on top of the already existing confounding factors, suffered from intense drought. Secondly, this work took a turn after Cyclone Idai hit our study area. Chipinge being badly impacted by extensive floods and heavy winds, it was decided to evaluate Sentinel-2 capacity in detecting the resulting damage. As results, it appears possible to detect flood damage. Indeed, some features, namely the GCI, NDWI2, the NIR band and the CIRE that uses a band in the red-edge appears to be able to differentiate the extreme classes of damage. Furthermore, by comparing Sentinel-2 images before and after the Cyclone with the SWIR band, the areas that got flooded could clearly be distinguished. However, there were some inadequacies between what we could visually see and the ground truth data which highlights the great challenges when it comes to using remote sensing in a complex environment. This work therefore highlights the difficulties that must be overcome in order to be able to detect crop damage remotely in a context of small-scale agriculture.

Using a pixel-based Random Forest classification, a cropland mask was obtained with an F-score for crop of 61% and an overall accuracy of 79%. Once the crop pixels were isolated, the classification of maize, sorghum and other crops was performed. Out of the performance rate of 61%, the three classes were classified with an F-score of 72%, 65% and 99% respectively. Finally, a crop types map was produced using VHR Pléiades imagery and the F-score for maize and sorghum was of 63% for Ward 18 and 48% for Ward 16. In both cases, about 50% of crop misclassification occurred with shrublands and grasslands. Both sensors show limitations and these issues might be highly related with the characteristics of the fields in Zimbabwe that are of small size and rainfed, plus the unusual climatic situation on this crop season.

This work could therefore underline the challenges faced by remote sensing in smallholder agriculture in part of Zimbabwe and highlight perspectives for further investigations.